

# Fatigue Assessment of Composite Propellers

Master of Science Thesis

George Patsantzopoulos





# Fatigue Assessment of Composite Propellers

Master of Science Thesis

by

George Patsantzopoulos

to obtain the degree of Master of Science  
at the Delft University of Technology  
to be defended publicly on September 25 of 2024, at 09:30

*Thesis committee:*

Chair:	Dr. Pahlavan Pooria
Supervisors:	Dr. Kassapoglou Christos PhD Candidate Huijjer Arno
External examiner:	Dr. Henk den Besten
Place:	Faculty of Mechanical Engineering, Delft
Project Duration:	November, 2023 - September, 2024
Student number:	5832527

An electronic version of this thesis is available at <http://repository.tudelft.nl/>.



*To my beloved grandmother  
Evaggelia Michopoulou  
(1929–2022)*

# Abstract

Recent advancements in composite materials have significantly influenced various industries, necessitating accurate fatigue assessment models. This research aims to evaluate the fatigue behavior of composite structures using Kassapoglou's analytical method, originally designed for metals. Adapted to composites, the method gave good lifespan predictions compared to experimental data. In cases of disagreement between predicted and experimental data (in some of the examined cases), the main cause was the lack of discrete stress strain data from literature. In continuation to this model, a new stiffness degradation model was also developed presenting results in a preliminary testing.

An updated Finite Element Analysis (FEA) model for a GFRP blade, part of the EcoProp project, was created by correcting fiber alignment and adding root regions in the previous models. The aim of this model is to find the hot spots (which are the stress critical locations) of the blade during operation and, combined with the lifespan model to make predictions about the fatigue life of the blade. The updated FEM model identified a new critical hot spot compared to previous works and provided a more realistic representation of the blade, with critical stress analysis confirming the most vulnerable regions. An experiment will be conducted in the next few months to validate whether these predictions are accurate or not.

The study also includes the development of a stiffness degradation model, estimating tangent and secant modulus degradation. This model aligned well with experimental data, but further investigation is necessary, especially when the lifespan fatigue model becomes a more robust method.

Predictions for the blade under actual load conditions emphasized the importance of considering out-of-plane stresses and highlighted the need for small-scale coupon experiments. This research demonstrates the potential of the proposed method for rapid and accurate fatigue predictions in composites, contributing to the development of robust fatigue assessment models and reducing the reliance on conservative safety factors in design.

# Contents

<b>List of Figures</b>	<b>v</b>
<b>List of Tables</b>	<b>viii</b>
<b>1 Introduction</b>	<b>1</b>
<b>2 Literature Review</b>	<b>2</b>
2.1 State of the art . . . . .	2
2.2 Knowledge Gaps . . . . .	12
2.3 Conclusion . . . . .	13
<b>3 Lifetime Prediction Model</b>	<b>14</b>
3.1 Methodology . . . . .	14
3.2 Model Validation and Verification . . . . .	19
3.3 Conclusions. . . . .	31
<b>4 Stiffness Degradation Model</b>	<b>33</b>
4.1 Methodology . . . . .	33
4.2 Validation of the method . . . . .	36
4.3 Conclusions. . . . .	44
<b>5 Finite Element Analysis</b>	<b>45</b>
5.1 Description of the model . . . . .	45
5.2 Results . . . . .	49
<b>6 Predictions for a GFRP blade</b>	<b>53</b>
6.1 Description of Methodology . . . . .	53
6.2 Material Properties . . . . .	55
6.3 Predictions . . . . .	61
6.4 Conclusions. . . . .	65
<b>7 Conclusions</b>	<b>67</b>
<b>8 Recommendations for future work</b>	<b>69</b>
<b>References</b>	<b>72</b>
<b>A Matlab functions</b>	<b>73</b>
<b>B Material properties of GFRP blade</b>	<b>76</b>
<b>C FEA: Marc Mentat</b>	<b>79</b>

# List of Figures

2.1	Geometry discretization of blade [1]	3
2.2	Determination of the material orientation [1]	3
2.3	Maximum Tsai-Wu failure indices of the composite propeller blade for the new FEM model [3]	3
2.4	Simplified flow diagram of Herwerden's thesis taken from [3].	4
2.5	First two loading-unloading cycles in stress-strain space for R=0. This figure is taken from [4]	7
2.6	Linear versus Nonlinear material behaviors. This figure is also taken from [4]	7
2.7	Coordinate System of Material. This figure is taken from [29]	8
2.8	Variation of hysteresis loop under cycling loading. The figure is taken from [36]	10
2.9	Stress strain curve for the cyclic loading of GFRP samples in the range of 25-250 MPa. The figure is taken from [39]	11
2.10	Doubly curved propeller blade made of GFRP	12
3.1	Fatigue cycles for $0 \leq R < 1$ , [4]	14
3.2	Energy density $U_{df}$	16
3.3	Variation of mechanical properties from region to region	18
3.4	Normal distribution	18
3.5	Figures obtained from paper,[42]	19
3.6	Initial slope of the experimental data	20
3.7	Complementary approach	20
3.8	Ramberg-Osgood approach	21
3.9	Comparison of experimental data with predictions for coupon 1	22
3.10	Comparison of experimental data with predictions for coupon 2	22
3.11	Comparison of experimental data with predictions for coupon 3	22
3.12	Comparison of experimental data with predictions for coupon 4	23
3.13	Figures obtained from paper,[43]	23
3.14	Initial slope of the experimental data	24
3.15	Complementary approach	24
3.16	Ramberg-Osgood approach	25
3.17	Comparison of experimental data with predictions using the geometric mean of the predicted lifespans from all specimens.	25
3.18	Figures obtained from paper,[44]	26
3.19	Initial slope of the experimental data	26
3.20	Complementary approach	27
3.21	Ramberg-Osgood approach	27
3.22	Comparison of experimental data with predictions	28
3.23	Figures obtained from paper,[45]	28
3.24	Initial slope of the experimental data	29
3.25	Complementary approach	29
3.26	Ramberg-Osgood approach	30
3.27	Comparison of experimental data with predictions	30
3.28	Predictions using every static stress strain curve of each coupon	31
4.1	Stiffness degradation - general representation	33
4.2	Pair of stresses and strains that correspond to dissipated energy	34
4.3	Definition of stiffness degradation terms	35
4.4	Figure taken from [46]. The examined curve is the pink one B2-BD.	36
4.5	Stress strain curve: Model vs experiment from the origin to the applied stress.	36
4.6	Residual stress that corresponds to dissipated energy	37
4.7	Residual strain that corresponds to dissipated energy	38
4.8	Stress ( $\sigma_{mb}$ ) strain ( $\varepsilon_{mb}$ ) curve	38
4.9	Residual scaled strain that corresponds to dissipated energy	39



4.10 Experiments made by Zhang. This figure was taken from his thesis [2]. . . . .	39
4.11 Stress strain curve of the first tested coupon in Zhang's thesis. . . . .	40
4.12 Fictitious stress strain curve for coupon 1. . . . .	40
4.13 Ramberg - Osgood model vs fictitious stress strain curve. . . . .	41
4.14 Residual stress that corresponds to dissipated energy . . . . .	41
4.15 Residual strain that corresponds to dissipated energy . . . . .	42
4.16 Stress ( $\sigma_{mb}$ ) strain ( $\varepsilon_{mb}$ ) curve . . . . .	42
4.17 Residual scaled strain that corresponds to dissipated energy . . . . .	43
5.1 Suction side of the blade . . . . .	45
5.2 Pressure side of the blade . . . . .	46
5.3 Position of critical elements, both images were taken from the work of Zhang [2] . . . . .	47
5.4 Clamped boundary condition and actual distributed pressure . . . . .	47
5.5 Solid brick element and Composite brick element - Marc Mentat [49] . . . . .	47
5.6 Design of new brace. The image is used after the permission of the designer. . . . .	48
5.7 FEA model: Experiment . . . . .	48
5.8 Coordinate system before applying the subroutine . . . . .	49
5.9 Orient2 subroutine, image taken from [50] . . . . .	50
5.10 Coordinate system after applying the subroutine . . . . .	50
5.11 Relation of the user defined coordinate system (XYZ) and lamina's local system (123) . . . . .	50
5.12 Inputs in FEA - Marc . . . . .	51
5.13 Numerical results of the actual loading - critical layer 11 . . . . .	51
5.14 Numerical results of the experiment - critical layer 11 . . . . .	52
5.15 Results of Zhang, [2] . . . . .	52
6.1 Critical elements from the FEM analysis . . . . .	53
6.2 Estimated variation of failure index - Actual load case . . . . .	54
6.3 Estimated variation of failure index - Experiment . . . . .	54
6.4 Longitudinal tension of GFRP, [51] . . . . .	55
6.5 Model vs experimental curve, longitudinal tension . . . . .	55
6.6 Transverse tension of GFRP, [52] . . . . .	56
6.7 Model vs experimental curve, transverse tension . . . . .	56
6.8 Longitudinal compression of GFRP, [53] . . . . .	57
6.9 Model vs experimental curve, longitudinal compression . . . . .	57
6.10 Transverse compression of GFRP, [54] . . . . .	58
6.11 Model vs experimental curve, transverse compression . . . . .	58
6.12 Shear properties of GFRP, [55] . . . . .	59
6.13 Model vs experimental curve, shear . . . . .	59
6.14 Strength as a function of cycles - longitudinal tension . . . . .	62
6.15 Strength as a function of cycles - longitudinal compression . . . . .	62
6.16 Strength as a function of cycles - transverse tension . . . . .	62
6.17 Strength as a function of cycles - transverse compression . . . . .	63
6.18 Strength as a function of cycles - In plane shear . . . . .	63
6.19 Maximum stress criterion - 1 <sup>st</sup> failure index - transverse direction . . . . .	65
6.20 Maximum stress criterion - 2 <sup>nd</sup> failure index - longitudinal direction . . . . .	65
6.21 Actual blade: fabrication of the hub-blade interface . . . . .	66
A.1 GUI of grabit function . . . . .	73
A.2 Calibration of the curve . . . . .	74
A.3 Grabbing points . . . . .	74
A.4 Resultant curve - coupon $[0_3/90]_s$ . . . . .	75
A.5 Script with <i>fmincon</i> . . . . .	75
B.1 Original stacking sequence of the GFRP blade . . . . .	76
B.2 Allocation of the different zones . . . . .	77
C.1 Marc Mentat - GUI . . . . .	79
C.2 Create a solid . . . . .	79
C.3 Meshing . . . . .	80

---

C.4	Selecting hexahedral elements . . . . .	80
C.5	Available failure criteria . . . . .	81
C.6	Creating a composite material . . . . .	81
C.7	Stacking sequence . . . . .	82
C.8	Different materials . . . . .	82
C.9	Different types of elements . . . . .	83
C.10	Clamped boundary condition . . . . .	83
C.11	Tensile force at the other side . . . . .	84
C.12	Use table . . . . .	84
C.13	Apply the load linearly . . . . .	84
C.14	Select table when the load is applied . . . . .	85
C.15	Time steps . . . . .	85
C.16	Initial loading . . . . .	86
C.17	Job results . . . . .	86
C.18	Extract results . . . . .	87
C.19	Tools . . . . .	87

# List of Tables

3.1	Data imported from paper [42]	19
3.2	Terms of the complementary approach and Ramberg - Osgood (RO) - first case	21
3.3	90 <sup>th</sup> and 10 <sup>th</sup> percentiles of Young's modulus - Roundi et al. [42]	21
3.4	Terms of the complementary approach and Ramberg - Osgood (RO) - second case	24
3.5	Data imported from paper [44]	26
3.6	Terms of the complementary approach and Ramberg - Osgood (RO) - third case	27
3.7	Data imported from paper [45]	28
3.8	Terms of the complementary approach and Ramberg - Osgood (RO) - fourth case	29
4.1	R-O terms determined by the model	37
4.2	Stiffness degradation: predicted values vs measured values	39
4.3	R-O terms determined by the model - Zhang	41
4.4	Predicted values of stiffness degradation model vs experimental values	43
4.5	Comparison of mean values	43
6.1	Results of FEA in terms of stresses	54
6.2	Longitudinal tensile properties of GFRP, [51]	56
6.3	Tensile properties in transverse direction of GFRP, [52]	57
6.4	Longitudinal compression properties of GFRP, [53]	58
6.5	Compression properties in transverse direction of GFRP, [54]	59
6.6	Shear properties of GFRP, [55]	60
6.7	Ramberg-Osgood terms determined for the lifespan predictions	61

# Introduction

In recent years, advanced materials like composites have increasingly replaced metal components in various sectors, especially where lighter solutions are preferred. Prominent examples include the aerospace, aeronautical, automotive, and maritime industries. Despite their significant mechanical advantages, there is no universal method for assessing their fatigue, often leading to overestimated safety factors. This issue arises from the complexity of these materials, which spans from the micro to the macro level. Numerous defects can form either during manufacturing or in the early stages of loading. One of the most critical areas in a composite material is the interface between fibers and matrix, particularly for fibers oriented closer to 90 degrees. These laminas are matrix-dominated, and the matrix, usually a polymer, lacks the advanced properties of the fibers. The complexity increases further under dynamic conditions such as fatigue.

Three categories of fatigue models are prevalent in the literature. These include fatigue life models that use stress life cycle curves, such as Goodman diagrams; phenomenological models that address the degradation of the mechanical response of composites either deterministically or statistically; and progressive damage models that estimate how defects evolve during cyclic loading and how mechanical properties degrade over time. All of these models rely heavily on fatigue experimental data from small-scale coupons, and no single methodology applies universally to all composites. This leads to large safety factors during the design process, so more expensive structures are fabricated with an increased adverse environmental impact as polymer resins are used underscoring the need for a more general model.

A significant challenge in recent years has been transitioning propeller blades for ships from metal to composite materials. Various studies have been conducted under the EcoProp project, focusing on the fatigue assessment of marine blades. The main advantage of composites is their higher efficiency, especially under off-design conditions, due to their ability to provide a flexible structure depending on the orientation of the fibers. GFRP and CFRP blades were investigated by Maljaars [1] and Zhang [2] in the case study of the Nautilus diving support vessel, which is designed to sail in calm waters with a four-blade composite propeller rotating at a constant speed. Maljaars conducted a fluid-structure interaction analysis for the GFRP blade, while Zhang used the same loading conditions for a carbon fiber material. Zhang's short-term fatigue investigation provided results on stiffness degradation and fatigue life of the tested coupons. Van Herwerden [3] developed a progressive damage model based on Zhang's data and combined models from the literature, offering a fatigue lifespan for the blade. However, this thesis presents a more detailed analysis using a different approach.

The objective of this thesis is to predict the performance of a GFRP blade in the same case study of the Nautilus support vessel by applying an innovative method proposed by Kassapoglou [4]. This method focuses on determining energy dissipation during cyclic loading and predicting fatigue life. It was previously applied to metal alloys, showing good agreement with experimental data. The main goal is to investigate whether this method can also be applied to composite materials and if it can predict stiffness degradation. The advantage of this method is its analytical form, which leads to fast fatigue life predictions. Additionally, this thesis explores whether combining this method with an FEM model can provide accurate predictions for an actual structure like the blade. This process involves conducting a ply-by-ply analysis and using the model on the most critical layer identified from FEA.

# Literature Review

## 2.1. State of the art

### 2.1.1. Flexible Marine Propellers

The history of propulsion systems involves renowned scientists and engineers such as Archimedes, Leonardo Da Vinci, Robert Hooke, and Bernoulli, among others. Inventors and engineers have proposed numerous designs and patents over the years, all with the goal of achieving the most efficient propeller. The design of the propeller, as known today, originated from an incident on the Paddington Canal in 1837 involving the prototype boat F P Smith [5]. The introduction of theoretical models in the 19th century by figures like Rankine and Froude played a crucial role in understanding the physics of propellers and contributed significantly to their development. In the past, marine propellers were primarily designed as rigid, fixed-geometry structures. However, advances in computational modeling, material research, and the evolution of manufacturing processes have played a crucial role in optimizing propeller efficiency by incorporating more complex geometries and utilizing adaptive materials [6].

Focusing more on materials, composites are gaining popularity for their advantages over metals. They offer lighter solutions, enhanced durability, and greater freedom in the design process. In contrast to conventional rigid propellers made of nickel-aluminum-bronze (NAB) or manganese bronze (MB), one of the advantages of composite propellers made of polymer resin and fibers is flexibility. Flexible composite propellers can contribute to improved efficiency at off-design conditions [2]. Despite that, careful material selection is crucial for composites used in the marine sector. The choice of reinforcement becomes particularly significant when considering factors such as corrosion, similar to how resin can be affected when the composite is immersed in saltwater [7]. Additionally, the potential complexity that a composite structure may have also affects its response under fatigue loading. This is one of the reasons that increased effort is given for more accurate predictions of composites behavior.

Maljaars [1] investigated the hydrodynamic and structural response of a flexible propeller blade made of composite material (GFRP) in the case study of the Nautilus diving support vessel. The operational conditions that were considered are that the vessel sails in a straight path in the calm water at the constant speed of 10.4 knots, with a four-blade composite propeller rotating at a constant speed of 600 rpm. The propeller experiences a non-uniform wakefield. At this study, a Fluid Structure Interaction (FSI) was necessary which can be either done by merging the fluid and structural set of equations into one and solve them simultaneously (monolithic solution) or by splitting the fluid and structural sub-problem and solve them sequentially. In the second way, the coupling iterations are repeated until they converge to the monolithic solution.

In Maljaars' research, a combination of the Boundary Element Method (BEM) and Finite Element Method (FEM) was employed. The BEM determined the hydrodynamic loads on the blade, while the FEM assessed its structural response. Experimental studies were additionally conducted at the Maritime Research Institute Netherlands (MARIN) to validate the results obtained from the BEM-FEM methods in non-uniform flows. A notable aspect of the analysis was the consideration of material orientation in the FEM program MARC, where a sub-routine was imported to ensure the correct alignment of fibers on the doubly curved blade - Figures (2.1, 2.2).

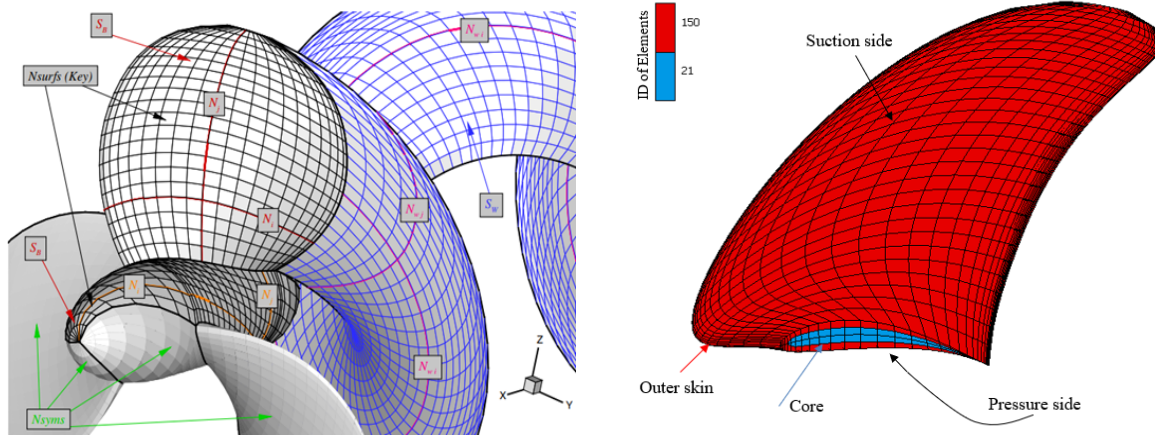


Figure 2.1: Geometry discretization of blade [1]

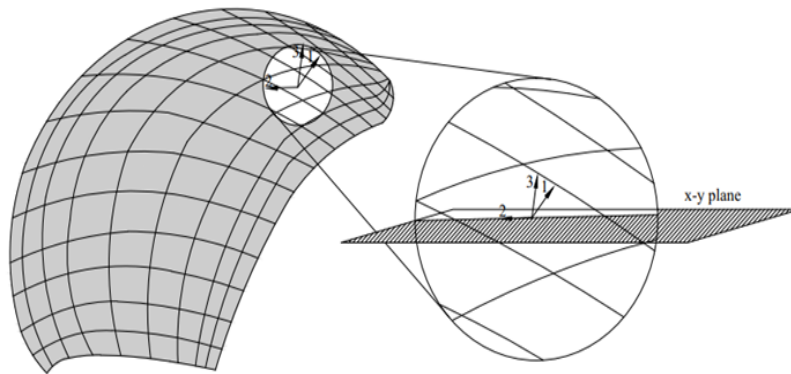


Figure 2.2: Determination of the material orientation [1]

Zhang conducted an investigation into the short-term structural performance of a blade similar in geometry to Maljaars' work but made of CFRP [2]. In this research, a series of specimens, both wetted and dry, underwent testing to assess their stiffness and strength under static loading and after 10 thousand and 1 million number of cycles. The objective was to observe the degradation of material properties due to moisture exposure and fatigue loading. Additionally, sensors (PZT) were embedded into the blade, and their impact on the structure was examined.

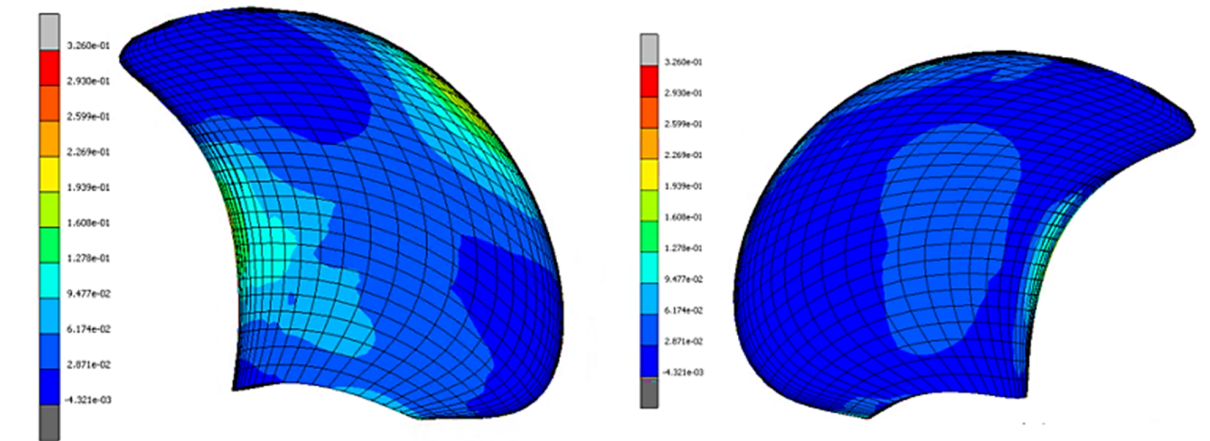
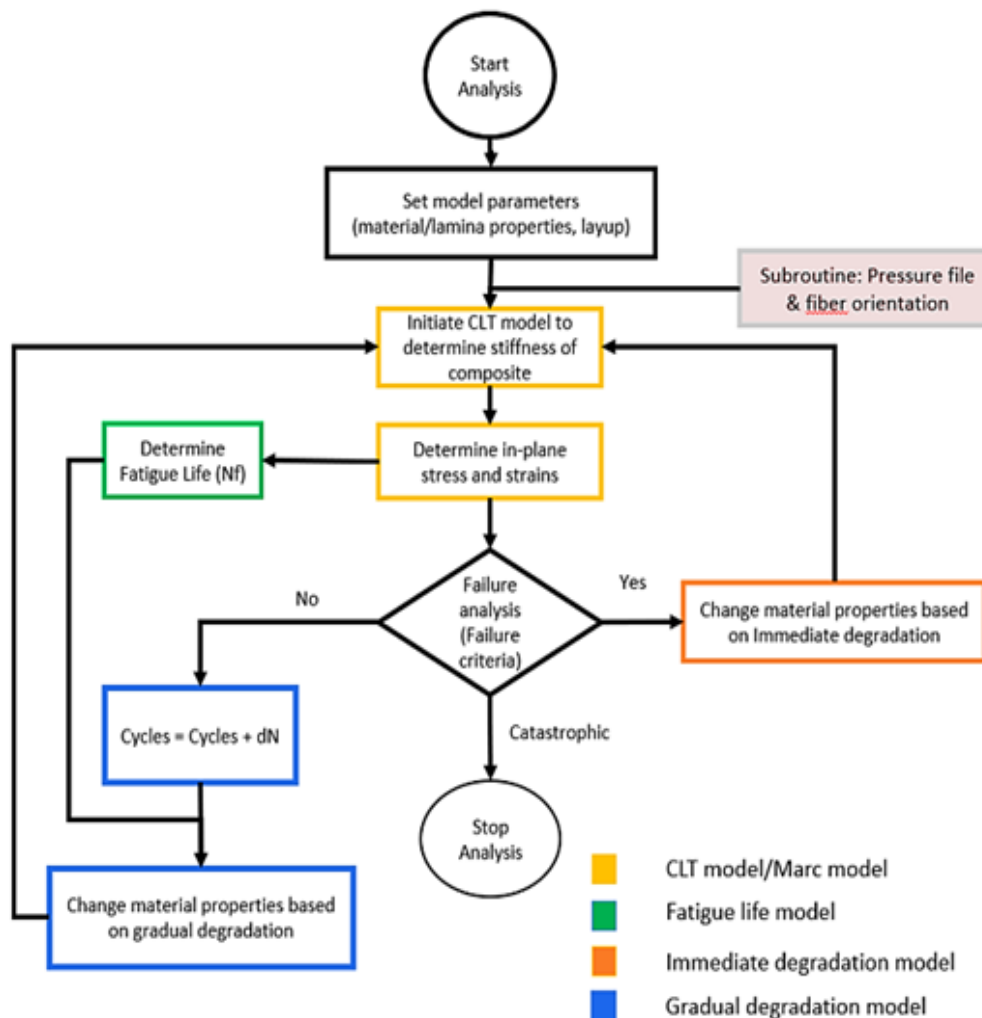


Figure 2.3: Maximum Tsai-Wu failure indices of the composite propeller blade for the new FEM model [3]

In continuation of these works, Van Herwerden [3] applied a macroscopic Progressive Damage Model (PDM) to evaluate the fatigue lifetime of Zhang's CFRP blade and predict the degradation of material properties. During this research, Van Herwerden utilized models from the literature to predict the fatigue lifetime, drawing from works such as Shokrieh et al. [8] and Kawai [9]. Additionally, he employed two other models derived from those mentioned before. In the first model, the strain energy densities from longitudinal, transverse, and shear contributions were added to the total normalized strain energy density. In the second model, the aforementioned three strain energy densities were used separately for the determination of fatigue life. The third model was Kawai's one where Tsai-Hill criterion was used, whereas in the fourth model, instead of using the Tsai-Hill criterion in the Kawai's approach, the Hashin criterion was applied. For the gradual degradation of material properties, the model of Shokrieh and Lessard [10] was employed.

In the progressive model, Finite Element Method (FEM) analysis was used to estimate global stresses on the blade, subsequently transformed into local stresses. Following this, a failure analysis was conducted, considering either an immediate degradation of material properties or a gradual degradation per cycle. The procedure is illustrated in Figure 2.4.



**Figure 2.4:** Simplified flow diagram of Herwerden's thesis taken from [3].

Beyond the Nautilus and Greenprop propeller designs, several investigations have explored flexible marine propellers in the past. Chuang analyzed the strength of a composite marine propeller examining its Fluid-Structure Interaction (FSI), using Finite Element Method (FEM), and Lifting Surface Theory (LST). The study examined symmetric balanced and unbalanced laminates made of graphite-epoxy T300/1076E [11]. It is noteworthy to mention here that unbalanced laminates have bending-twisting coupling terms, leading to a change in the angle of attack as the blade bends. As it is mentioned in this research, the critical regions in terms of delamination are the trailing and leading edge of the blade. Young emphasized the necessity of FSI analysis for flexible composite marine propellers [12]. This analysis helps predict blade deflection, hydrodynamic loads, the impact of cavitation, and stress distribution. Blasques et al. conducted research on optimizing the lay-up of a composite marine propeller, considering factors such as fuel consumption, thrust, and torque [13]. Notably, the investigated propeller was larger than any previously studied. The study suggested that flexible marine propellers surpass conventional rigid ones in terms of fuel consumption and efficiency, a viewpoint also echoed in the work of Motley et al. [14]. Similar conclusions were drawn in the investigation by Vijayanandh et al. [15], where GFRP marine propellers were proposed as more suitable than aluminum alloy or steel alternatives from a fatigue assessment of a marine blade.



### 2.1.2. Fatigue Life Models

Fatigue is a phenomenon that exists everywhere in nature, from materials to human life (aging) and describes the degradation of properties. The comprehension of fatigue has evolved over many years of investigation. However, the fatigue behavior of composite materials differs from that observed in metals. Various factors contribute to this distinction, ranging from disparate material configurations to distinct manufacturing methods. Researchers have undertaken numerous efforts to model fatigue in composites, with many of them relying on experimental work. They have sought to establish standards wherein different parameters are controlled to assess fatigue behavior. Generally, fatigue models can be categorized into three categories [16], as outlined in the following paragraph.

These three categories comprise Fatigue Life Models (FLM), Phenomenological Models (PM), and Progressive Damage Models (PDM). Models falling into the first category involve stress-life cycles (S-N curves) and Goodman diagrams, similar to those presented in the work of Kawai [17]. Phenomenological models describe the deterioration of a material property due to fatigue, as exemplified in the work of Van Paepegem [18]. These models may exhibit either a deterministic or a statistical character. Additionally, Progressive Damage Models (PDM) are used to estimate how damage evolves and how it is affected by the degradation of material properties due to fatigue, operating in iterative processes. The functionality of a PDM is grounded in theoretical models in its background, as presented in the article by Degrieck et al. [16]. The formulations that were presented in the method proposed by Kassapoglou [4] (for metals), follow the typical form of S-N curves without the necessity of fitting experimental data. A component that could be characterized closer to a PD model is the determination of stiffness degradation, which relies on the new K and n values of Ramberg-Osgood relationship in every loop ( R-O:  $\varepsilon = \frac{\sigma}{E_o} + K(\frac{\sigma}{E_o})^n$ ).

Some of the preceding studies regarding composite fatigue are elucidated in this paragraph. Hwang and Han [19] introduced the concept of the "fatigue modulus". This built upon the assumption made by Wang and Chim [20] that fatigue damage follows a power function of fatigue cycles and is proportionate to a parameter dependent on the damage. Failure occurs when the resultant strain equals the ultimate static strain. In this study, researchers recommend using physical parameters for cumulative damage rather than the number of cycles. Mao and Mahadevan [21] proposed a damage accumulation model for predicting the fatigue lifetime of composite materials; however, it necessitates a series of Young's modulus measurements every few cycles. Kassapoglou [22] developed a model to compute the residual strength of composite structures after cyclic loading and utilized it to estimate Goodman constant life diagrams (CLDs). This approach requires a dataset containing the statistical distribution of static strength for the composite material. Shokrieh et al. formulated a progressive damage model to forecast the fatigue life of cross-ply laminates [23], while Sarfaraz et al. put forth a semi-empirical formulation by amalgamating two existing models to capture the fatigue behavior across various composite materials [24]. However, as noted by the latter researcher, a universally applicable fatigue life prediction methodology has not been achieved yet[25].

An interesting approach for estimating fatigue lifetime was recently introduced by Kassapoglou in his publication titled "**Determination of energy dissipation during cyclic loading and its use to predict fatigue life of metal alloys**" [4]. This research entails deriving a closed-form expression for the initiation of fatigue cycle to failure and outlining a methodology for determining the specific energy dissipated per cyclic loading, specifically for stress ratios  $0 \leq R < 1$ . A validation study was conducted, comparing the results with four different alloys.

The core concept of this research is founded on the idea that fatigue failure occurs when the total energy per unit volume dissipated during cyclic loading equals the area under the stress-strain curve. As outlined in the paper, Inglis [26] was among the pioneers who proposed this approach, serving as inspiration for numerous researchers exploring different cases with varied properties or characteristics to predict fatigue life or its effects. Many of these methods relied on experimental data and were primarily applicable to low-cycle fatigue, whereas the proposed method demonstrates results that align well with reality for low, medium, and high-cycle fatigue. An additional advantage lies in the ability to predict material lifespan with only a static tensile test. The material is assumed to follow a Ramberg-Osgood equation (2.1), and four key assumptions have been outlined according to [4]:

$$\varepsilon = \frac{\sigma}{E_o} + K\left(\frac{\sigma}{E_o}\right)^n \quad (2.1)$$

1. Every loading cycle ( $i$ ) follows Ramberg-Osgood equation (2.1), but it has its own stiffness  $E_i$  [GPa], coefficient  $K_i$  and exponent  $n_i$ . The last two material constants have no units.
2. The slope of the stress strain curve (AHB) during loading in figure 2.5 is assumed to be equal to the original stress-strain curve at point B with coordinates  $(\varepsilon, \sigma)$ .
3. The straight line (AB), which connects the residual strain  $(\varepsilon_{m_i}, 0)$  with  $(\varepsilon, \sigma)$ , splits the loading and unloading curves (AHB) and (BIA) into two regions with equal area.  $\varepsilon_{m_i}$  refers to the residual strain at cycle ( $i$ ).
4. The last assumption requires envisioning a system with both a purely linear and an inelastic response of a material, as illustrated in Figure 2.6. The relative area between these two lines is termed as "unavailable" energy. When a cyclic load is applied to the nonlinear material, a new curve with Ramberg-Osgood slope is generated, resulting in residual strain  $\varepsilon_{m_i}$ . The ratio between the area (CGBHA) to the "unavailable" energy (CEBGC) closely approximates the ratio of the total energy of the nonlinear behavior to the total energy of the linear behavior. By rearranging the terms, the following equation is derived:

$$\frac{CEBGC}{CEF} \approx \frac{CGBHA}{CGBFC} \quad (2.2)$$

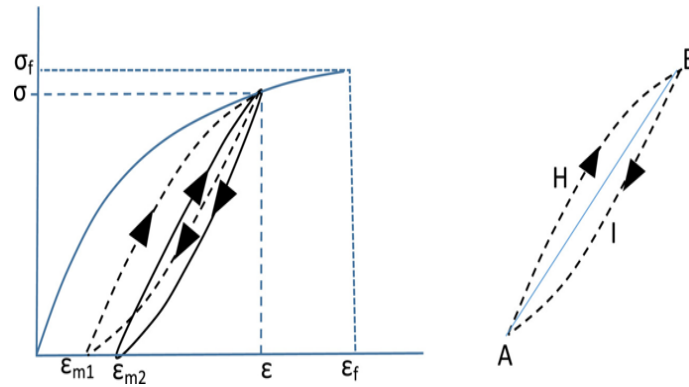


**Figure 2.5:** First two loading-unloading cycles in stress-strain space for  $R=0$ . This figure is taken from [4]

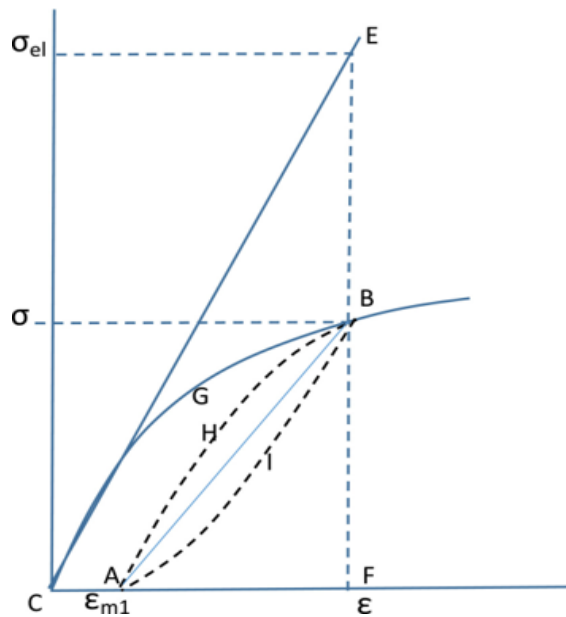


**Figure 2.6:** Linear versus Nonlinear material behaviors. This figure is also taken from [4]

### 2.1.3. Nonlinear Behaviour of Composite Materials

A nonlinear elastic-plastic behaviour on composite laminates is usually found in shear response, and the Ramberg-Osgood (RO) relation is commonly used to model it. Textile composite laminates present a nonlinear response to the different material orientations as shown in the work of Cousigne et al. [27]. Jelf et al. [28] presented the RO parameters for different materials in their investigation of the failure of carbon fibre/epoxy tubes under combined axial compression and torsion, with Makeev et al. [29] publishing the corresponding parameters for S2 glass/E773 epoxy tape and IM7-carbon/8552 epoxy tape for the shear planes 1-2 and 1-3 as they are shown in figure 2.7. Choi et al. [30] used RO formulation and presented the experimental values of short carbon-fiber reinforced polymer composites. Benedetto et al. [31] published the in-plane shear response of CF/Epoxy and CF Polyurethane by using RO formulation in their work, where the values of exponent  $n$  are close to one. An alternative way of using the Ramberg-Osgood relation was presented by Qiu and Fan [32] during the modeling of bamboo fiber-reinforced composite materials. In their investigation, a decreasing number of parameters is required to be obtained from the experiments. More specifically, in the generalized RO equation, stiffness  $E_o$ , coefficient  $K$  and exponent  $n$  are required, while in their expression, stress  $\varepsilon_o$  and strain  $\sigma_o$  are applied and only  $\alpha$  and  $n$  must be defined. This can be seen in the following expressions:

$$\varepsilon = \frac{\sigma}{E_o} + K \left( \frac{\sigma}{E_o} \right)^n \quad (2.3)$$

and it can be written as:

$$\frac{\varepsilon}{\varepsilon_o} = \frac{\sigma}{\sigma_o} + \alpha \left( \frac{\sigma}{\sigma_o} \right)^n \quad (2.4)$$

where  $(\varepsilon_o, \sigma_o)$  could be any reference stress and strain into the elastic stage with  $\alpha$  given by:

$$\alpha = K \varepsilon_o^{n-1} \quad (2.5)$$

As it is mentioned in their research, smaller  $\alpha$  and  $n$  denote a strain hardening deformation, while large  $n$  indicates an elastic-ideally-plastic model. For  $n$  almost equal to 1, a quasi-linear curve is obtained, and it is noteworthy that Ramberg-Osgood cannot be used to model a strain-softening curve.

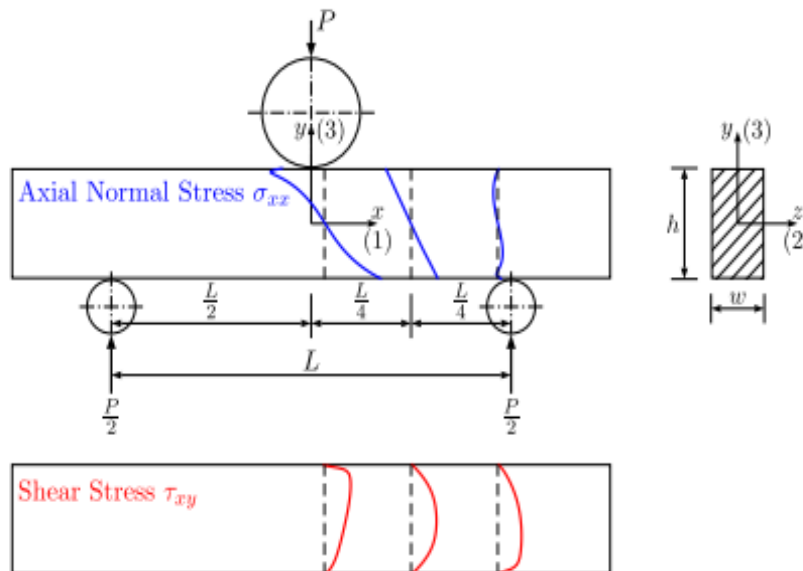


**Figure 2.7:** Coordinate System of Material. This figure is taken from [29]

A novel constitutive model for the generalization of the Ramberg-Osgood relation to capture nonlinear anisotropic fibre-reinforced materials with different tensile and compressive responses under a general stress state was published by Obid et al. [33].

The determination of the non-linear terms used in this study was made by minimizing a cost function  $f$  which is defined as:

$$f = \sum_{i=1}^{\Omega} \sum_{j=1}^{m_{\max}} \left( \frac{\varepsilon_{i,j,\text{model}} - \varepsilon_{i,j,\text{exp}}}{\varepsilon_{i,j,\text{exp}}} \right)^2 \quad (2.6)$$

with the first sum taking over all tests included in a set  $\Omega$ , whereas the second sum takes over  $m$  strain data points within each test. This equation (2.6) was used in this thesis to capture data from the literature, as it can be seen in the article [33].

The aforementioned approaches are related to composite materials that exhibit a nonlinear relationship. However, there are cases where the laminate shows a linear or very close-to-linear response. In such instances, the proposed method by Kassapoglou [4] can also be applied with a reformulation of fatigue life formula as described in his paper.

### 2.1.4. Dissipated Energy During Cyclic Loading

The concept that dissipated energy is related to the fatigue failure of a material has been investigated by many authors, with Inglis being among the pathfinders in 1927 [26]. It has been observed that metals indicate a convergence to the quantity of dissipated energy after some cycles of loading; however, the dissipation of energy is more complex in composite materials. The creation of different types of damages can lead to variations in the dissipated energy.

Holmes et al. investigated the evolution of hysteresis loops in UD SIC/CAS – II composite at room temperature [34]. They found that the hysteresis modulus decreases at an initial stage due to matrix multi-cracking, fiber/matrix debonding, and interface wear, with dissipated energy consistently decreasing until approaching fatigue fracture, where it increases rapidly.

Longbiao [35] utilized a hysteresis dissipated energy-based parameter to monitor damage evolution in carbon fiber–reinforced ceramic matrix. It was found that the response of dissipated energy is influenced by various factors, including peak stress, fatigue stress ratio ( $R$ ), matrix crack spacing, and fiber volume fraction. Specifically, hysteresis dissipated energy, denoted as  $U_n$ , increases towards final fatigue fracture at peak stress levels but behaves differently at intermediate and low peak stress levels. In the former,  $U_n$  increases to a peak value and then decreases until fracture; in the latter situation,  $U_n$  increases to a peak value, then decreases to a valley value, and subsequently increases again until fracture. Regarding stress ratio,  $U_n$  decreases with the increase of  $R$  during cycling loading. In the case of matrix crack spacing,  $U_n$  decreases when the interface partially debonds and increases when the interface debonds at the same cycle number. Finally, dissipated energy lessens with the rise of fiber volume fraction. More information related to the hysteresis dissipated energy can be found on [35].

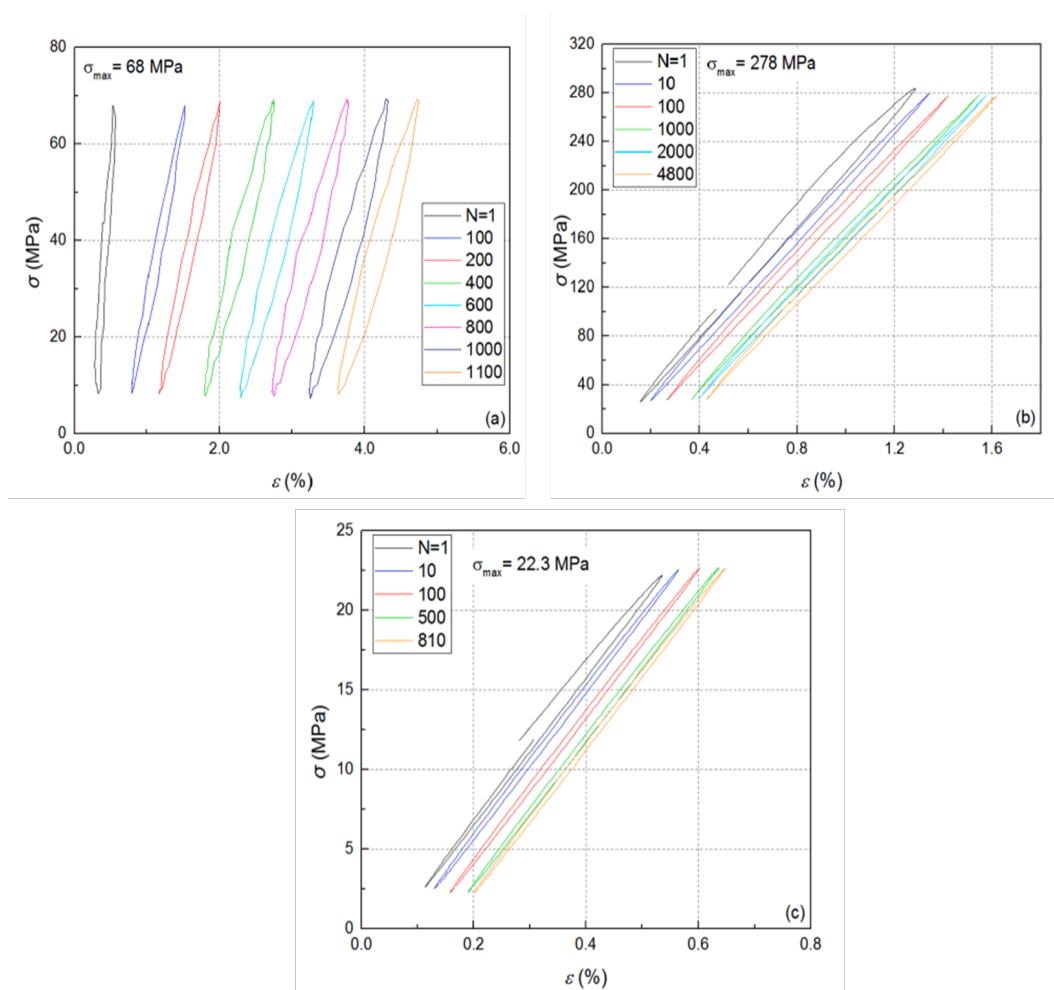


**Figure 2.8:** Variation of hysteresis loop under cycling loading. The figure is taken from [36]

Movahedi–Rad et al. [36] presented a novel fatigue life prediction methodology considering the creep effect on fatigue behavior in different GFRP laminates. In Figure 2.8, it can be seen that the dissipated energy shows a convergence as the number of cycles becomes larger.

Cadauid et al. [37] studied the fatigue performances of GFRP laminates under constant sinusoidal loading ( $f = 5$  Hz) at room temperature in different stress ratios. In this work, it was demonstrated that in the majority of cases, the energy dissipated per cycle near the end of the fatigue lifetime increased due to the expanded area captured by hysteresis loops. However, for different cases of R and fiber orientation, the energy dissipation remained nearly constant away from the end of coupons' lifetime.

Stikkelorum, in his master thesis [38], showed that the energy dissipation in relation to the number of cycles appeared to be a linear relationship between the lifetime of the specimen and the amount of energy dissipated during a coupon's life. Low, medium and high load levels were applied in his experimental work (from 16 to 65 kN) with stress ratio R being 0.1.

Sapozhnikov et al. [39] investigated the fatigue life of GFRP laminates under high-frequency cyclic loading. The analysis of the stress-strain curves demonstrated that hysteresis loops are slightly moving to the right and getting narrower – Figure 2.9.

Drvoderic et al. [40] investigated GFRP laminates of different orientations to compare crack density and dissipated energy as measures for off-axis damage. It was found that dissipated energy starts to increase at higher cycle numbers and does not stop rising after crack saturation.

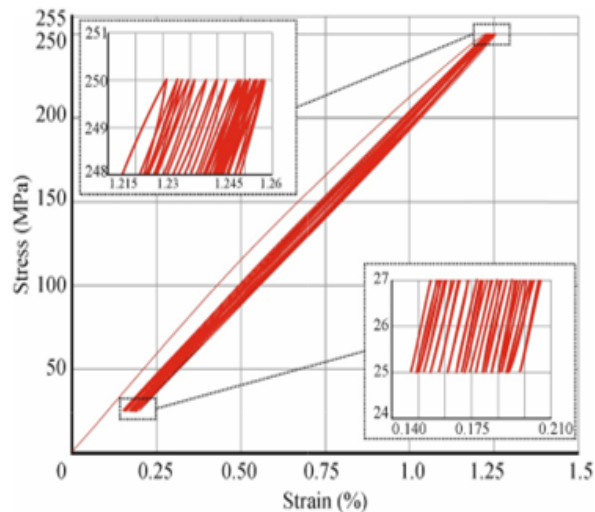


**Figure 2.9:** Stress strain curve for the cyclic loading of GFRP samples in the range of 25-250 MPa. The figure is taken from [39]

## 2.2. Knowledge Gaps

### 2.2.1. What does this research try to cover?

As outlined in the preceding paragraphs, research into flexible marine propeller blades has intrigued researchers in the maritime sector over the years. Although it has been established that Fluid-Structure Interaction (FSI) analysis is imperative for investigating marine propellers, there are not many studies focusing on propellers with complex geometries made of fiber-reinforced polymer materials. As it was described before, Maljaars and Zhang investigated the use of composite materials in marine propellers and Van Herwerden applied a progressive damage model to assess the fatigue lifespan of the blade based on the works of Shokrieh et al. [8] and Kawai [9].

It is important to note that both models were initially designed for unidirectional composites. In a detailed examination of Kawai's and Shokrieh's models, the former relied on empirical fatigue strength derived from existing literature, which was subsequently generalized in a later phase for the prediction of lifespan. On the contrary, Shokrieh's approach required a fatigue test to determine the material constants essential for his model. Consequently, if Kassapoglou's innovative method [4] is deemed valid for composites, it could offer significant benefits by providing quick results only through specimen tests. It is essential to underline the primary advantages of an analytical solution in this context, as highlighted in the work of Villanueva [41]. These advantages include speed, efficiency, insights into underlying mechanisms, extrapolation, generalization, and parameter-sensitive analysis.



**Figure 2.10:** Doubly curved propeller blade made of GFRP

## 2.3. Conclusion

### 2.3.1. Research Questions

In concluding this literature review, a central question emerges.

**To what extent can the fatigue lifetime of a composite material and subsequently propeller's blade be predicted using a constant dissipated energy per cycle?**

To address the main question, it is necessary to formulate several sub-questions that can break it down and explore it more thoroughly. As mentioned in the preceding paragraphs, the fatigue assessment of fiber-reinforced composite materials can be categorized into three approaches. To be more precise, the estimation of the fatigue life of a structure typically involves the application of Finite Element Method (FEM) analysis to investigate hot spots. Subsequently, one of these three approaches is chosen. Specifically, either fatigue life models, such as stress-cycle curves (S-N) or Fatigue Life Diagrams (FLDs), is employed, or phenomenological models using empirical formulas are applied by drawing upon data from the literature, or progressive damage models are selected. The potential to predict fatigue lifetime solely using data from static tensile tests in case  $0 \leq R \leq 1$  could revolutionize the engineering design of structures.

Some of the sub-questions that will assist in answering the main question are:

#### Research Question 1

Can this method be generalized and become applicable to composite materials other than metals?

#### Research Question 2

What are the necessary assumptions for that transition?

#### Research Question 3

Is this method able to capture stiffness degradation?

#### Research Question 4

Considering the fact that the dissipation of energy does not converge in some cases of composite materials (2.1.4), to what extent do these findings challenge the proposed method?

#### Research Question 5

Under what circumstances (regarding the dissipation of energy) can this method be deemed applicable?

#### Research Question 6

How do the method's results compare to experimental data?



# Lifetime Prediction Model

## 3.1. Methodology

### 3.1.1. Brief description of the method

The mechanisms behind an examined phenomenon can be more easily understood when closed-form analytical expressions have been derived. As previously discussed, analytical models typically surpass other approaches in terms of efficiency, interpretability, speed, extrapolation/generalization, and parameter sensitivity analysis [41]. Despite these advantages, it's important to remember that analytical models are usually based on initial assumptions that may not fully correspond to reality, serving as simplified representations of real cases.

An innovative approach to determining the fatigue life of metals was recently proposed by C. Kassapoglou [4], introducing closed-form expressions for the dissipated energy during cyclic loading and their fatigue lives for load ratios between 0 and 1. The main idea is that fatigue failure occurs when the total dissipated energy equals the energy density of the material, necessitating the presence of plastic strains during cyclic loading.

The four key assumptions made by Kassapoglou were presented in the Fatigue Life Models section of the Literature Review chapter. Referring to figures (2.5) and (2.6), the energy density of a material at failure follows curve (CGB) and is given by:

$$U_{df} = \sigma \varepsilon - \int_0^{\sigma} \varepsilon d\sigma \quad (3.1)$$

which can be written as:

$$U_{df} = \frac{\sigma_f^2}{2E_o} + \frac{nK}{n+1} \left(\frac{\sigma_f}{E_o}\right)^n \quad (3.2)$$

As described in paper [4], the goal is to determine the area enclosed in the “converged” cycle delineated by curve ( $A_i H_i B$ ) for the loading part and ( $B I_i A_i$ ) for the unloading part, as shown in the next figure.

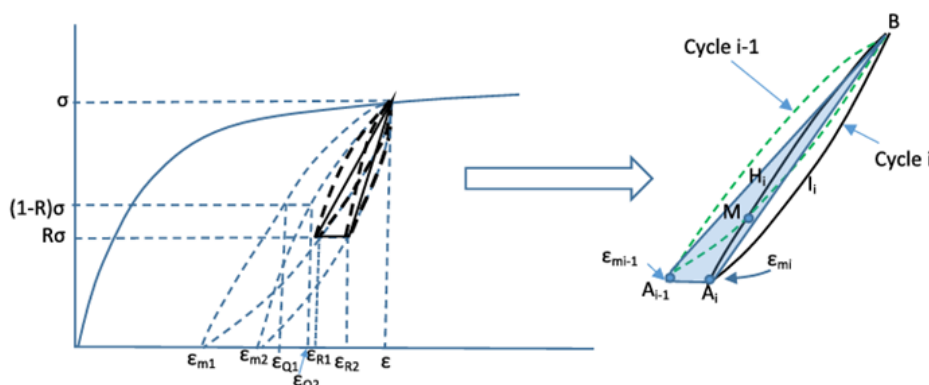


Figure 3.1: Fatigue cycles for  $0 \leq R < 1$ , [4]

The line  $(A_{i-1} B)$  divides the  $(i-1)$  cycle into two portions of equal area, according to the third assumption. Similarly,  $(A_i B)$  divides the  $(i)$  cycle into two portions with equal area. When energy dissipation occurs, the point  $A_{i-1}$  converges to  $A_i$ , making the area  $(A_{i-1} M A_i)$  zero. The area of triangle  $(A_{i-1} B A_i)$  then represents the dissipated energy during the stabilized unloading-reloading cycle. As a result, the total dissipated energy when the first two cycles are examined is given by:

$$T\Delta A = \frac{1}{2}(\sigma - R\sigma)(\varepsilon_{R_2} - \varepsilon_{R_1}) \quad (3.3)$$

where  $\varepsilon_{R_1}$  and  $\varepsilon_{R_2}$  indicate the residual strains when the loading ratio  $R$  is not zero. A fifth assumption to simplify the model is that “the shape of the unloading curve is the anti-symmetric one of the loading curve for a loading ratio equal to zero.” This assumption avoids calculating  $K$  and  $n$  at each cycle when  $0 \leq R < 1$ .

Returning to the analysis in paper [4], the final expression for the dissipated energy between the first two cycles is given by:

$$T\Delta A = \frac{1}{2}\sigma\left(\varepsilon - \frac{\sigma}{E_o}\right)(1-R)^{n_1+1}\frac{n}{n_1}\left(1 - (1-R)^{n_2-n_1}\frac{n_1}{n_2}\right) \quad (3.4)$$

The coefficient  $n_i$  at each cycle can be determined using the recursion expression for the ratio  $n_{i-1}/n_i$  mentioned in [4]:

$$\frac{n_{i-1}}{n_i} = \frac{-3an_{i-1}^3 + n_{i-1}^3 + 2an_{i-1}^2 + an_{i-1} - 2n_{i-1}^2 + n_{i-1}}{-2a^2n_{i-1}^3 - 4a_i^2n_{i-1}^2 - 2a^2n_{i-1} + 3an_{i-1}^2 - 2an_{i-1} - a - n_{i-1}^2 + 2n_{i-1} - 1} \quad (3.5)$$

where:

$$\alpha = \frac{E_o\varepsilon}{\sigma} \quad (3.6)$$

Due to the great sensitivity of the hardening exponent  $n$ , it is preferred to work with the limiting case where the ratio  $n_{i-1}/n_i$  has stabilized, given by:

$$\lim_{x \rightarrow \infty} \frac{n_{i-1}}{n_i} = \frac{1}{2}a^{-1}(3 - a^{-1}) \quad (3.7)$$

Additionally, for a large number of cycles,  $n_{i-1}$  and  $n_i$  become large and close in magnitude, so it can be assumed that:

$$(1-R)^{n_i-n_{i-1}} \approx 1 \quad (3.8)$$

Finally, the dissipated energy per cycle when the convergence of  $A_{i-1}BA_i$  occurs can be determined using the following expression:

$$T\Delta A = \frac{1}{8}\beta(1-\beta)^2(2-\beta)(3-\beta)(1-R)^{n_1+1} \quad (3.9)$$

where

$$\beta = \alpha^{-1} = \frac{\sigma}{E_o\varepsilon} \quad (3.10)$$

Consequently, the number of cycles to fatigue failure can be found by dividing the total energy density  $U_{df}$  by the stabilized dissipated energy:

$$N_f = \frac{8U_{df}}{\sigma\varepsilon\beta(1-\beta)^2(2-\beta)(3-\beta)(1-R)^{n_1+1}} \quad (3.11)$$

in case  $R \neq 0$ , and

$$N_f = \frac{8U_{df}}{\sigma\varepsilon\beta(1-\beta)^2(2-\beta)(3-\beta)} \quad (3.12)$$

in case  $R = 0$ .

### 3.1.2. Adaption of the method to composite materials

As mentioned in research [4], it is assumed that no material exhibits a perfectly linear response, which would lead to non-zero plastic strains. There are always slight deviations from linear behavior that create plastic strains. This assumption underscores the importance of accurately measuring stresses and strains during experiments. Consequently, Kassapoglou attempted to create a consistent methodology for metals to convert stress-strain curves into usable data. Specifically, the 0.2% strain offset method was used to determine the yield stress and strain, and a complementary approach to the Ramberg-Osgood relationship was developed. The resulting expression is:

$$\sigma = E_o\varepsilon + \Theta\varepsilon^\theta \quad (3.13)$$

where the values of  $\theta$  and  $\Theta$  can be determined using the expressions found in [4]. The 0.2% strain offset method is not commonly used in composites so a new way to determine  $K$  and  $n$  values was developed. A similar approach can be applied for  $\theta$  and  $\Theta$  however, the last two terms are not required to determine the fatigue life of a material.

For this analysis, Matlab was used to replicate the stress-strain curves from various works in the literature, using the function *grabit*. This function allows the user to import an image (in this case, the curve), set the origin, the lower and upper bounds of the axes, and finally capture different points to replicate the curve (Appendix - A). As will be explained later, the optimization function *fmincon* was also used to determine the values of  $K$  and  $n$ .

Firstly, the same assumptions made by Kassapoglou are considered again. This means that even though the stress-strain curve of a composite material follows the Ramberg-Osgood stress-strain law, the dissipated energy during cyclic loading stabilizes after some time, and fatigue failure occurs when the dissipated energy per cycle equals the energy density of the material at failure. The area under the static stress-strain curve represents this energy, and the notation  $U_{df}$  is used to describe it. Beginning with

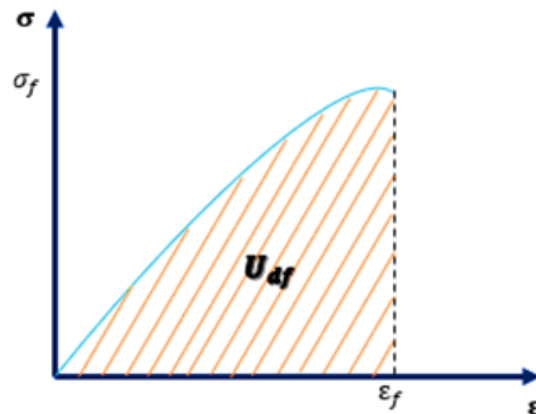


Figure 3.2: Energy density  $U_{df}$

the complementary approach, an expression for the static total energy  $U_{df}$  can be derived by integrating relation (3.13):

$$\begin{aligned} U_{df} &= \int_0^{\varepsilon_f} (E_o\varepsilon + \Theta\varepsilon^\theta) d\varepsilon \Rightarrow \\ U_{df} &= \frac{1}{2}E_o\varepsilon_f^2 + \frac{\Theta}{\theta+1}\varepsilon_f^{\theta+1} \end{aligned} \quad (3.14)$$

Having the stress-strain curve of the material, the area under the curve can be easily calculated using numerical integration. Consequently, expression (3.14) can now be expressed in relation to  $\Theta$  as:

$$\Theta = (\theta + 1) \frac{U_{df} - \frac{1}{2}E_o\varepsilon_f^2}{\varepsilon_f^{\theta+1}} \quad (3.15)$$

where  $\varepsilon_f$  is the strain at failure. Replacing equation (3.15) into equation (3.14) leads to the following formulation:

$$\sigma = E_o \varepsilon + (\theta + 1) \frac{U_{df} - \frac{1}{2} E_o \varepsilon_f^2}{\varepsilon_f^{\theta+1}} \varepsilon^\theta \Rightarrow$$

$$\sigma = E_o \varepsilon + (\theta + 1) \frac{U_{df} - \frac{1}{2} E_o \varepsilon_f^2}{\varepsilon_f} \left( \frac{\varepsilon}{\varepsilon_f} \right)^\theta \quad (3.16)$$

where only the parameter  $\theta$  is unknown. The estimation of  $\theta$  is based on the experimental data and the curve created using the “*grabit*” function, and it can be defined using a non-linear optimization technique to minimize the following cost function as described in research [33]:

$$f = \sum_{k=1}^n \left( \frac{\sigma_{i,j}^{\text{model}} - \sigma_{i,j}^{\text{exper.}}}{\sigma_{i,j}^{\text{exper.}}} \right)^2 \quad (3.17)$$

Having estimated the value of  $\theta$ , which must be positive, one can return to equation (3.15) and calculate the value of  $\Theta$ , which takes only negative values. Using this approach, the area under the stress curve of the complementary approach with respect to measured strains is always the same as the area under the measured stress-strain curve.

A similar approach can be followed for Ramberg-Osgood parameters  $K$  and  $n$ . It is crucial to calculate them in a way that the model curve represents the experimental data with high accuracy. An expression to calculate  $U_{df}$  is given in paper [4] as:

$$U_{df} = \frac{\sigma_f^2}{2E_o} + \frac{nK}{n+1} \sigma_f \left( \frac{\sigma_f}{E_o} \right)^n \quad (3.18)$$

which can be reformulated as:

$$\frac{U_{df} - \frac{\sigma_f^2}{2E_o}}{\sigma_f} = \frac{nK}{n+1} \left( \frac{\sigma_f}{E_o} \right)^n \quad (3.19)$$

where the left side of (3.19) can be calculated as all values are known. Therefore, by assuming that the left side of this equation is denoted as  $U$ , which has a specific value derived from the experimental data, equation (3.19) can be reformulated with respect to  $K$  as:

$$K = U \frac{n+1}{n} \left( \frac{\sigma_f}{E_o} \right)^{-n} \quad (3.20)$$

The Ramberg-Osgood relationship can now be written as:

$$\varepsilon = \frac{\sigma}{E_o} + U \frac{n+1}{n} \left( \frac{\sigma}{\sigma_f} \right)^n \quad (3.21)$$

with  $n$  being the only value that must be derived. The minimization of the same cost function as before was used but in terms of strains:

$$f = \sum_{k=1}^n \left( \frac{\varepsilon_{i,j}^{\text{model}} - \varepsilon_{i,j}^{\text{exper.}}}{\varepsilon_{i,j}^{\text{exper.}}} \right)^2 \quad (3.22)$$

When the value of  $n$  has been determined, expression (3.20) is used to calculate  $K$  to ensure that equation (3.18) is satisfied. A major parameter that highly affects the results is the value of initial stiffness  $E_o$ , and a statistical approach is also considered to make predictions. As it was presented before, the number of cycles until failure can be estimated using equations (3.11) and (3.12), where  $n_1$  is given by:

$$n_1 = -1 - 2\alpha \frac{\frac{n(n+1)^2}{(n-1)}}{(n-1)\beta - (3n+1)} \quad (3.23)$$

### 3.1.3. Statistical Approach

As described in paper [4], the method is highly sensitive to errors. Even the thickness of lines for the stress-strain curves can affect the results, not to mention the accuracy of strain measurements. A small change in the value of  $n$  significantly influences the prediction of life cycles, and one of the major parameters affecting the results is the initial stiffness  $E_o$ . An additional difficulty for this sensitive method is the variability of the mechanical properties of composite materials. Most test coupons are cut from a larger plate, which may have regions with different fiber volume fractions or misaligned fibers, either externally or within the material. Defects introduced during cutting or fabrication further contribute to variations in mechanical properties.

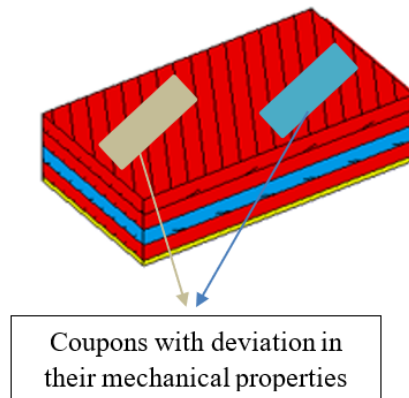


**Figure 3.3:** Variation of mechanical properties from region to region

This variability in the mechanical properties is the main reason for the significant differences in fatigue lives of small-scale coupons observed in many studies. Another issue is that, in addition to  $E_o$ , the failure stress  $\sigma_f$  and failure strain  $\varepsilon_f$  change for different specimens and, through them,  $U_{df}$  is also different. Because the scatter of strength and the failure strain are rarely available, it was assumed that parameter  $K$  and exponent  $n$  of Ramberg-Osgood relationship remain constant and can be determined based on the static stress strain curve of the coupon that is published. Therefore, a variation of the Young's modulus  $E_o$  based on the 90<sup>th</sup> and 10<sup>th</sup> percentiles (figure 3.4) when standard deviation of Young's modulus is available was applied. In cases where the standard deviation of the stiffness is not given, a  $\pm 10\%$  variation of the initial stiffness was used. By doing that, it is expected that the variation on the basis of only  $E_o$  changing will be a smaller portion of the total variation that would be seen if  $E_o, \sigma_f$  and strain  $\varepsilon_f$  were changed.

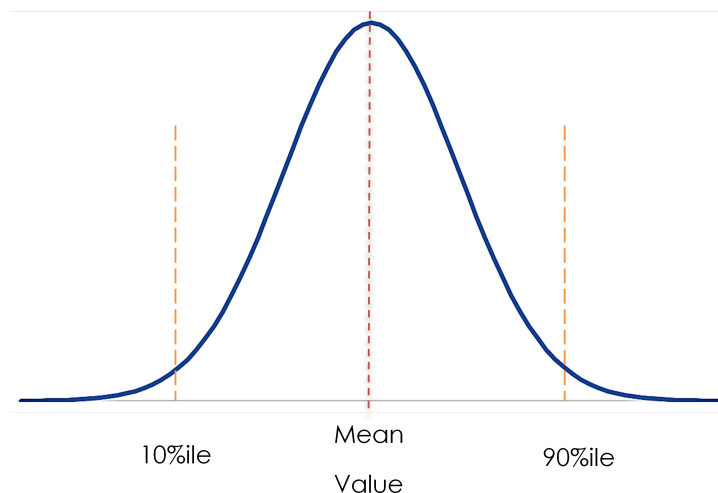


**Figure 3.4:** Normal distribution

### 3.2. Model Validation and Verification

The predicted lifespans from the developing method are compared with experimental data from the literature to verify the applicability of the proposed methodology to composite materials. To facilitate this comparison, the use of papers with both stress - strain curves from static experiments and their fatigue life cycles was necessary.

The first comparison is based on the work of Roundi et al. [42], who investigated four different laminates made of glass fiber with various stacking sequences. The second comparison is from Rafiqzaman et al. [43], where both open-hole and unnotched specimens made of woven glass fiber reinforced polymer laminates were tested for their mechanical performance under static and fatigue loading. The third comparison involves O'Brien et al. [44], who conducted tension fatigue tests on quasi-isotropic glass epoxy, graphite epoxy, and glass/graphite hybrid laminates. The predicted fatigue lifespans from the proposed model were compared with the graphite epoxy results from this study to verify the ability of the model to accurately predict the onset of edge delamination as reported by the authors. Finally, the predicted fatigue life cycles for interlaminar shear stress  $\tau_{13}$  for IM7/8552 carbon/epoxy unidirectional tape were assessed using published data by Makeev et al. [45]. The results from these comparisons are discussed in section (3.3).

#### Validation of the method compared with glass/epoxy laminates, [42]

Roundi et al. conducted an experimental investigation on four laminates with different stacking sequences:  $[0_2/90_2]_s$ ,  $[90_2/0_2]_s$ ,  $[0_3/90]_s$ , and  $[90_3/0]_s$ , [42] named in this comparison as coupon 1,2,3 and 4 respectively. These laminates were fabricated using the vacuum infusion process. Both static stress-strain curves and Wohler curves are presented in their work. The tests were conducted following the ASTM D3039/D3039M standard test method. For the fatigue experiments, tensile loads were applied at a constant frequency of 10 Hz with a load ratio  $R = 0.1$ , and the temperature recorded at 20°C. According to the authors, five tests were performed for each laminate during the static experiments, and approximately three specimens were used for fatigue lifespan characterization. The next two figures constitute the static stress-strain curves and the fatigue life cycle curves for the four different laminates as were published in paper [42],

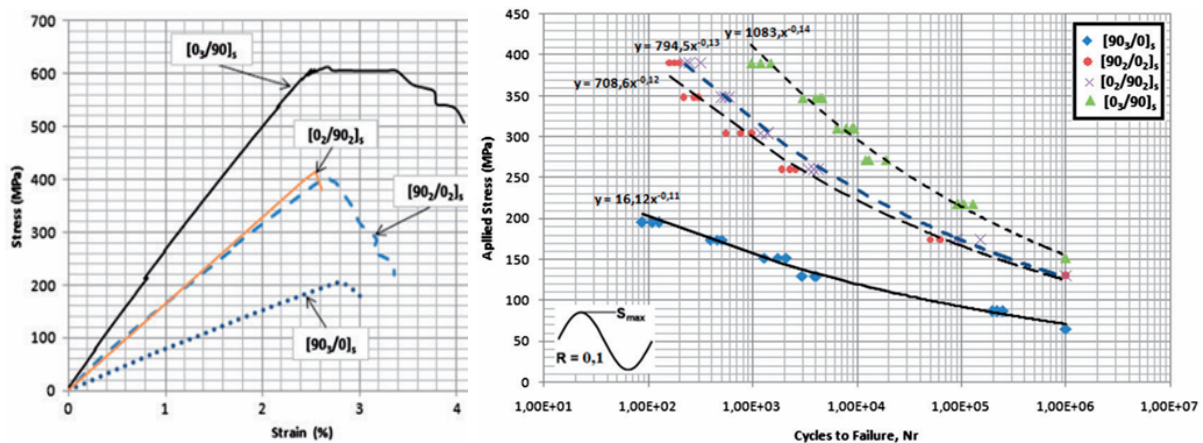


Figure 3.5: Figures obtained from paper,[42]

with their mechanical properties being displayed in the next table, where the mean values and the standard deviations are given for the initial stiffness  $E_o$  and for the tensile strength  $\sigma_f$ .

Table 3.1: Data imported from paper [42]

Laminates	Tensile Strength		Young's Modulus	
	$\sigma$ (MPa)	SD	E (GPa)	SD
Coupon 1	611	30	26.5	3.5
Coupon 2	415	25	18.5	2.5
Coupon 3	401	20	17.4	2.5
Coupon 4	205	10	7.8	1

where the different coupons correspond to the different laminates with the different stacking sequences. The methodology described below was applied to each laminate, but the case of  $[0_3/90]_s$  will be presented in detail to clarify the analytical process for the reader. Final predictions on a stress-log scale of fatigue life will be presented for all cases. Beginning with the initial stiffness, the following graph displays the initial slope of stress-strain data using the value of Young's modulus as referred by the authors.

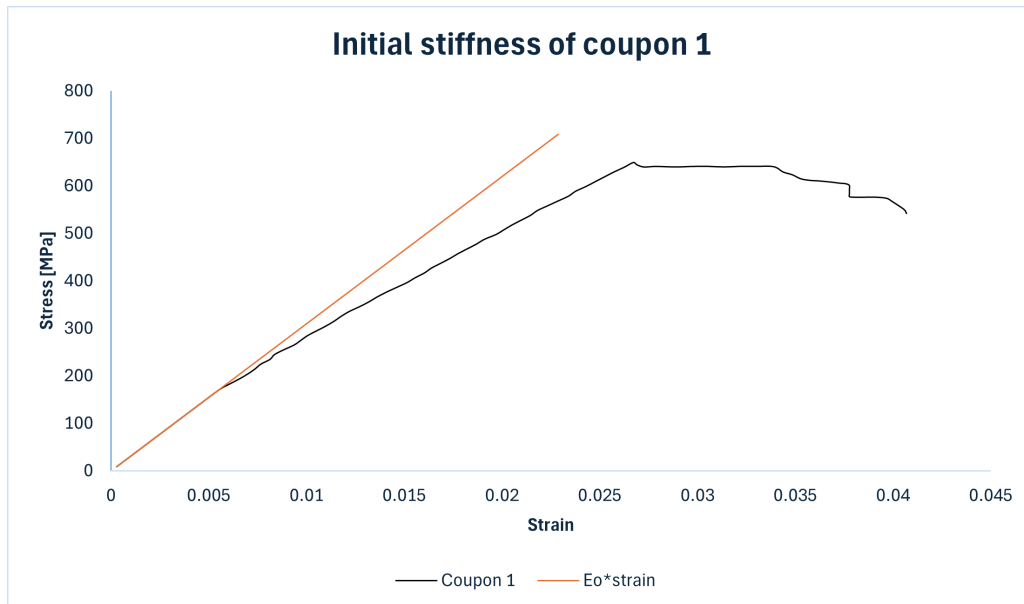


**Figure 3.6:** Initial slope of the experimental data

It is important to note that the values of  $\Theta$ ,  $\theta$ ,  $K$ , and  $n$  were estimated using the energy up to the tensile strength. For the calculation of fatigue life, the total energy under the stress-strain curve was used. The reason for determining the Ramberg-Osgood parameters using the energy up to the tensile strength is to accurately reproduce the curve of cyclic loading at the first cycle, providing the initial values needed.

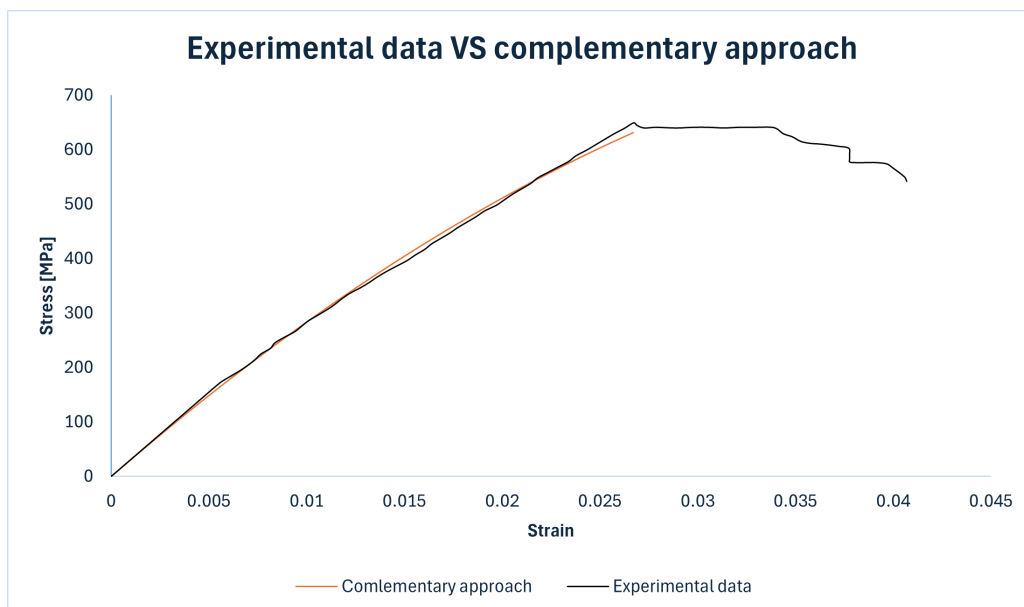


**Figure 3.7:** Complementary approach

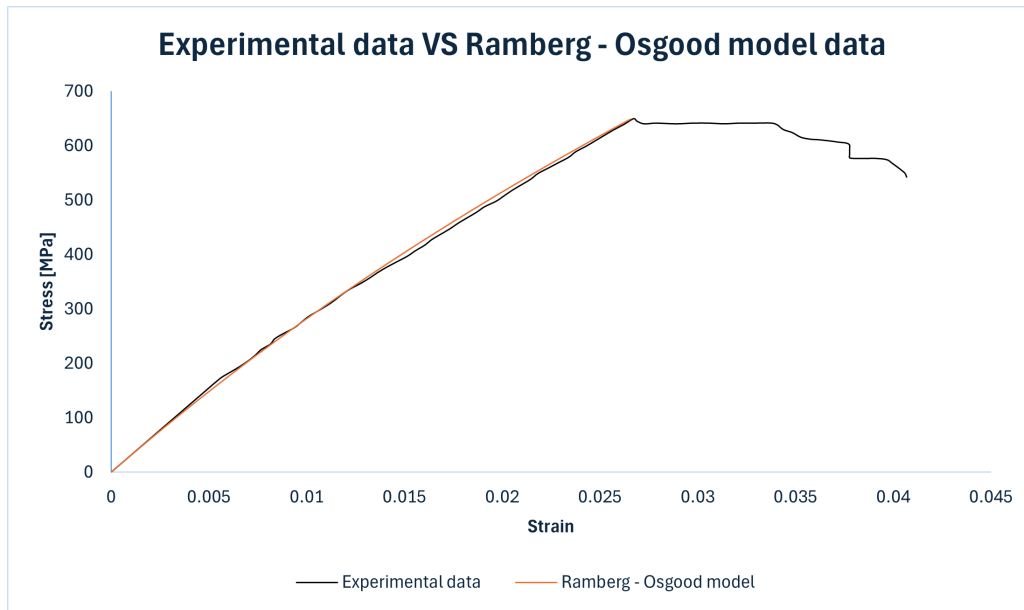


**Figure 3.8:** Ramberg-Osgood approach

with all required terms being demonstrated in the next table:

**Table 3.2:** Terms of the complementary approach and Ramberg - Osgood (RO) - first case

Complementary		RO Model	
$\Theta$ [MPa]	$\theta$	K	n
-5.7972e+07	3.7212	2.2682e+08	6.6043

Doing the same for the rest coupons, the next stress - life cycle curve were obtained. The 90<sup>th</sup> and 10<sup>th</sup> percentiles of the coupons based on the provided data (standard deviation of the initial stiffness) can be found in the next table:

**Table 3.3:** 90<sup>th</sup> and 10<sup>th</sup> percentiles of Young's modulus - Roundi et al. [42]

	Mean Value [GPa]	90 <sup>th</sup> ile [GPa]	10 <sup>th</sup> ile [GPa]
<b>Coupon 1</b>	26.50	22.01	30.98
<b>Coupon 2</b>	18.50	15.30	21.70
<b>Coupon 3</b>	17.40	14.20	20.60
<b>Coupon 4</b>	7.80	6.52	9.08



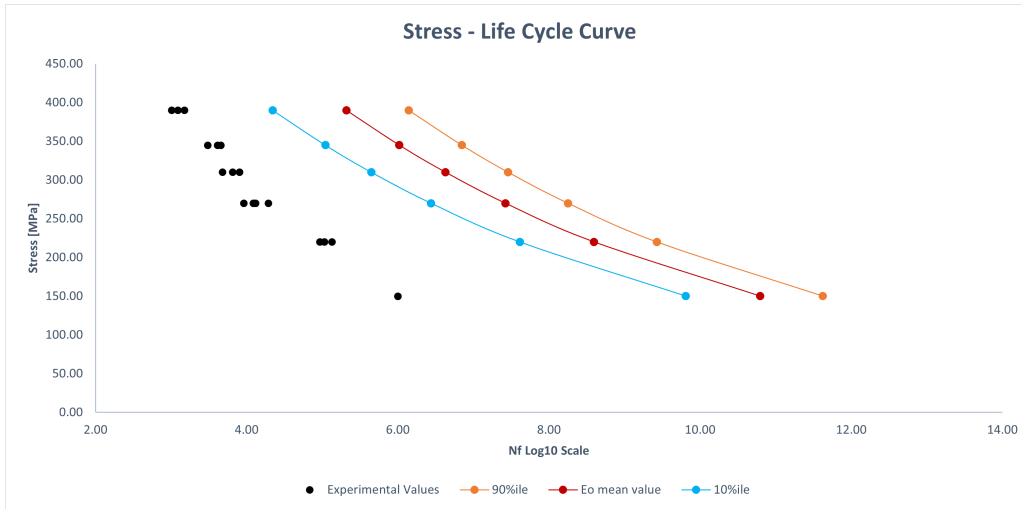


Figure 3.9: Comparison of experimental data with predictions for coupon 1

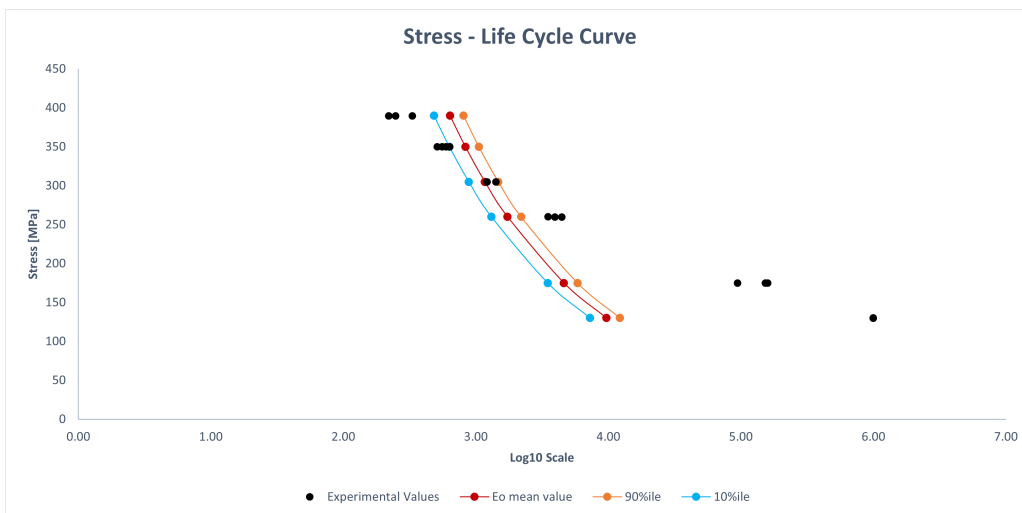


Figure 3.10: Comparison of experimental data with predictions for coupon 2

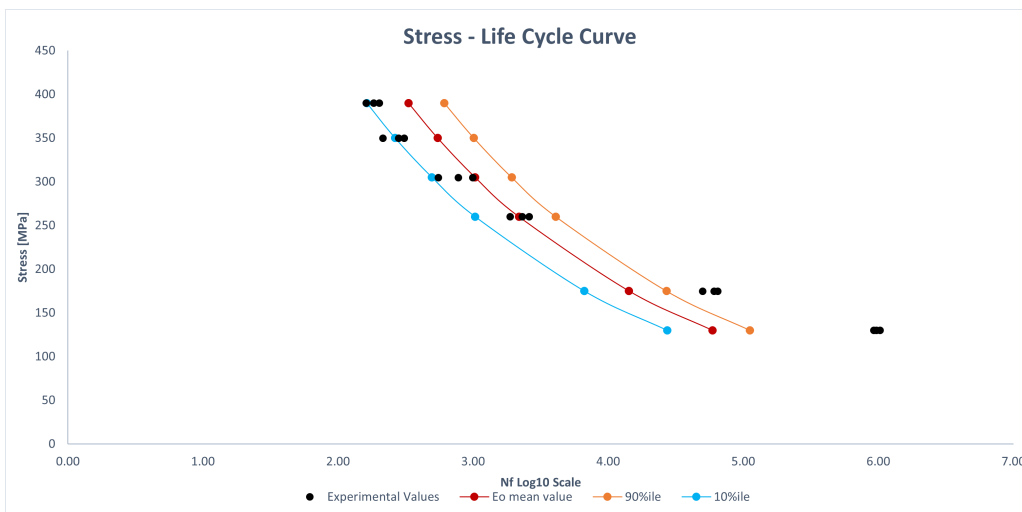
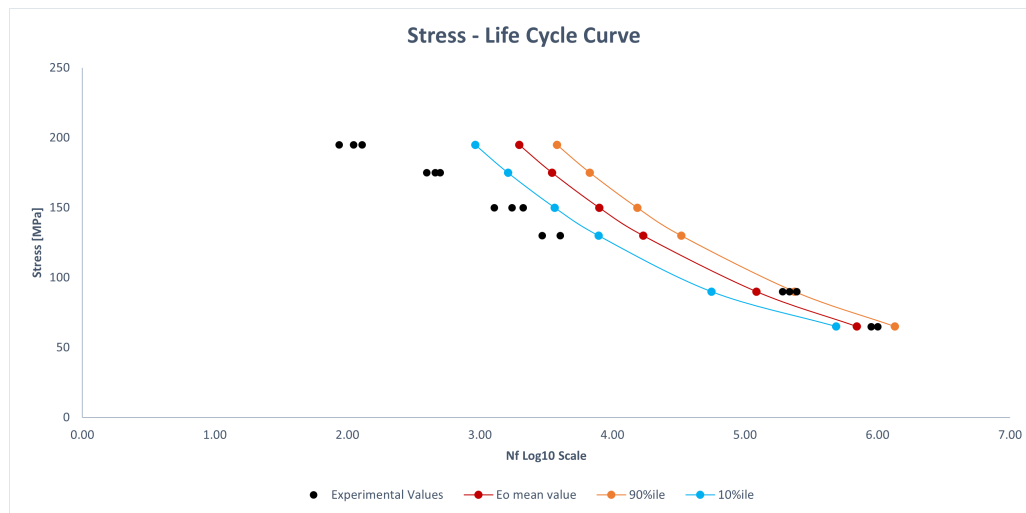


Figure 3.11: Comparison of experimental data with predictions for coupon 3



**Figure 3.12:** Comparison of experimental data with predictions for coupon 4

### **Validation of the method compared with woven glass fiber reinforced polymer laminates - notched specimens, [43]**

Five unnotched and five notched (open hole) specimens were tested in this study to investigate the mechanical behavior of chopped strand mat and woven roving E-glass laminates. The authors provided static stress-displacement curves and fatigue lifespan curves for both notched and unnotched specimens, highlighting the significant impact of the hole on the strength of the coupons. Specifically, the average strength of the notched specimens was approximately 60 MPa, while the strength for the unnotched coupons was 93 MPa. The average Young's modulus measured by Rafiquzzaman et al. was 2278 MPa for the unnotched specimens and 3657 MPa for the notched specimens. Cyclic loading was also applied to a set of coupons under a load ratio of  $R = 0$  at frequencies of 1 Hz, and under room temperature conditions. The displacement rate was 2 mm/min. To convert the displacements into strains, an initial length of 100mm was assumed to obtain an average Young's modulus close to what was mentioned by the authors. The recorded data can be seen in the next two figures:

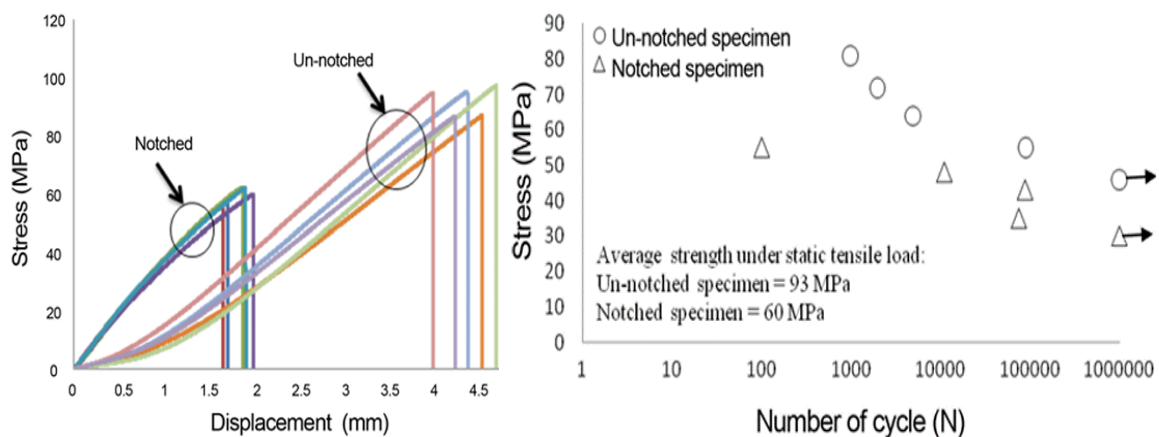


**Figure 3.13:** Figures obtained from paper,[43]

The experiments were conducted according to ASTM D3039 standards. Notched specimens were tested in this study because, as shown in the first graph of (3.13), the unnotched curves exhibit slippage at the beginning, which affects the estimated values and consequently the predictions. As before, the resulting curves from one notched specimen will be presented; however, all specimens were used to make predictions, and their geometric mean value curve will be presented here as every curve for each specimen is known. As described before, the same figures will also be presented for this case to determine the required terms to make predictions.

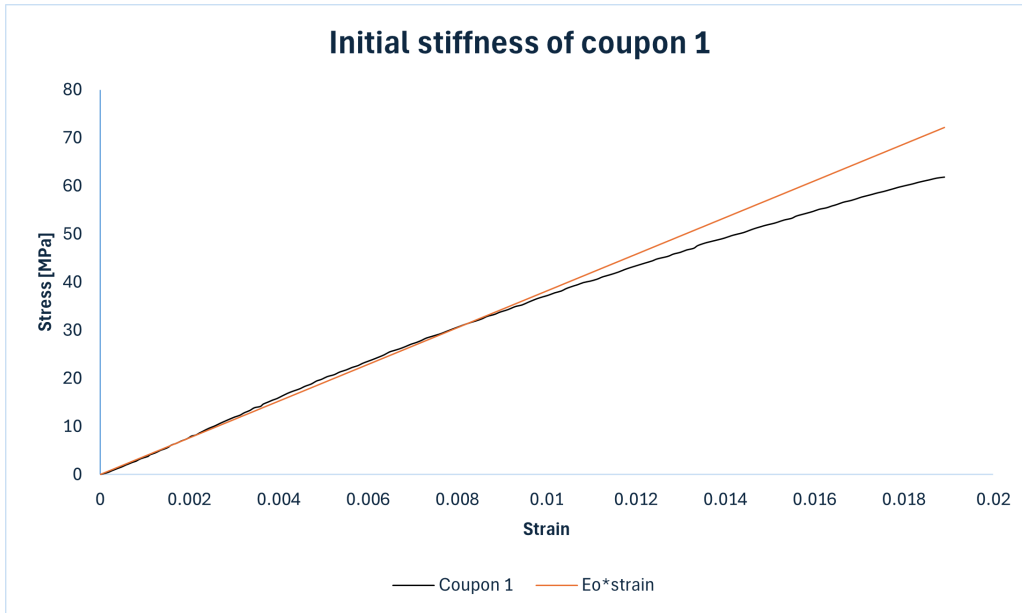


Figure 3.14: Initial slope of the experimental data

with  $E_o$  having been determined to be equal to 3776.50 [MPa], and the terms of complementary approach and Ramberg-Osgood’s model being displayed in the following table:

Table 3.4: Terms of the complementary approach and Ramberg - Osgood (RO) - second case

Complementary		RO Model	
$\Theta$ [MPa]	$\theta$	K	n
-8.8793e+07	4.0092	8.57e+05	4.7461

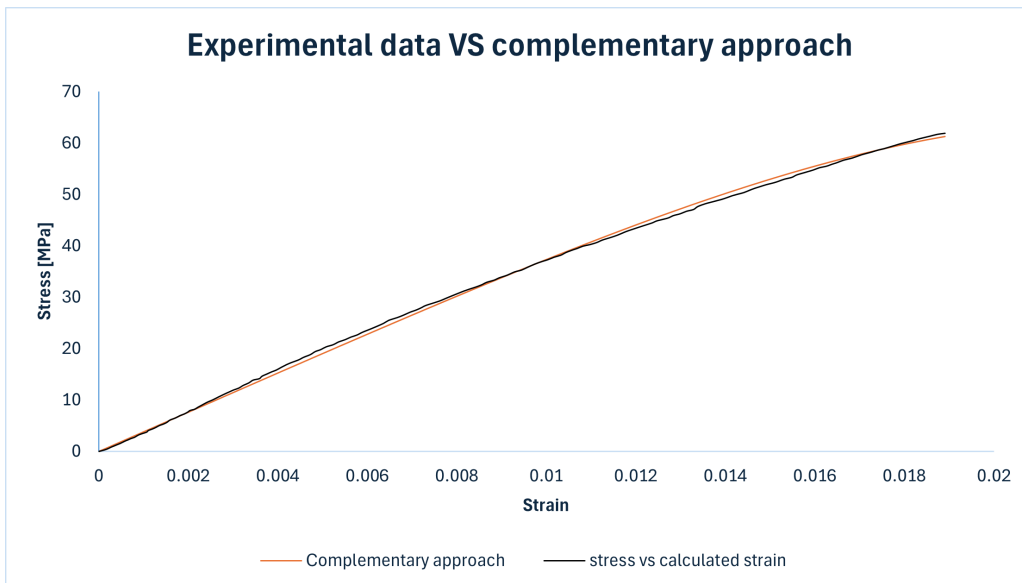
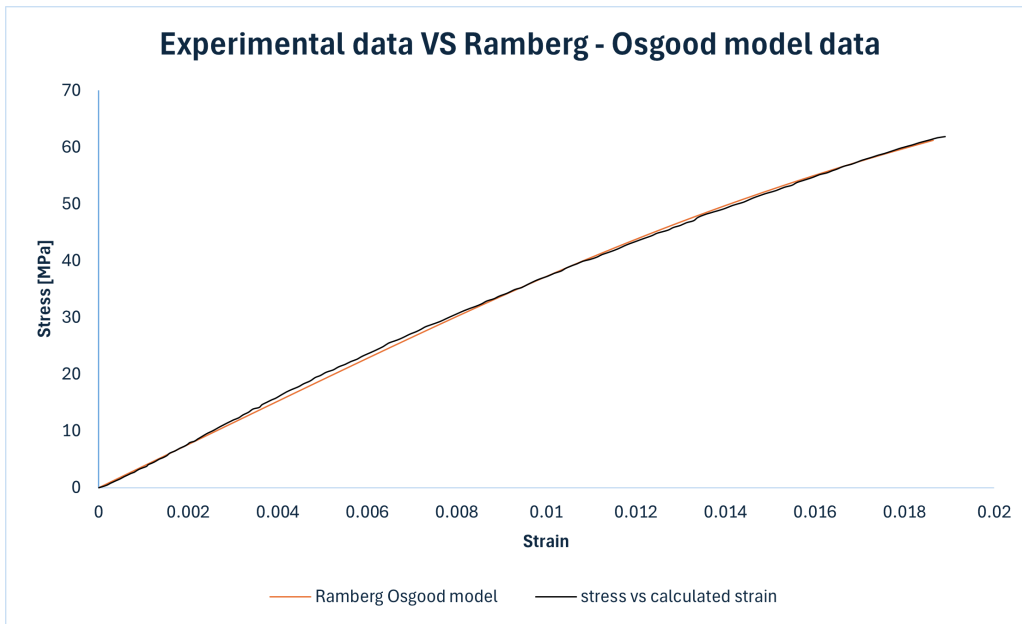
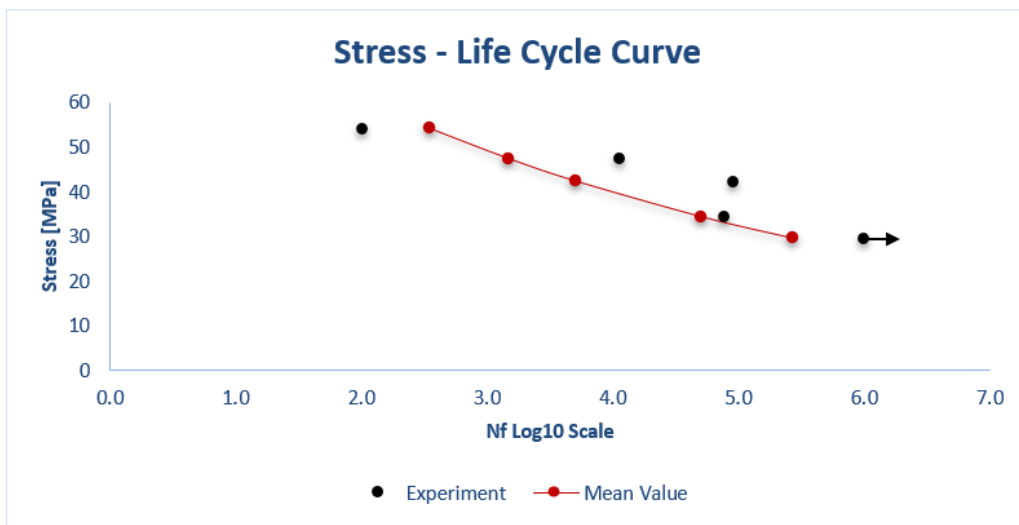


Figure 3.15: Complementary approach



**Figure 3.16:** Ramberg-Osgood approach

The predicted life curve was determined by using the geometric mean of the predicted lifespans for each coupon at each stress level.



**Figure 3.17:** Comparison of experimental data with predictions using the geometric mean of the predicted lifespans from all specimens.

**Validation of the method compared with graphite/epoxy laminates, [44]**

O'Brien et al. [44], developed a methodology to predict the fatigue life of composite laminates based on stiffness degradation measurements, accounting for the accumulation of matrix cracks and delamination growth. For their analysis, tension fatigue tests were conducted on quasi-isotropic and orthotropic glass epoxy, graphite epoxy, and glass/graphite hybrid epoxy laminates. Data regarding graphite epoxy laminates from this work were used to investigate whether the developing method can predict the onset of delamination. The idea is that edge delamination onset is indicated in the stress-strain graph with the graphite epoxy curve, so the energy density up to this point can be considered to verify whether the behavior of graphite epoxy laminates can be accurately predicted.

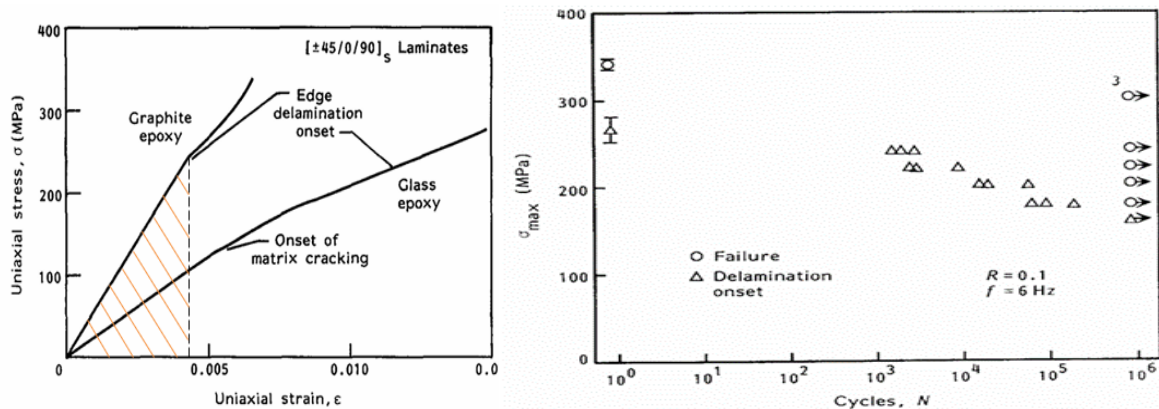


**Figure 3.18:** Figures obtained from paper,[44]

Unfortunately, there are no information about the standard deviation of the measured values in this work; therefore, only the mean value was considered again for the predicted lifespan. More specifically, the values that were used for the predictions are:

**Table 3.5:** Data imported from paper [44]

Material	Lay-up	Average $\epsilon_f$	Average $E_o$ [GPa]
Graphite	[±45/0/90] <sub>s</sub>	0.00663	57.5

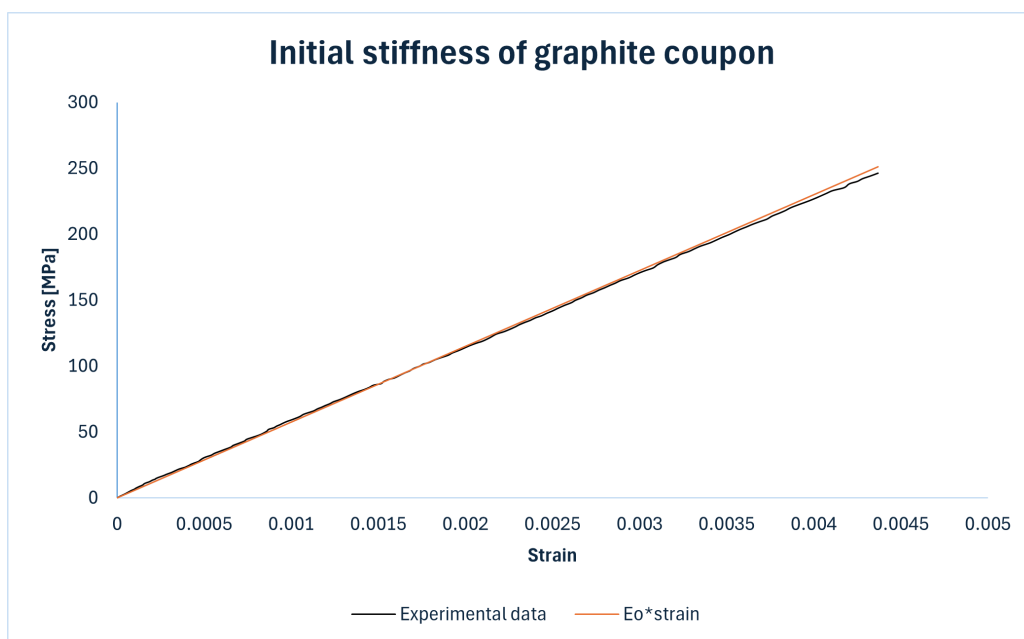


**Figure 3.19:** Initial slope of the experimental data

**Table 3.6:** Terms of the complementary approach and Ramberg - Osgood (RO) - third case

Complementary		RO Model	
$\Theta$ [MPa]	$\theta$	K	n
-5.165e+09	3.8589	1.5772e+05	3.9011

with the graphs of the two models being:

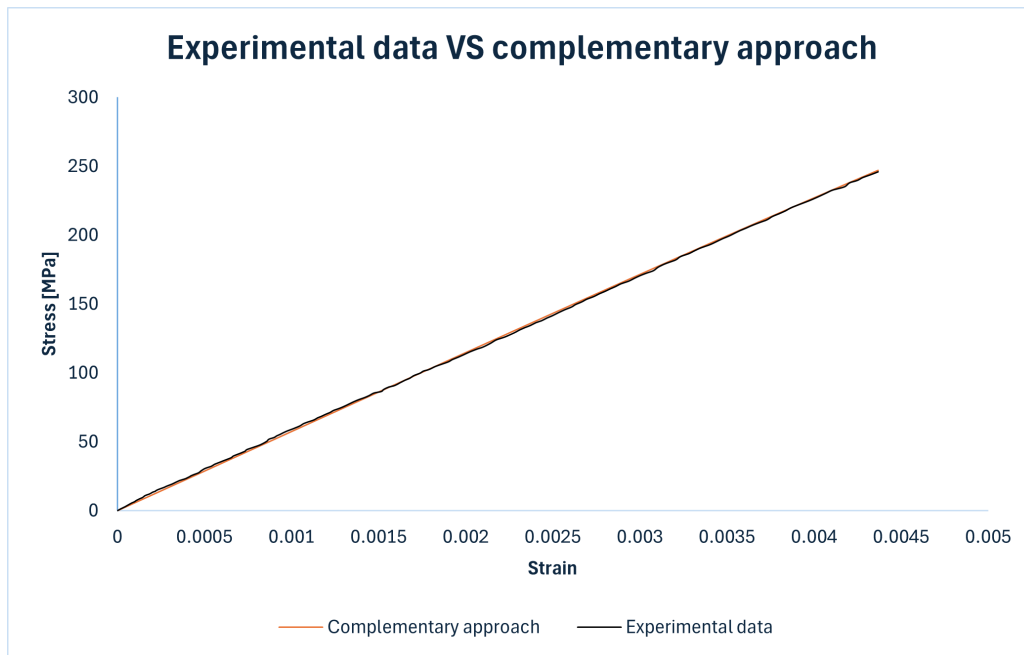


**Figure 3.20:** Complementary approach

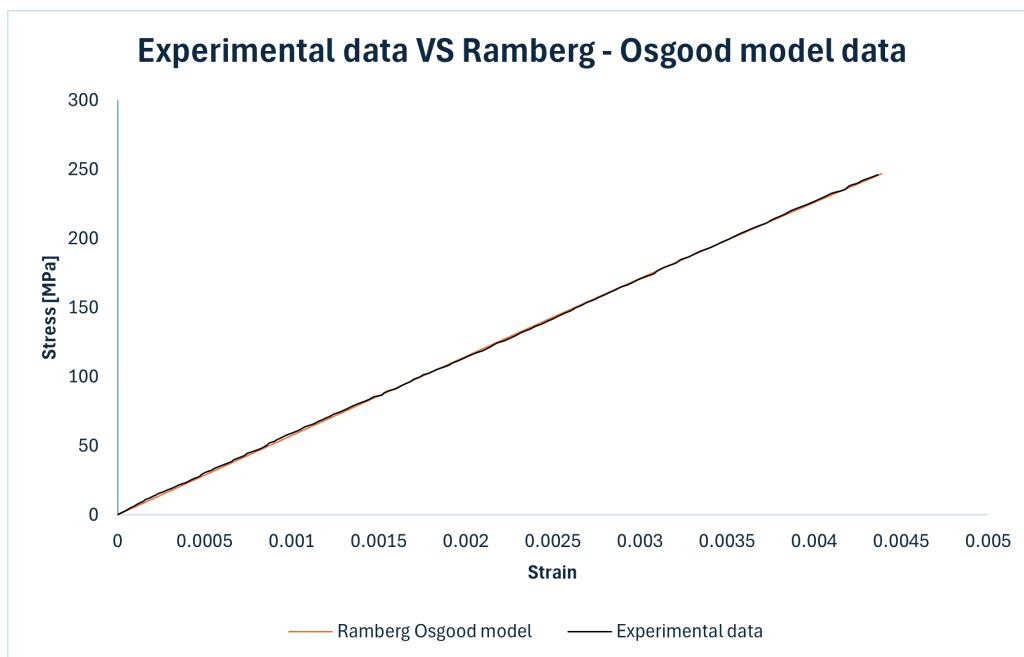


**Figure 3.21:** Ramberg-Osgood approach

and the predicted values for lifespan can be found in the next figure.

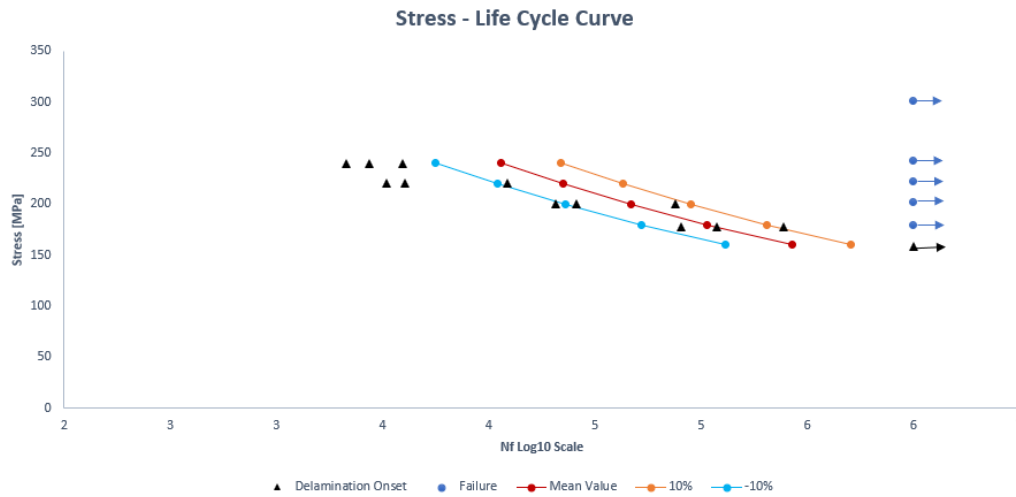


Figure 3.22: Comparison of experimental data with predictions

**Validation of the method compared with IM7/8552 epoxy data - interlaminar shear stress, [45]**

A significant challenge in understanding the failure of thick composite structures is the lack of data related to matrix-dominated properties, such as interlaminar ones. Makeev et al. [45] developed a methodology to measure nonlinear stress-strain relationships. In their research, experimental data for static and fatigue experiments are presented for coupons made of wavy IM7/8552 unidirectional laminas. Three coupons were subjected to static load experiments using a strain rate of 0.05 inches/minute, while three other coupons were subjected to cyclic loading under constant amplitude at a frequency of 10Hz and a load ratio of R=0.1. The experimental data for the static interlaminar shear tests and the fatigue lifespan are displayed below:

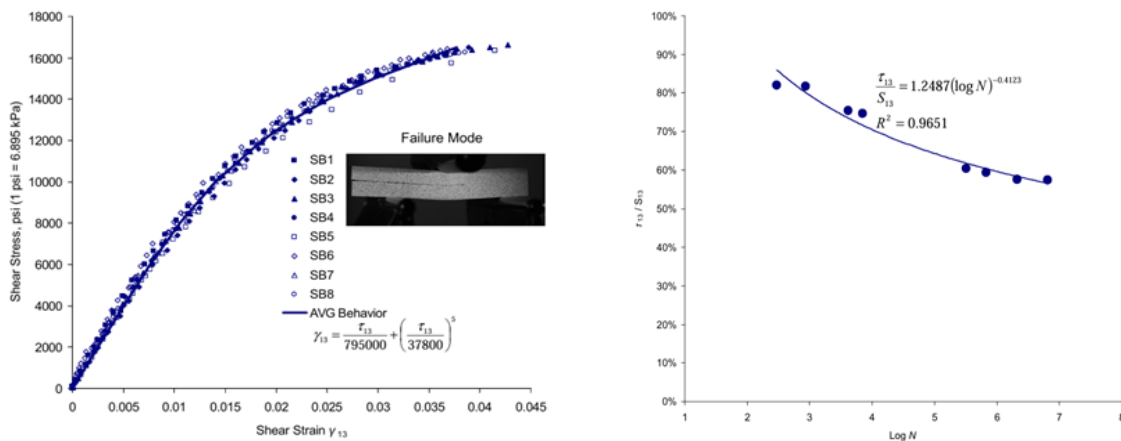


Figure 3.23: Figures obtained from paper,[45]

with both mean value and standard deviation being given in this work.

Table 3.7: Data imported from paper [45]

	Average Values	COV
Interlaminar Shear Strength [MPa]	113.8	1.59%
Interlaminar Shear Modulus $G_{13}$ [GPa]	5.48	5.57%

By following the same methodology described in Roundi's data (3.2), the terms of the complementary approach and those of Ramberg - Osgood law are:

**Table 3.8:** Terms of the complementary approach and Ramberg - Osgood (RO) - fourth case

Complementary		RO Model	
$\Theta$ [MPa]	$\theta$	K	n
-2.463e+06	2.9839	4.2117e+06	5.0063

with the  $E_{90\%ile}$  being estimated at 5871.17 [MPa] and  $E_{10\%ile}$  at 5088.83 [MPa].

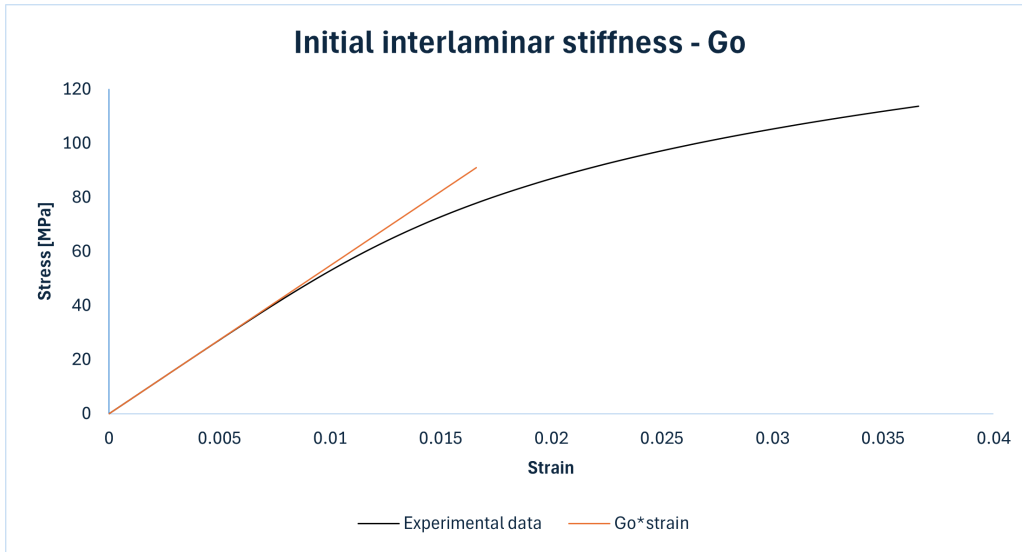


**Figure 3.24:** Initial slope of the experimental data

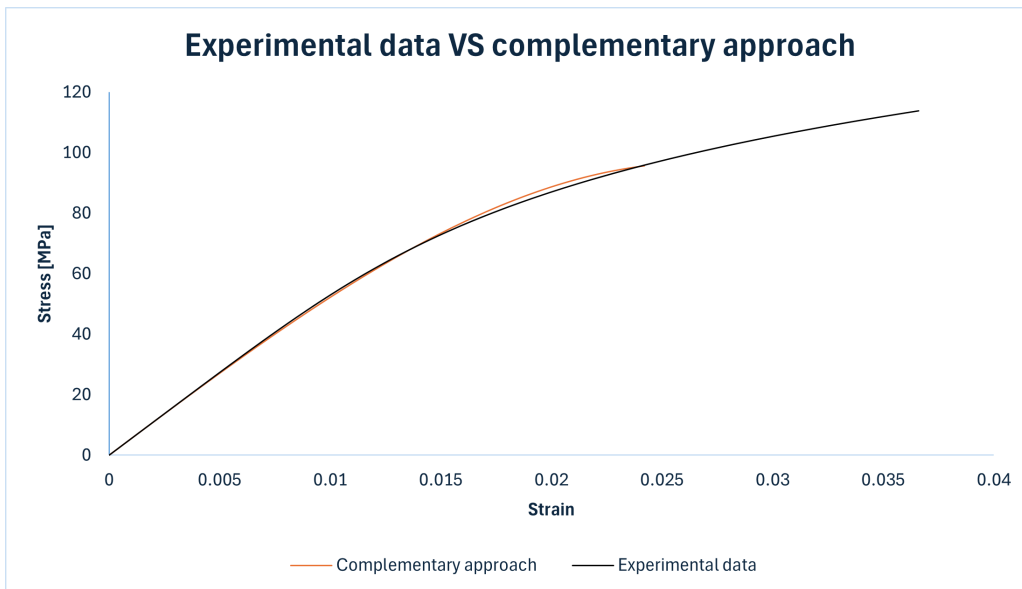


**Figure 3.25:** Complementary approach



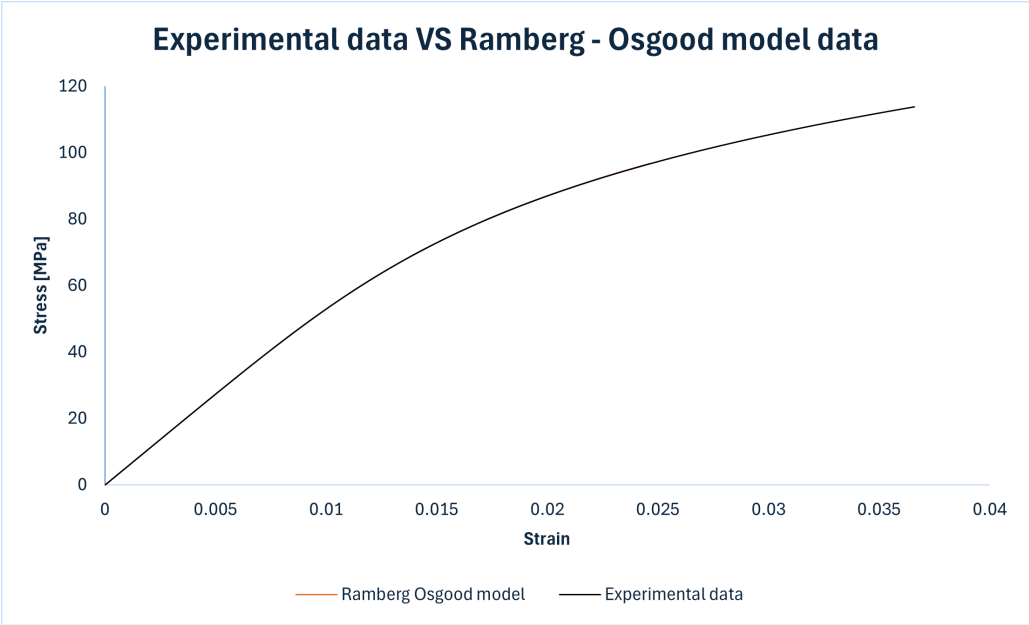


Figure 3.26: Ramberg-Osgood approach

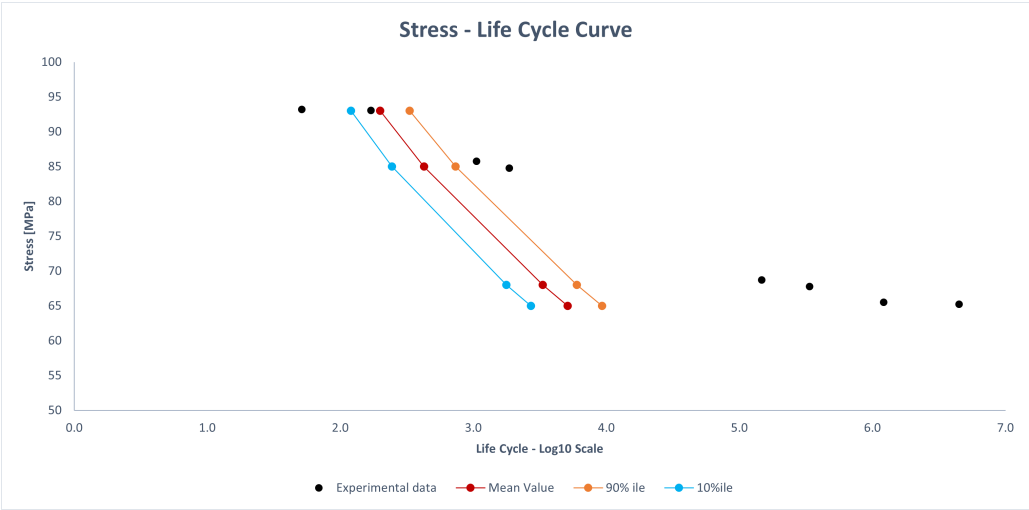


Figure 3.27: Comparison of experimental data with predictions

### 3.3. Conclusions

The conclusions drawn from the resulting stress-life cycle curves indicate that, in some cases, the predicted lifespans are close to experimental measurements, while in other cases, they are either overestimated or underestimated. The primary reason for this variance is the lack of discrete stress-strain data in the literature, which makes it difficult to determine the term  $\beta$  (3.10) with high accuracy. To address this issue, the function "grabit" was used to digitize the published data. However, this process can vary between individuals and significantly affect predictions, as the method is very sensitive. Moreover, having discrete stress-strain data allows for different sensitivity studies, such as finding the maximum slope from every 5, 10, or 15 successive points and using this as the initial stiffness  $E_o$ .

Regarding the comparisons made in this chapter, the deviations of the predicted values compared to the experimental results can be attributed to different factors. Specifically, in the case of Roundi et al., the coupons were fabricated using the RTM (Resin Transfer Molding) method, which is known to produce specimens with variations in their mechanical properties from region to region, especially due to potential differences in fiber volume fraction. These differences affect the term and, consequently, the predicted values.

The case of Rafiquzzaman et al. also involves uncertainties during the digitization process. After digitizing the data using "grabit" the displacements were converted into strains by dividing their values by a length that resulted in an average Young's modulus close to what was measured by the authors. This technique is not entirely accurate and is prone to errors in predicting lifespans. Nevertheless, an interesting observation in this research was when each specimen was examined independently.

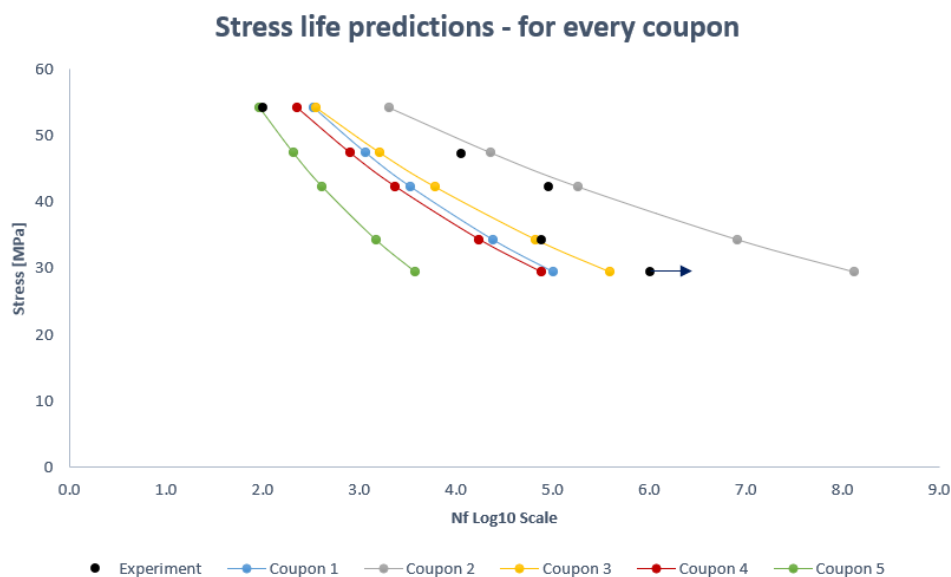


**Figure 3.28:** Predictions using every static stress strain curve of each coupon

As observed in the graph, the different inputs for each specimen resulted in curves that, at least at one stress level, the experimental results are predicted with high accuracy. This demonstrates the significant variability among different coupons and how this method can account for it. However, the geometric mean of these values led to figure (3.17), which shows predictions that are close to experimental values at some stress levels while indicating large deviations at other stresses.

For the last two cases, the following reasons may explain the discrepancies between the predicted lifespans and the published data. In the case of O'Brien et al., delamination onset was observed using a dye penetrant to enhance the X-ray images imported at the edges of the specimens. The combination of human error in measurements and the presence of local defects could explain the differences in results. However, the predictions for this study align well with the experimental results (figure 3.22). Finally, the wavy nature of the fibers in the coupons of Makeev et al. introduced local complexities, such as a combination of shear and bending in the curved fibers, which led to a load ratio different from what was applied to the specimen. Additionally, there is no mechanism that can be directly applied to correlate the stress concentration in a local region with the global stresses applied.

In conclusion, the main idea that fatigue failure occurs when the total dissipated energy density equals the total energy per volume of the material at failure seems valid. In simpler terms, it's like having a material with a specific storage capacity (total energy density) that depends on its condition (whether it is an intact specimen or already pre-loaded), and it loses a portion of this energy with every loading-unloading cycle. An interesting direction for future research would be to investigate how the dissipated energy varies through the cycles (at least in the first few cycles) to validate the recursion relationship of  $n_i/n_{i+1}$ , particularly regarding  $n_1$ , which is used when R is not equal to zero.

# Stiffness Degradation Model

## 4.1. Methodology

The investigation of the behavior of composite materials under cyclic loading is a complex topic, whether examining their fatigue lifespan or their stiffness degradation. The reasons for these complexities in composite materials are the numerous interactions between the differently oriented laminas and the matrix that holds them together and protects the fibers from environmental conditions. Many studies in the literature address both fatigue life and stiffness degradation models, accompanied by experimental results.

Delving further into the process of stiffness degradation, matrix cracks form at a very early stage of fatigue loading, especially near fibers oriented at 90 degrees. This is characteristic of a matrix-dominated lamina. The formation of these cracks leads to a deterioration in the mechanical properties, such as the strength and stiffness of the laminate. As it can be found in many works, stiffness degradation occurs in three stages. The first stage involves the formation of matrix cracks and the second stage involves the development of edge delaminations. Finally, the third stage is the transition to local damage progression. The main behavior observed in studies of stiffness degradation for fiber-reinforced composite materials is illustrated in the following figure:

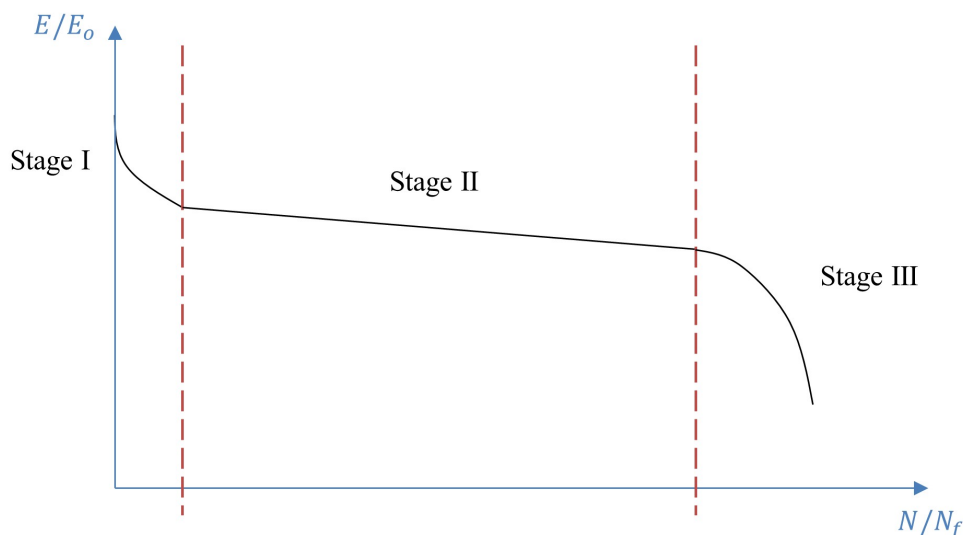


**Figure 4.1:** Stiffness degradation - general representation

One of the main goals of the following analysis is to extend the method used in the previous chapter for predicting fatigue lifespan, enabling the prediction of stiffness degradation directly without requiring additional experiments. To begin with, by applying the method used for life cycle predictions, the critical number of cycles where failure occurs is known, as is the converged dissipated energy. Consequently, the remaining energy density in every cycle  $U_{dm}$  can be determined using the following equation:

$$U_{dm} = U_{df} - mT\Delta A \quad (4.1)$$

At this point, after discussions with the supervisor the dissipated energy was translated into a pair of stresses and strains that follow the Ramberg-Osgood relationship, with the area under their curve corresponding to that energy. This pair of stresses and strains is displayed in the next figure, and the idea is that by adding a strip of area at every cycle  $m$ , the entire energy density of the material would be accounted for.

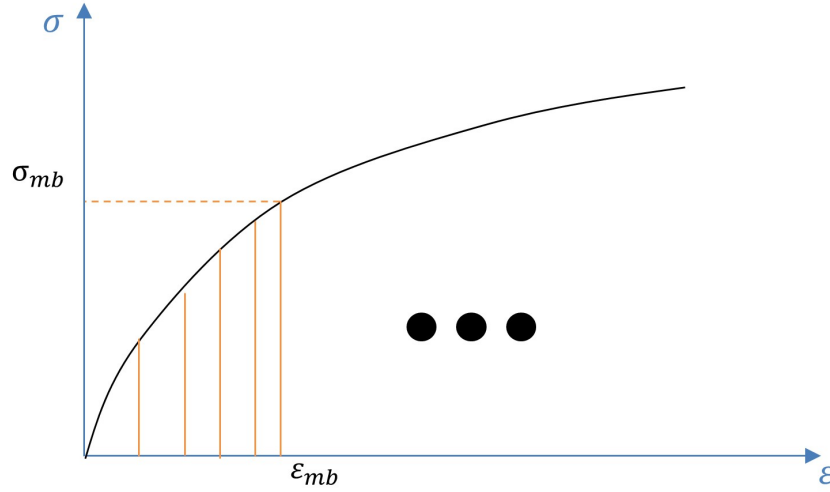


**Figure 4.2:** Pair of stresses and strains that correspond to dissipated energy

Based on that assumption the area under each strip in the above figure, is the same, and the strain  $\varepsilon_{mb}$  on the x-coordinate increases in a nonlinear fashion. To determine the value of  $\varepsilon_{mb}$ , the area under the stress-strain curve in the figure above must be equal to the dissipated energy at cycle  $m$ . This gives the condition:

$$\frac{\sigma_{mb}^2}{2E_o} + \frac{n}{n+1} K \sigma_{mb} \left( \frac{\sigma_{mb}}{E_o} \right)^n = m(T\Delta A) \quad (4.2)$$

which can be solved numerically to obtain  $\sigma_{mb}$  and consequently calculate the strain  $\varepsilon_{mb}$ :

$$\varepsilon_{mb} = \frac{\sigma_{mb}}{E_o} + K \left( \frac{\sigma_{mb}}{E_o} \right)^n \quad (4.3)$$

Having determined these parameters, the following two assumptions were made. Firstly, the residual strain  $\varepsilon_m$  was scaled relative to  $\varepsilon_{mb}$  such that when  $m$  reaches the fatigue life  $N_f$ , the residual strain equals  $\varepsilon_{mbfinal}$ , which corresponds to the total dissipated energy when the energy density of the material at failure has been covered.

$$\varepsilon_m = \varepsilon_{mb} \left( \frac{m}{N_f} \right) \quad (4.4)$$

Secondly, the strength is assumed to decrease linearly as  $m$  increases:

$$\sigma_{rm} = \sigma_f - \sigma_f \left( \frac{m}{N_f - 1} \right) \quad (4.5)$$

The following figure will help illustrate the entire methodology more clearly.

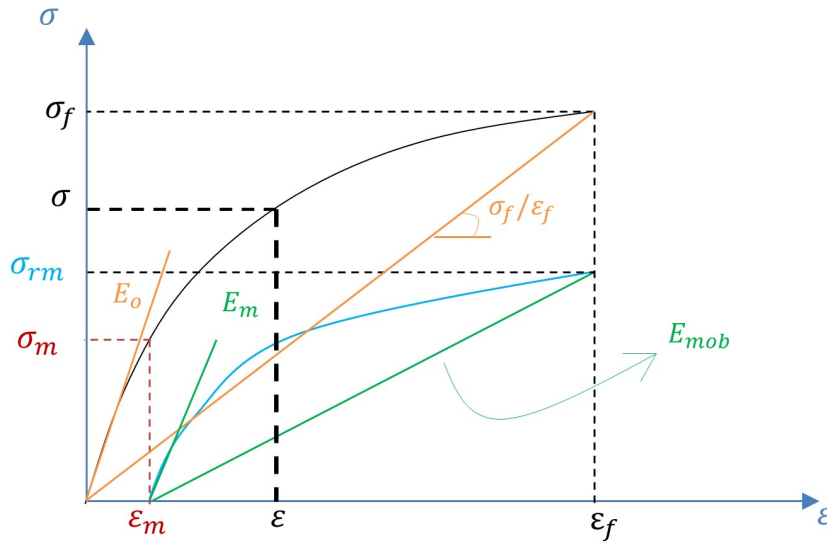


**Figure 4.3:** Definition of stiffness degradation terms

Looking at the previous figure, it can be easily understood that

$$E_{mob} = \frac{\sigma_{rm}}{(\varepsilon_f - \varepsilon_m)} \quad (4.6)$$

Then, an assumption was made that the tangent slope to the new stress-strain curve, divided by the slope of the line connecting the beginning of the curve to the point defined by the failure strain and the failure stress (residual strength), gives a constant number equal to the ratio of the same quantities for the static stress-strain curve:

$$\frac{E_m}{E_{mob}} = \frac{E_o}{\left(\frac{\sigma_f}{\varepsilon_f}\right)} \quad (4.7)$$

From this, the tangent modulus  $E_m$  can be determined and by comparing it to  $E_o$  will give the stiffness degradation:

$$\begin{aligned} \frac{E_m}{E_o} &= \frac{\frac{\sigma_{rm}}{(\varepsilon_f - \varepsilon_m)}}{\frac{\sigma_f}{\varepsilon_f}} \Rightarrow \\ E_m &= E_o \left( \frac{\sigma_{rm}}{\sigma_f} \right) \left( \frac{\varepsilon_f}{\varepsilon_f - \varepsilon_m} \right) \end{aligned} \quad (4.8)$$

In a similar manner, the secant modulus can be defined using the next formulation:

$$E_{sec_m} = \frac{\sigma - \sigma_{mb}}{\varepsilon - \varepsilon_m} \quad (4.9)$$

## 4.2. Validation of the method

### Comparison with experimental measurements provided in the works of Truong et al. and Vallons et al., [46] & [47]

These two papers are consecutive parts of a research study related to the evaluation of the mechanical behavior of multi-axial, multi-ply carbon fabric reinforced laminates. Tensile properties, along with stress-strain curves, are available in the work of Truong et al. [46], where quadriaxial, biaxial  $[+45/-45]$ ,  $[0/90]$  and unidirectional coupons were tested in different directions named as machine direction ( $MD$ ), biaxial direction ( $BD$ ), and cross direction ( $CD$ ).

Due to the research of Vallons et al. [47] on the determination of the stiffness degradation of biaxial coupons at  $[0/90]$  degrees, the case of biaxial coupons loaded in the biaxial direction ( $BD$ ) was selected for evaluation using the stiffness degradation model described earlier. This selection was made because this was the only case that a specific number of fatigue life was mentioned. However, as shown in the following figure, the graph related to the biaxial direction is not clear enough to gather all data accurately, and the provided lines are too thick, affecting the accuracy of the lifespan prediction model (which is highly sensitive, as previously described).

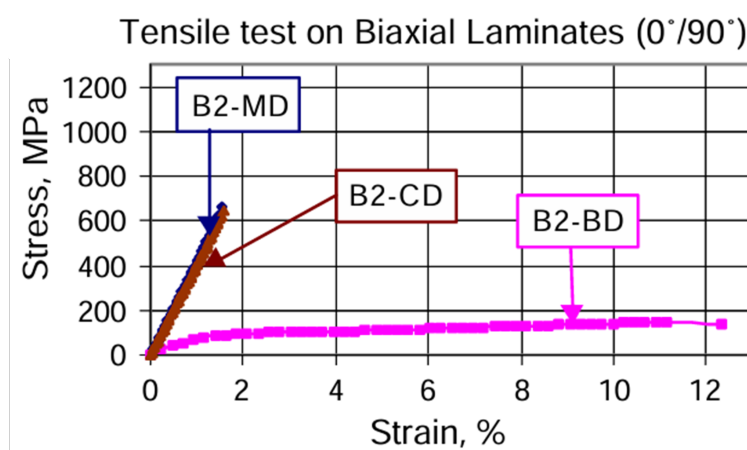


**Figure 4.4:** Figure taken from [46]. The examined curve is the pink one B2-BD.

Moreover, the Young's modulus that was finally calculated after the digitization was lower than what is mentioned in [46] and equal to  $5.4 [GPa]$  instead of  $9.1 [GPa]$ . Using the lifespan prediction model and trying to determine  $K$  and  $n$  that corresponds at least to first cycle, the following results were obtained:

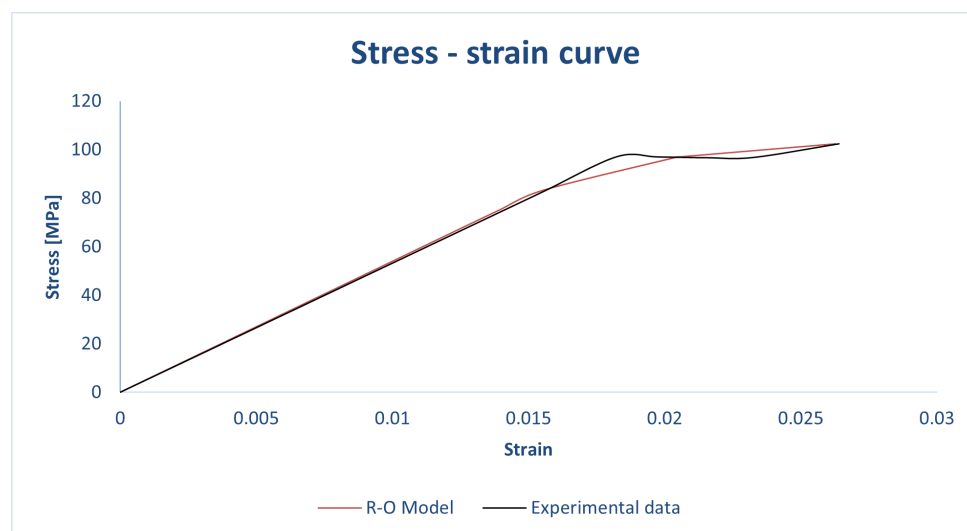


**Figure 4.5:** Stress strain curve: Model vs experiment from the origin to the applied stress.

with Ramberg – Osgood terms being displayed in the next table.

**Table 4.1:** R-O terms determined by the model

Ramberg - Osgood model	
<b>K</b>	1.80e+32
<b>n</b>	19.971

leading to a life prediction of  $N_f = 316642$  cycles which is 5.55% higher than what was measured in this research ( $N_f = 300000$ ). Using these values, the methodology proceeds as follows:

First, the recursion formula to determine the values of  $\frac{n_{i-1}}{n_i}$  is taken from the work of Kassapoglou [4], and the residual strains  $\varepsilon_{R_m}$  are calculated until convergence of  $\Delta\varepsilon_R$  occurs. The residual strains are determined as:

$$\varepsilon_{R_m} = \varepsilon - (1 - R) \frac{\sigma}{E_o} - (1 - R)^{n_m} \left( \varepsilon - \varepsilon_m - \frac{\sigma}{E_o} \right) \quad (4.10)$$

where  $\varepsilon_m$  is given by

$$\varepsilon_m = \left( \varepsilon - \frac{\sigma}{E_o} \right) \left( 1 - \frac{n}{n_m} \right) \quad (4.11)$$

Therefore, when  $\Delta\varepsilon_R = \varepsilon_{R_m} - \varepsilon_{R_{(m-1)}}$  becomes zero, it is known that  $\varepsilon_{R_{(m-1)}}$  is the last strain before the method has converged. All these strains are then scaled to  $\varepsilon_m$  as described in equation (4.4). Next, expressions (4.1) and (4.5) are used from the point of convergence to the point being examined. The following step involves determining the stresses and strains corresponding to the dissipated energy  $\sigma_{mb}$  and  $\varepsilon_{mb}$ . Consequently, equations (4.2) and (4.3) are applied, leading to the following results:

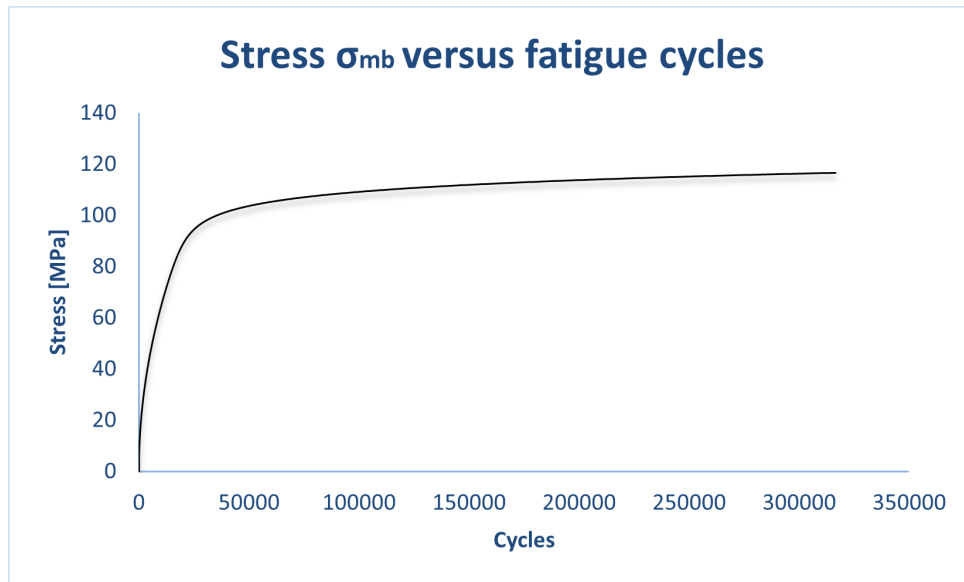


**Figure 4.6:** Residual stress that corresponds to dissipated energy



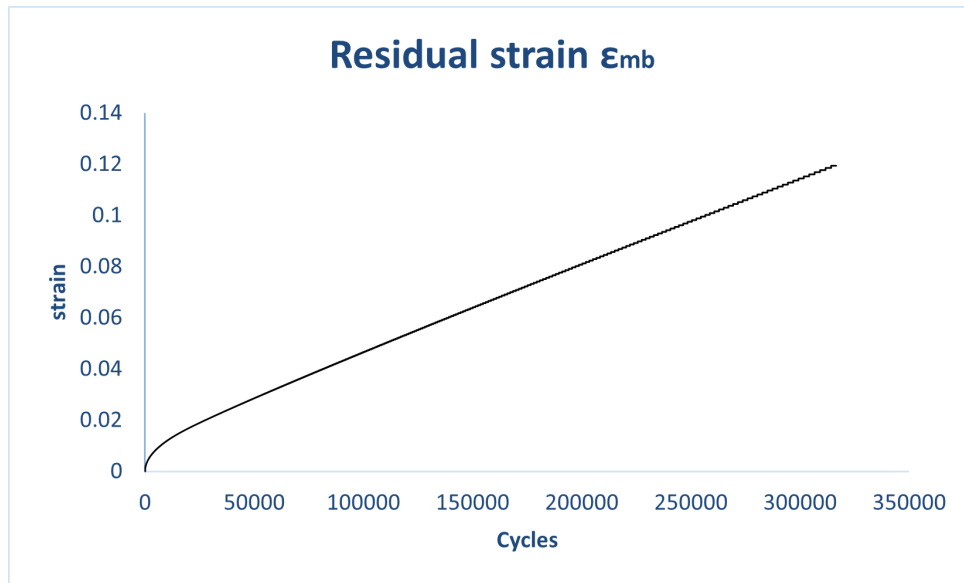


**Figure 4.7:** Residual strain that corresponds to dissipated energy

with the first figure denoting the way that stresses vary through the cyclic loading and the second figure the way that strains vary through fatigue lifespan. The following curve shows the initial stress strain curve made by  $\sigma_{rm}$  and  $\epsilon_m$  as the whole energy density was used for this example:

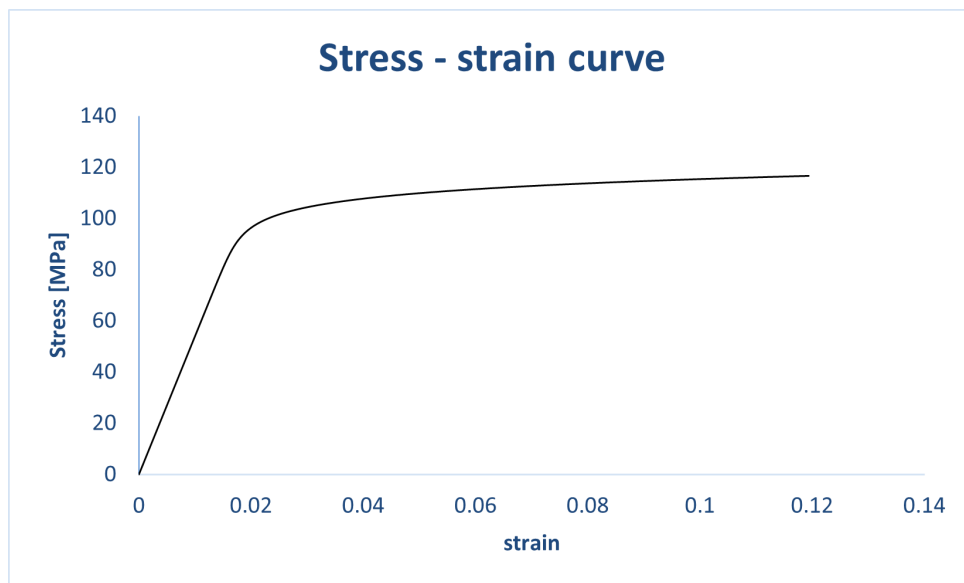


**Figure 4.8:** Stress ( $\sigma_{mb}$ ) strain ( $\epsilon_{mb}$ ) curve

Scaling  $\epsilon_{mb}$  to  $\epsilon_m$  again, the residual strains  $\epsilon_m$  changing in a nonlinear fashion as it was expected, and the graph is displayed below:

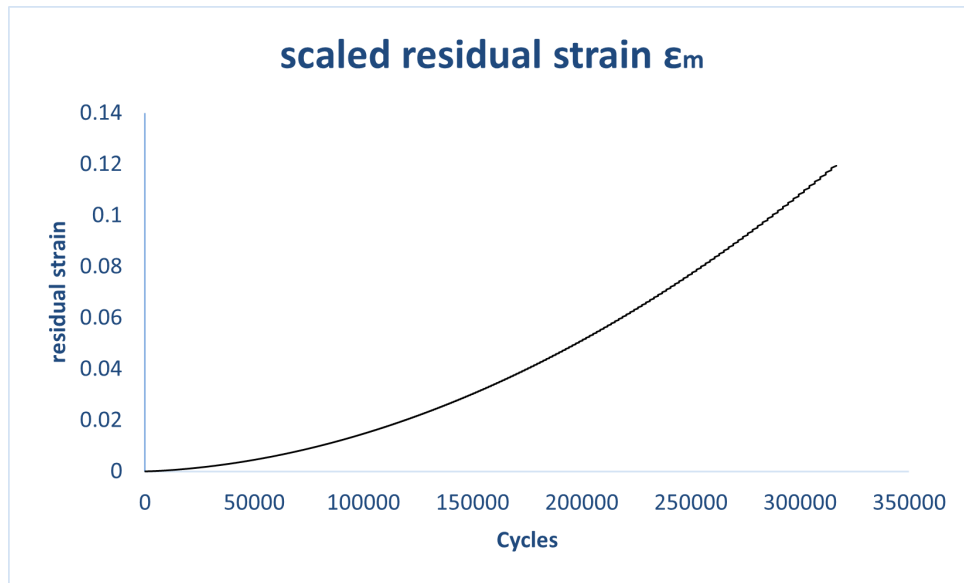


**Figure 4.9:** Residual scaled strain that corresponds to dissipated energy

By following this process, the last step is the application of (4.8) to determine the tangent modulus from the beginning until the end of the experiment. Vallons et al. [47] show measured the stiffness degradation at 30000 and 60000 cycles, so the predicted values and their results are demonstrated in the next table:

**Table 4.2:** Stiffness degradation: predicted values vs measured values

Stiffness degradation		
<b>Vallons et al. [47]</b>	D(30000) = 20.0%	D(60000) = 30.00%
<b>Predicted values</b>	D(30000) = 7.84%	D(60000) = 14.31%

#### **Comparison with experimental data provided in the doctoral thesis of Zhang, [2]**

The second research that was used to validate the methodology of stiffness degradation is the work of Zhang [2]. In his doctoral thesis, Zhang measured the secant modulus for dry and wet intact specimens, both after 10 thousand and 1 million cycles. Due to problems with slippage of the loading tabs during testing for the dry coupons, only the data from wet specimens were used for this comparison.

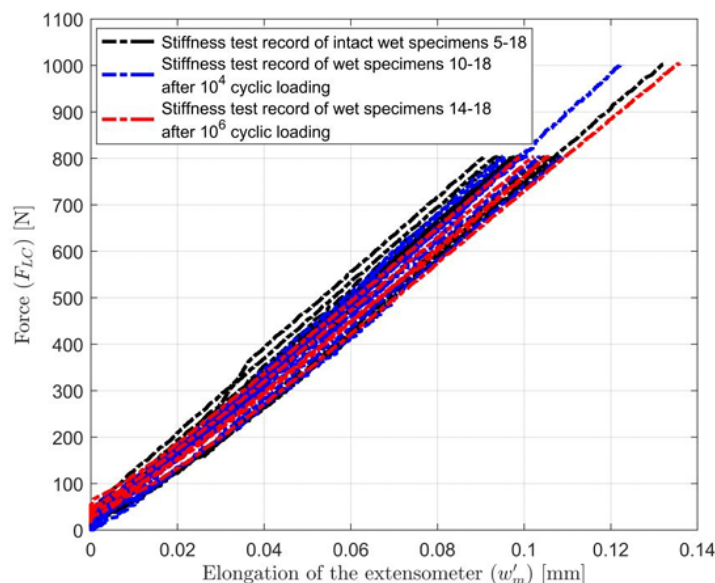


**Figure 4.10:** Experiments made by Zhang. This figure was taken from his thesis [2].

Like in the previous case, the same methodology was followed for Zhang's work, but this time the secant modulus was calculated. A key parameter in this analysis is that the static stress-strain curves are known as discrete points from the experimental process. However, as illustrated below, all coupons exhibited slippage at the beginning, and the stress-strain curves do not exactly follow the Ramberg–Osgood law. Instead, it appears that the stiffness increases as the load increases.

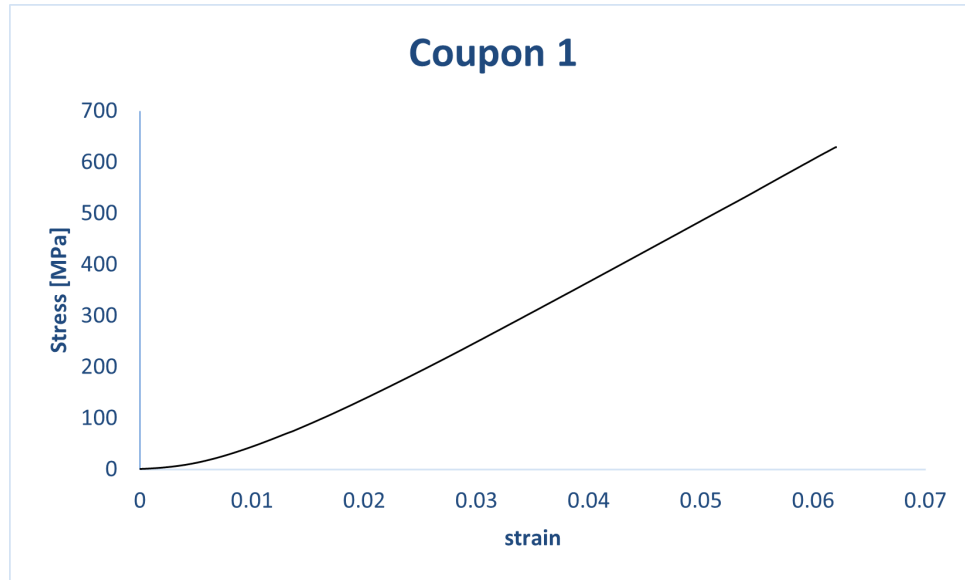


**Figure 4.11:** Stress strain curve of the first tested coupon in Zhang's thesis.

Therefore, the toe region ( $\varepsilon_T = 1.2\%$ ) was removed and replaced by the maximum slope found after 15 successive data points starting from the origin until the end of the experimental data. Subsequently, a straight line with this slope was used up to the strain  $\varepsilon_T = 0.012$ , and then the rest of the curve was translated to align with this straight line by subtracting each strain by  $\varepsilon_T$ . As a result, a “fictitious” stress-strain curve was created and used to make predictions for the fatigue life of the coupons and the stiffness degradation. The figure below presents this “fictitious” stress-strain curve:

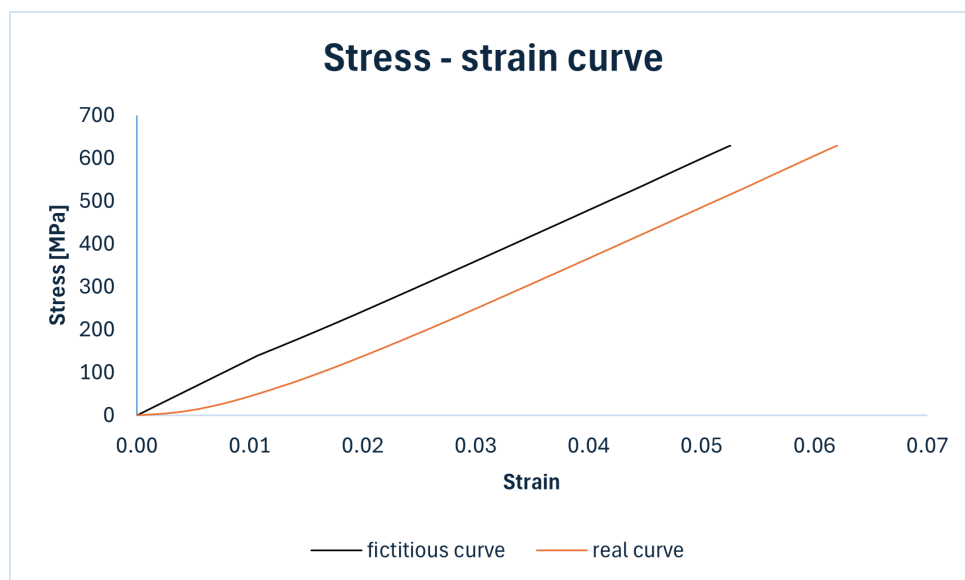


**Figure 4.12:** Fictitious stress strain curve for coupon 1.

The applied stress during the experiments was  $\sigma = 93.75$  [MPa] and the load ratio was  $R = 0.75$ . The same methodology was followed for all four coupons but the resultant stress strain curves and Ramberg – Osgood terms will be presented for only one coupon. After having applied the lifespan prediction

model, the new stress strain curve created by the Ramberg Osgood formula is denoted in the next graph compared to the real experimental data:

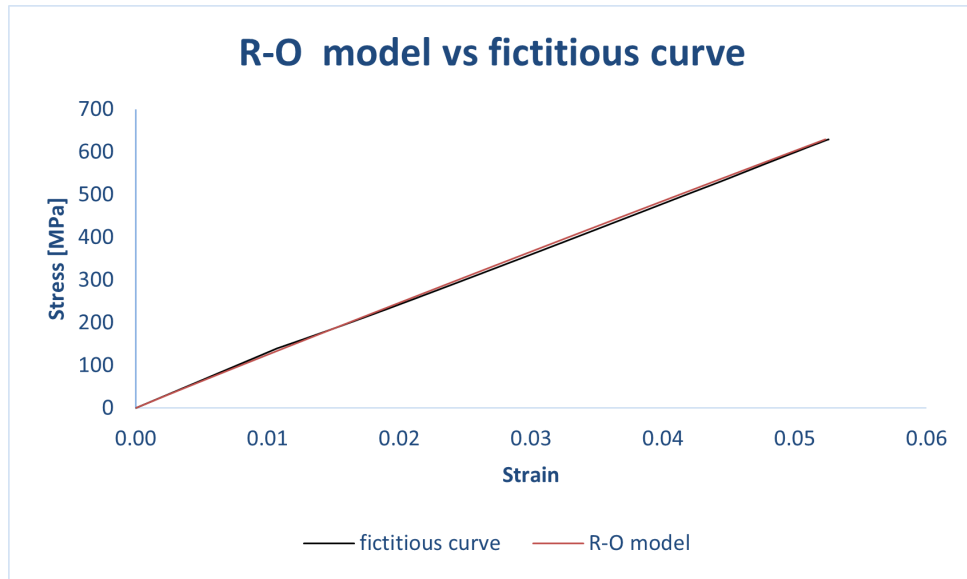


**Figure 4.13:** Ramberg - Osgood model vs fictitious stress strain curve.

with the values of  $K$  and  $n$  being displayed in the following table.

**Table 4.3:** R-O terms determined by the model - Zhang

Ramberg - Osgood model	
<b>K</b>	0.2964
<b>n</b>	1.3858

with the number of predicted cycles being  $N_f = 13.28$  billion cycles.

Moving on the stiffness degradation model, the same methodology that described for the previous case was followed here. Firstly, the residual strain where convergence occurred was determined and then  $\sigma_{mb}$  and  $\varepsilon_{mb}$  were calculated for 1 million cycles. The closer the value of exponent  $n$  to 1, the faster convergence occurs. The resultant figures are:

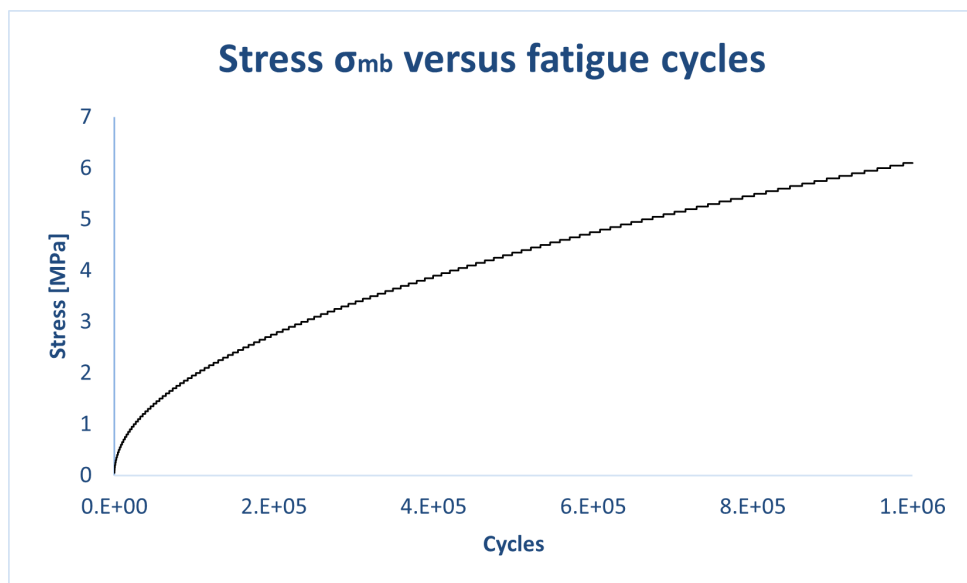


**Figure 4.14:** Residual stress that corresponds to dissipated energy

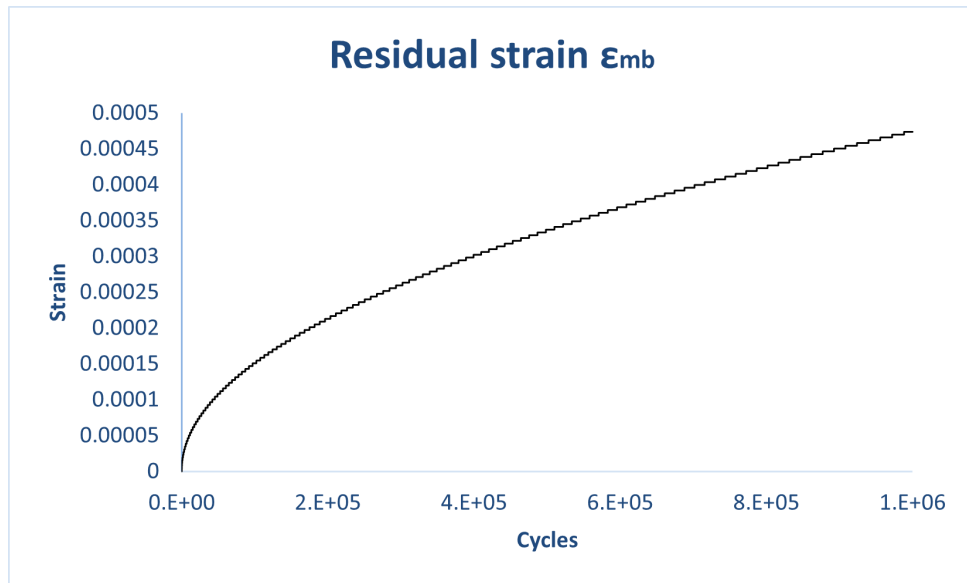


Figure 4.15: Residual strain that corresponds to dissipated energy

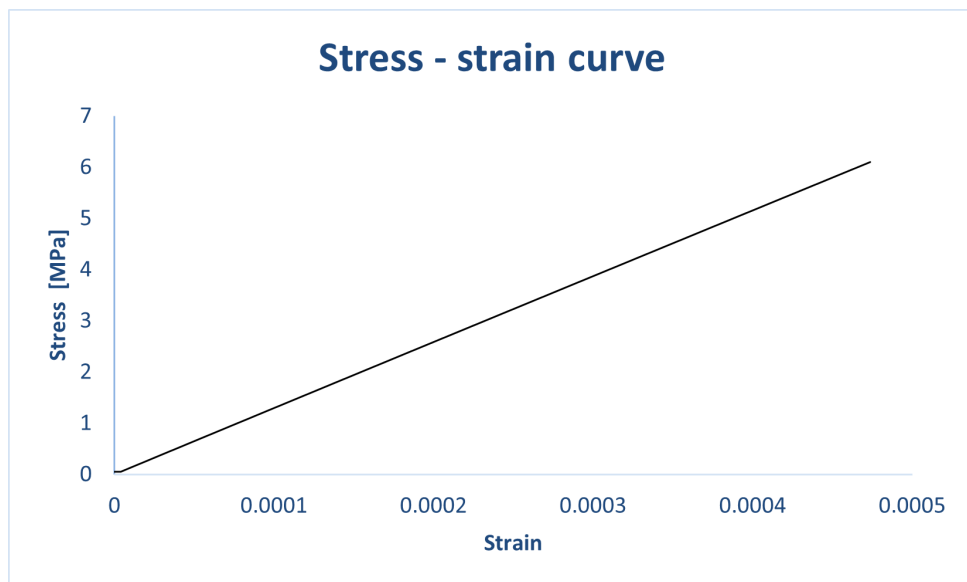
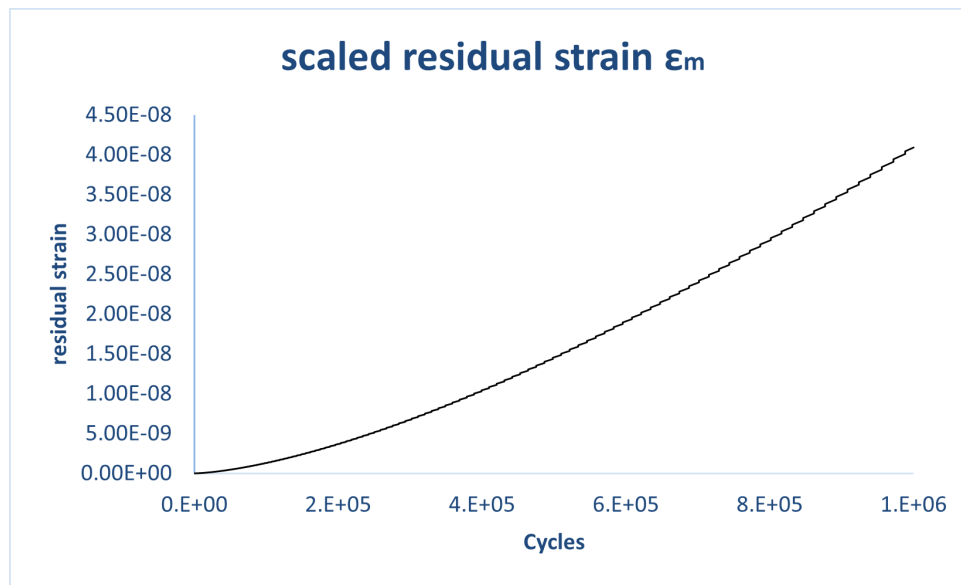


Figure 4.16: Stress ( $\sigma_{mb}$ ) strain ( $\epsilon_{mb}$ ) curve

with the last figure corresponding to the stresses and strains that led to the dissipated energy at 1 million cycles. Strains  $\epsilon_{mb}$  were scaled to  $\epsilon_m$  as in the previous cases, leading to the following curve:



**Figure 4.17:** Residual scaled strain that corresponds to dissipated energy

And finally, expression (4.9) was applied to evaluate the stiffness degradation of secant modulus. The results are:

**Table 4.4:** Predicted values of stiffness degradation model vs experimental values

Stiffness degradation (Secant Modulus)		
	10 thousand cycles	1 million cycles
<b>Coupon 1</b>	D = 0.587%	D = 5.976%
<b>Coupon 2</b>	D = 0.587%	D = 5.976%
<b>Coupon 3</b>	D = 0.694%	D = 7.203%
<b>Coupon 4</b>	D = 0.640%	D = 6.456%

so the comparison between the mean value of these results and the mean value that is provided by Zhang can be found in the following table:

**Table 4.5:** Comparison of mean values

Stiffness degradation (Mean Values)		
	10 thousand cycles	1 million cycles
<b>Zhang</b>	D = 0.6%	D = 6.7%
<b>Predicted values</b>	D = 0.6%	D = 6.4%

### 4.3. Conclusions

Stiffness degradation is an inevitable process resulting from the fatigue of a material. As explained in this chapter, developing a model to predict stiffness deterioration is commonly accompanied by data from experiments. This new proposed model continues the lifespan prediction model of Kassapoglou and provides results without needing extra experiments, as presented in (4.2 - a) and (4.2 - b), leading to results that are in good agreement with experimental measurements. Delving into more detail about the predicted values for the cases of Truong et al., Vallons et al., and Zhang, the following conclusions can be obtained.

In the first case of the biaxial coupons [0/90] subjected to biaxial loading [46], [47], the predicted results show a variation from the measured data. Specifically, the predicted stiffness degradation is almost half of what was measured for both examined cycles. One potential reason for this difference could be the difficulty in obtaining accurate stress-strain data from the static stress-strain curve (4.4). Additionally, there is a necessity for refining the lifespan prediction model to become a more robust method. Another potential reason could be the lack of data to perform a statistical analysis and calculate the lifespan and stiffness degradation for a range of coupons. Lastly, further investigation will be conducted to improve and correct this method.

In the case of Zhang, the results were more promising in terms of determining the secant modulus. However, a sensitivity study should be done to verify how this method is affected by differences in fatigue life and which terms are responsible for the changes. Finally, it has been proven that both the stiffness degradation and lifespan models work more efficiently with discrete stress-strain data than with digitized stress-strain curves.

# Finite Element Analysis

## 5.1. Description of the model

### 5.1.1. Actual load case

The best way to simulate the structural response of a blade to a hydrodynamic loading is by using fluid-structure interaction (FSI) analysis. An analysis like that was made in the past by Maljaars, providing a model that can be used in a FEM program to verify the structural integrity of the blade [1]. An accurate representation of the blade, in terms of the allocation of differently oriented laminas at various locations and the correct boundary conditions, is necessary. Maljaars' model was later used by Zhang [2], who changed the material properties from GFRP to CFRP and conducted an analysis using the same hydrodynamic loads as Maljaars did. Similarly, the same blade is used in this thesis, with the same mesh size, as it was noted that this led to the convergence of the method. Similar to Zhang, the same hydrodynamic loading was used, but a few changes were made to the material properties and to the allocation of the laminas to more accurately replicate the real blade.

The original idea was to manufacture a blade according to the guidelines of Jules Dock, as described in the thesis of W.H. de Bles [48]. The image showing the original plan can be found in Appendix B. However, there were discrepancies between the actual final blade and the one that was planned, necessitating a new allocation of the materials in this thesis to better represent reality. The new allocation of the laminas can also be found in the table in Appendix B. The FEM analysis was conducted at Marc/Mentat.

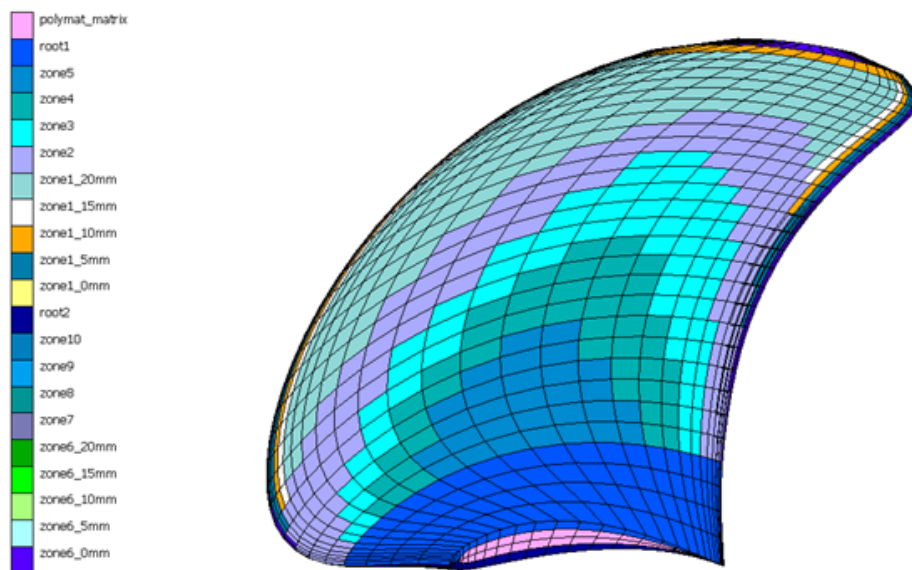


**Figure 5.1:** Suction side of the blade



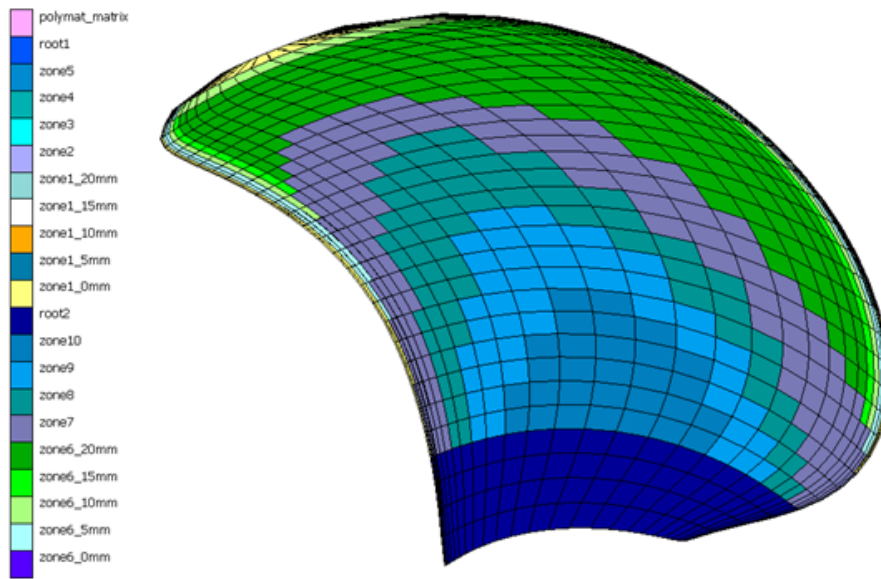


**Figure 5.2:** Pressure side of the blade

Maljaars and Zhang tested their blades in 60 different load cases, corresponding to a full revolution of the blade split into 60 time-steps for a specific scenario. Specifically, a vessel sails in a straight path in calm water at a speed of 5.35 m/s (10.4 knots), with the propeller operating at a constant rotational speed of 600 rpm, experiencing a non-uniform wake field. For each time step, the velocity potential was converted to pressure using Bernoulli's equation, and then the pressure was converted into nodal forces acting at the centroids of blade face elements. The maximum force is obtained when the blade is in the wake peak, leading to the following force components:

$$\Sigma F = \begin{cases} F_x = +8816 \text{ N} \\ F_y = +3565 \text{ N} \\ F_z = +318 \text{ N} \end{cases}$$

The total force is the absolute value of these three components and is given by:

$$\Sigma F = \sqrt{F_x^2 + F_y^2 + F_z^2} \quad (5.1)$$

which is equal to 9.5 kN.

The hub where the root is connected was assumed to be much stiffer than the blade, so a clamped boundary condition was used at the blade (root) – hub interface. Although the choice of a clamped boundary condition is not the most representative and likely leads to overestimated stress values at the critical location, potential improvements can be investigated in the future. Zhang found that the critical load case was the 59<sup>th</sup> time step, with the critical elements (hot-spots) being numbers 1363 and 1421 on the leading edge (figure 5.3). Consequently, this time-step was also used in this analysis to identify the hot-spot for the GFRP blade with the "corrected" material properties.

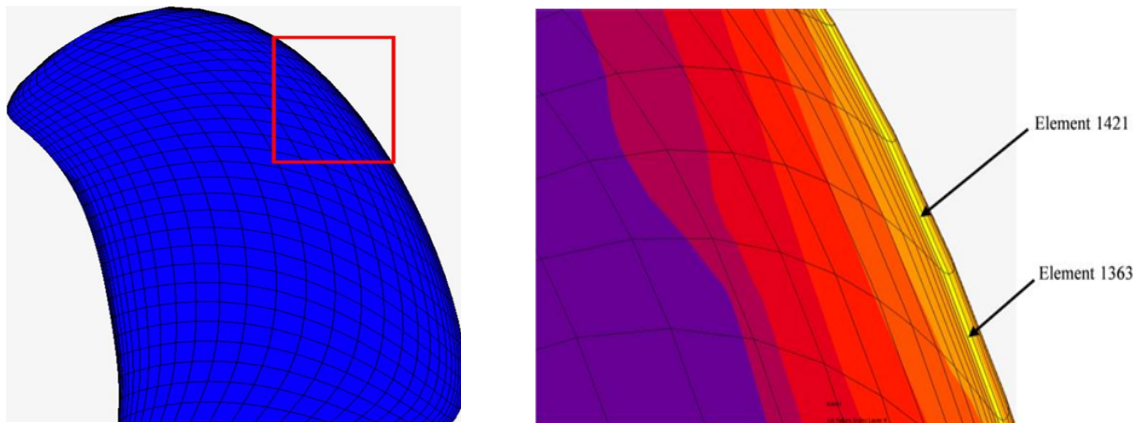


Figure 5.3: Position of critical elements, both images were taken from the work of Zhang [2]

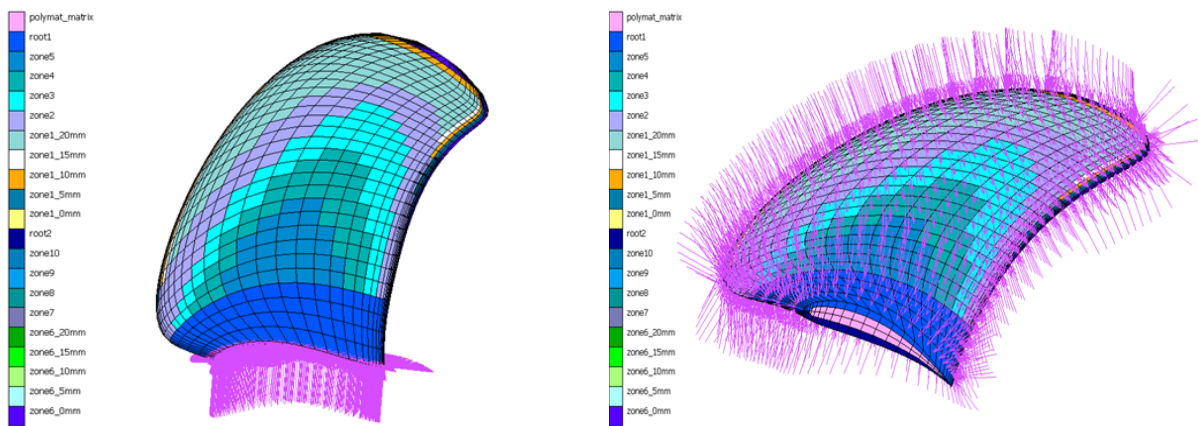


Figure 5.4: Clamped boundary condition and actual distributed pressure

Two different types of elements were used for the analysis of the blade. The brick element 21 of Marc Mentat was used for the core, which is a 20-node, isoparametric, arbitrary hexahedral element with three global degrees of freedom:  $u$ ,  $v$ , and  $w$ . Element type 150 of Marc was used for the skin of the blade; this is a composite brick element used for three-dimensional analysis of composite materials. Like element 21, it is also a 20-node element with the same global degrees of freedom. It consists of different layers within the element that represent the various laminas. More information about these elements can be found in the Marc Mentat documentation, Volume B.

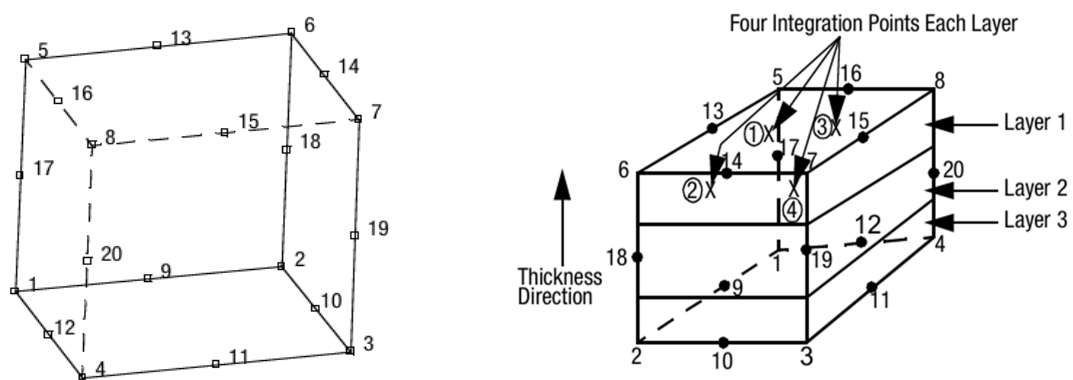
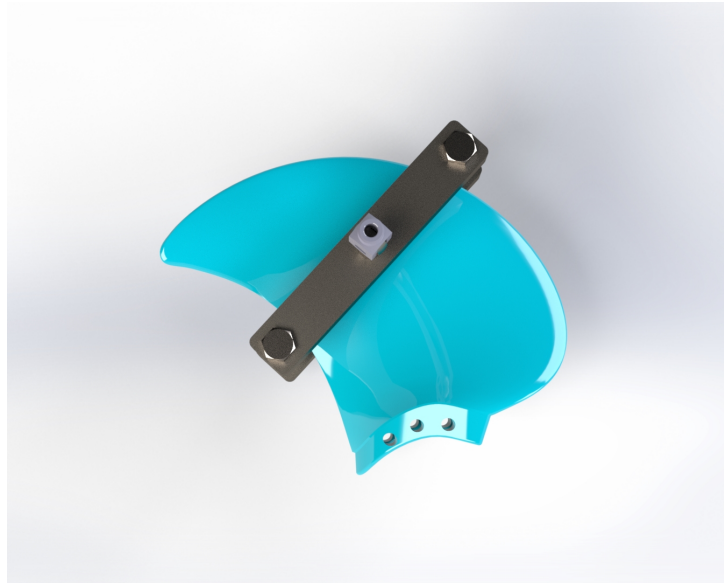


Figure 5.5: Solid brick element and Composite brick element - Marc Mentat [49]

### 5.1.2. Experiment

A fatigue experiment is planned as part of the EcoProp project to simulate the actual load case described previously. A similar fatigue test was conducted in the past by Maljaars on a different blade, and now Benjamin Groenhart is responsible for the new experiment on the examined GFRP blade. The new brace designed by Groenhart is displayed in the following image, and its finite element model was created in Marc/Mentat.



**Figure 5.6:** Design of new brace. The image is used after the permission of the designer.

Essentially, the same blade as before was used, with only the load case changed from distributed pressure to a surface load to replicate the force induced by this new brace. The total force was split into nodal forces on the pressure side and applied in a way to replicate the experiment, as shown below.

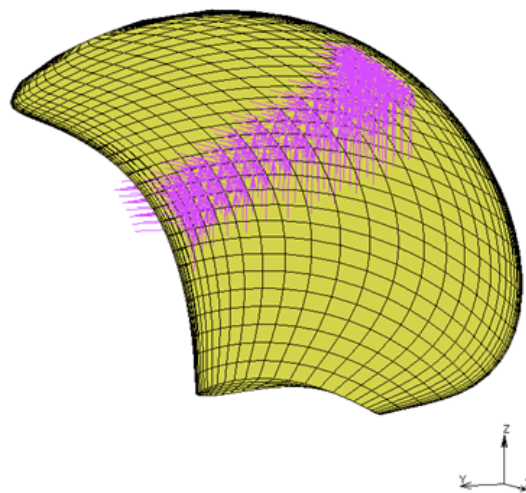


**Figure 5.7:** FEA model: Experiment

The purpose of this analysis was first to verify that the blade can carry the maximum load of 9.5 kN and second to determine the critical load that should be applied during the experiment to control the cycle at which failure occurs, based on the ply-by-ply analysis that will be presented in the next chapter. The load ratio of the experiment is  $R = 0.65$  and the frequency at which the experiment will be conducted is 5 Hz.

## 5.2. Results

To calculate where the hot spot is, Tsai – Wu failure criterion was used in three dimensions. The Tsai – Wu failure index in 3D is defined as:

$$F.I. = f_1\sigma_1 + f_2\sigma_2 + f_3\sigma_3 + f_{11}\sigma_1^2 + f_{22}\sigma_2^2 + f_{33}\sigma_3^2 + f_{44}\tau_{12}^2 + f_{55}\tau_{23}^2 + f_{66}\tau_{31}^2 + 2f_{12}\sigma_1\sigma_2 + 2f_{23}\sigma_2\sigma_3 + 2f_{31}\sigma_3\sigma_1 \quad (5.2)$$

where  $\sigma$  corresponds to the normal stresses and  $\tau$  to the shear stresses. The different terms  $f_{ij}$  can be determined using the following equations:

$$f_1 = \frac{1}{\sigma_1^T} - \frac{1}{\sigma_1^C} \quad (5.3)$$

$$f_2 = \frac{1}{\sigma_2^T} - \frac{1}{\sigma_2^C} \quad (5.4)$$

$$f_3 = \frac{1}{\sigma_3^T} - \frac{1}{\sigma_3^C} \quad (5.5)$$

$$f_{11} = \frac{1}{\sigma_1^T \sigma_1^C} \quad (5.6)$$

$$f_{22} = \frac{1}{\sigma_2^T \sigma_2^C} \quad (5.7)$$

$$f_{33} = \frac{1}{\sigma_3^T \sigma_3^C} \quad (5.8)$$

$$f_{44} = \frac{1}{\tau_{12}^2} \quad (5.9)$$

$$f_{55} = \frac{1}{\tau_{23}^2} \quad (5.10)$$

$$f_{66} = \frac{1}{\tau_{31}^2} \quad (5.11)$$

$$f_{12} = -\frac{1}{2}\sqrt{f_{11}f_{22}} \quad (5.12)$$

$$f_{23} = -\frac{1}{2}\sqrt{f_{22}f_{33}} \quad (5.13)$$

$$f_{31} = -\frac{1}{2}\sqrt{f_{33}f_{11}} \quad (5.14)$$

with the symbols T and C denoting the tensile and compressive strengths, respectively, and S the shear strength. Their values were taken from the literature (section 6.2) but they are not the most accurate due to the different ways of fabrication of the tested specimens and the different volume fraction of fibers that were used in the different works. It is noteworthy to mention how the new user coordinate system is defined based on the subroutine used by Maljaars to ensure the correct alignment of fibers in the blade, as described in the Literature Review chapter (see figure 2.2). Before conducting the analysis and using the subroutine, the global coordinate system is defined as follows:

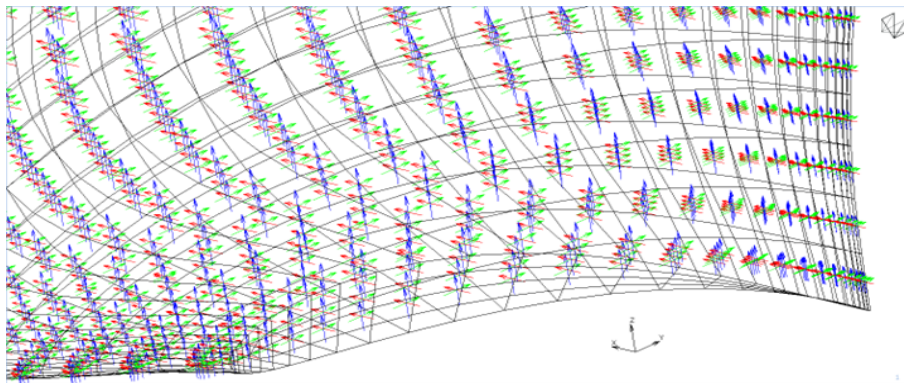


**Figure 5.8:** Coordinate system before applying the subroutine

with blue arrows corresponding to Z axis, red arrows to X axis and finally green arrows to Y axis. The origin of this global system XYZ is the black arrows with the force components presented before following this one (5.1.1). Marc constitutes a subroutine called orient2, which necessitates Z axis always being the through thickness direction of the elements and this was the first step that was followed to apply the user's defined coordinate system.

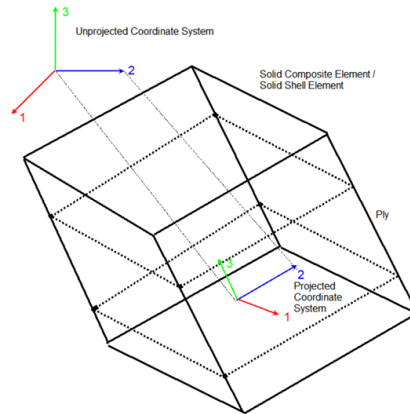


**Figure 5.9:** Orient2 subroutine, image taken from [50]

Therefore, after the application of Maljaars' subroutine, the new user – coordinate system becomes:

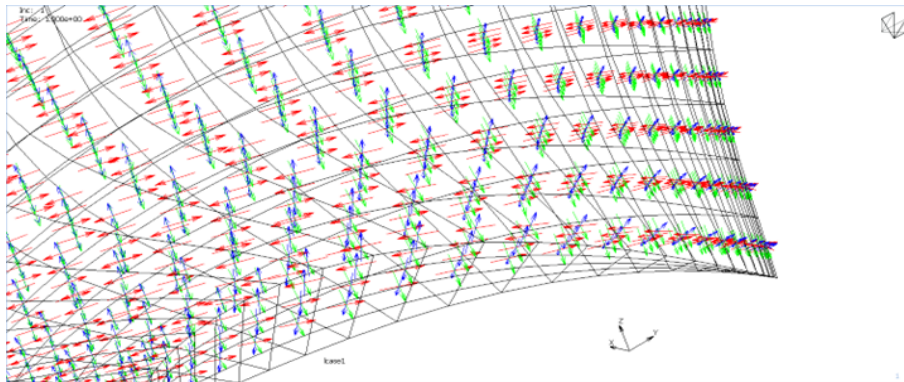


**Figure 5.10:** Coordinate system after applying the subroutine

where the Z axis (blue arrows) always runs through the thickness of the elements, the Y axis (green arrows) corresponds to the longitudinal axis of a 0-degree lamina, and the X axis (red arrows) corresponds to 90 degrees, similar to what is demonstrated in figure (5.11):

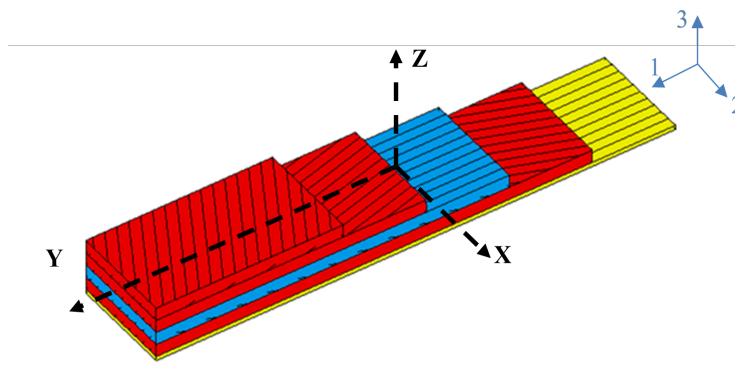
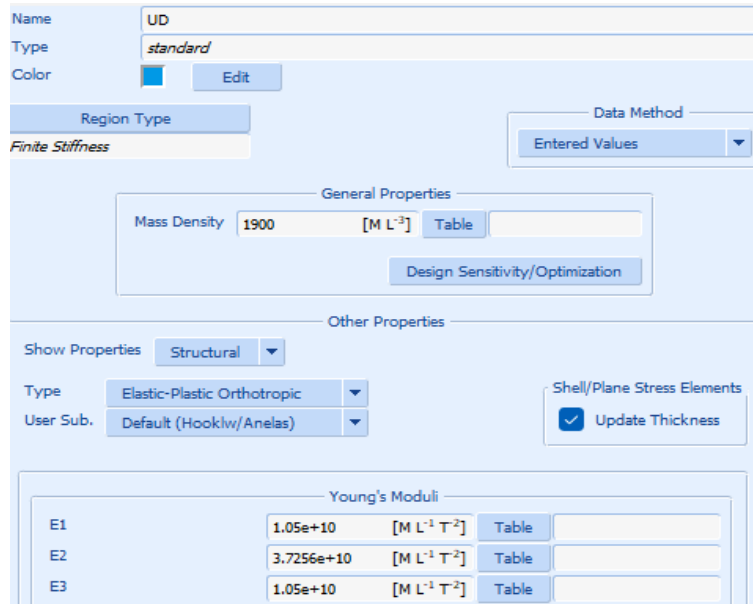


**Figure 5.11:** Relation of the user defined coordinate system (XYZ) and lamina's local system (123)

This transformation of the coordinate system requires the correct application of material properties. Specifically, material properties are imported into the local system of the lamina in Marc. To be compatible with the new coordinate system, the longitudinal axis corresponds to local direction 2 of the lamina, while the transverse direction corresponds to local orientation 1. For instance, the inputs for Young's modulus for a UD lamina are:



The screenshot shows the Marc software interface for defining material properties. The 'Name' is 'UD' and the 'Type' is 'standard'. The 'Region Type' is 'Finite Stiffness' and the 'Data Method' is 'Entered Values'. Under 'General Properties', the 'Mass Density' is set to 1900 [M L<sup>-3</sup>]. Under 'Other Properties', the 'Type' is 'Elastic-Plastic Orthotropic' and the 'User Sub.' is 'Default (Hooklv/Anelas)'. The 'Shell/Plane Stress Elements' section has 'Update Thickness' checked. The 'Young's Moduli' section is expanded, showing the following values:

Property	Value	Unit
E1	1.05e+10	[M L <sup>-1</sup> T <sup>-2</sup> ]
E2	3.7256e+10	[M L <sup>-1</sup> T <sup>-2</sup> ]
E3	1.05e+10	[M L <sup>-1</sup> T <sup>-2</sup> ]

Figure 5.12: Inputs in FEA - Marc

and similar process is followed for the shear modulus and strengths. Having explained these things, the results of the maximum failure index for the actual loading on the blade and the loading of 9.5 kN induced by the brace are demonstrated below:

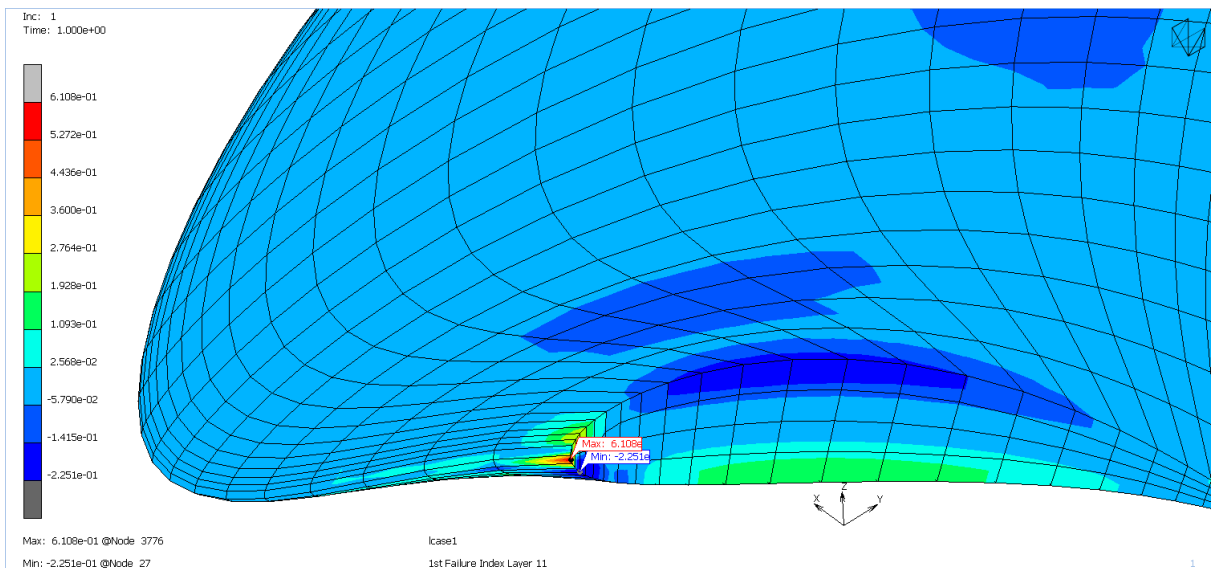
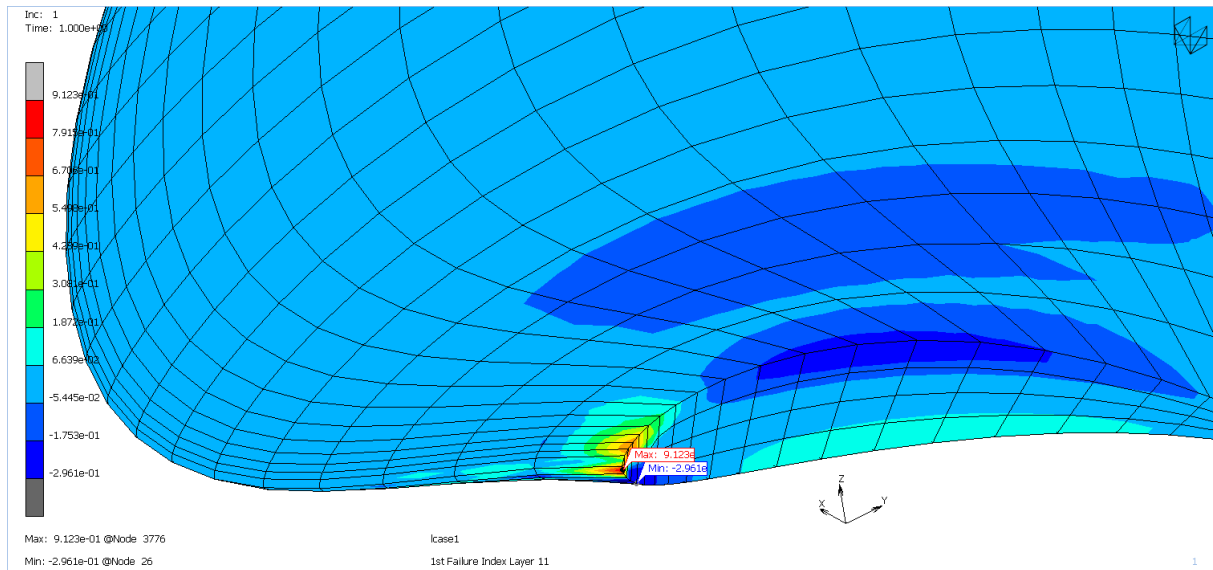
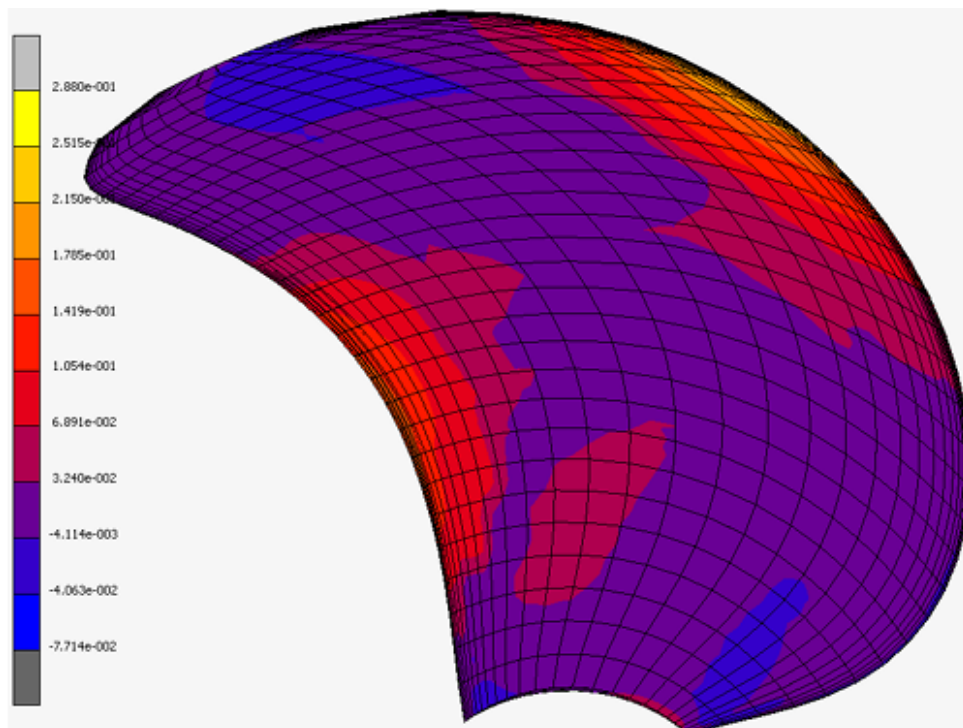


Figure 5.13: Numerical results of the actual loading - critical layer 11



**Figure 5.14:** Numerical results of the experiment - critical layer 11

In both cases, the hot-spot is found in element 29 at layer 11, near the clamp. This was expected because, firstly, the highest stresses are usually found closer to the boundary conditions, and secondly, layer 11 is a lamina oriented at 105 degrees that is loaded at 0 degrees. However, these results differ from what Zhang found in his analysis, as displayed in the next figure.



**Figure 5.15:** Results of Zhang, [2]

The differences between the two analyses have to do with the different type of material and also with the different allocation of the laminas in the blade.

# Predictions for a GFRP blade

## 6.1. Description of Methodology

One of the main goals of this research is to determine the extent to which the proposed methods for life cycle predictions and stiffness degradation can be applied to large-scale construction. The plan was to conduct a finite element analysis on the blade to identify where maximum stresses occur and to define the hotspot. Subsequently, it is necessary to export those values at the critical elements in their local coordinate system and combine them with Ramberg–Osgood terms, which can be derived from experimental data and are required for making predictions. This methodology is detailed in this chapter, starting with the definition of material properties, presenting the predictions for the blade’s lifespan and stiffness deterioration, and finally drawing conclusions.

The numerical method of finite element analysis is widely used, especially for complex geometries, to study their structural performance. This is due to the difficulty of deriving closed-form expressions from an analytical process that considers all parameters, such as changes in geometry at different locations and the presence of gaps, holes, or defects in the structure. In the case of the examined blade, the combination of its double-curved geometry and the fact that it is made of composite materials with laminas that were not placed to eliminate the coupling  $B_{ij}$  or flexural terms  $D_{ij}$  of the  $[ABD]$  matrix makes the use of FEM almost obligatory.

The blade is composed of laminates with different stacking sequences at various locations, leading to complex stress distribution fields. As observed in the chapter on Finite Element Analysis (5), the hot spot is near the root, close to the clamped boundary conditions. Therefore, the stress values at the critical elements were exported, and they were used to make predictions about the fatigue life of the blade. The critical node is 3776 in element 29, as can be seen in figures 5.13 and 5.14. Layer 11 is the critical lamina, which was expected based on prior discussions. The results of the post process analysis indicated that T-W failure index is 0.64 for the actual load case and 0.94 for the experiment (9.5 kN).

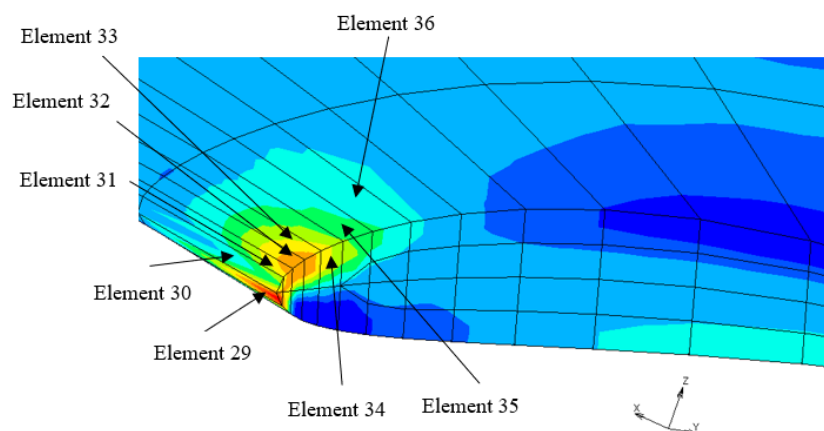


**Figure 6.1:** Critical elements from the FEM analysis



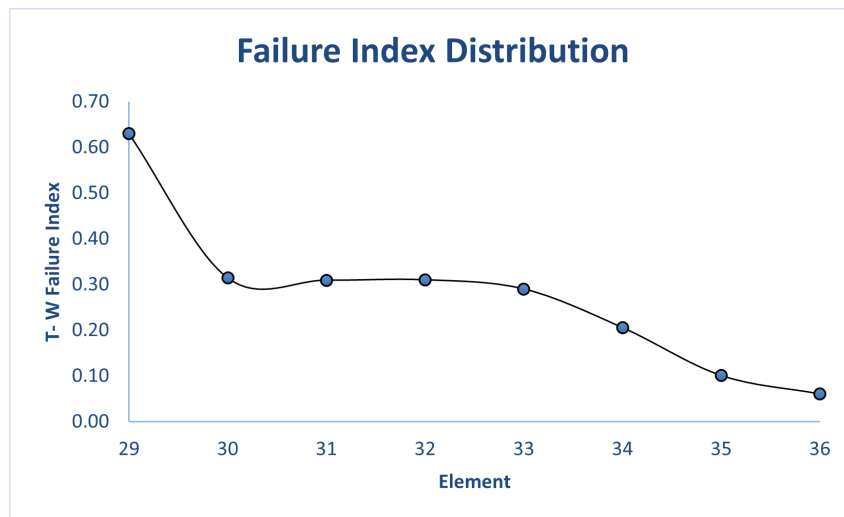


**Figure 6.2:** Estimated variation of failure index - Actual load case

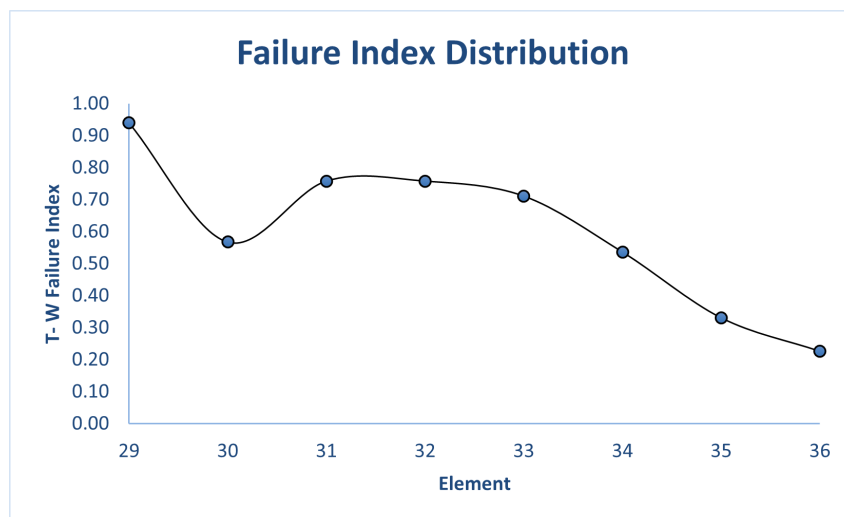


**Figure 6.3:** Estimated variation of failure index - Experiment

The exported stresses at every direction are summarized in the next table:

**Table 6.1:** Results of FEA in terms of stresses

Layer 11 (Element 29) - MPa	Actual load case	Experiment (9.5 kN)
$\sigma_{11}$	189.70	269.69
$\sigma_{22}$	38.26	58.84
$\sigma_{33}$	26.41	36.47
$\sigma_{23}$	-7.29	-8.39
$\sigma_{13}$	2.14	3.49
$\sigma_{12}$	13.05	21.17

The experiment is scaled up to accelerate the failure of the blade and the load is 5.82% higher than the actual load of the 59<sup>th</sup> load step. However, the stress distribution of the actual loading case is reproduced by the experiment.

## 6.2. Material Properties

A series of small-scale coupon experiments is planned over the next few months to determine the necessary parameters for predicting the fatigue life of the blade. Currently, a literature review has been conducted to find the mechanical properties for the FEA model and the required experimental curves to determine K and n values. Data for longitudinal and transverse directions were collected for tension, compression, and in-plane shear. The critical type of fabric is the unidirectional one because, as the lamina is oriented closer to 90 degrees while it is loaded at 0 degrees it becomes more matrix-dominated. This type of lamina is the most critical based on FEA results. The tensile strength of 0-degree coupons and their corresponding Ramberg-Osgood law terms were found based on the work of Shokrieh et al. [51]. The aim of this study was to investigate the effect of quasi-static and dynamic strain rates on unidirectional glass/epoxy laminates with a fiber volume fraction of 0.5. Data from five samples were recorded in this study, with the following figure used to determine K and n values for the strain rate of  $\dot{\epsilon} = 0.0017 \text{ s}^{-1}$ .

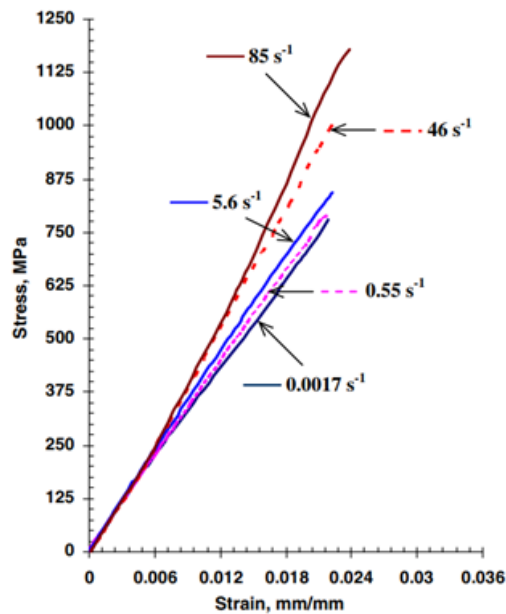


Figure 6.4: Longitudinal tension of GFRP, [51]

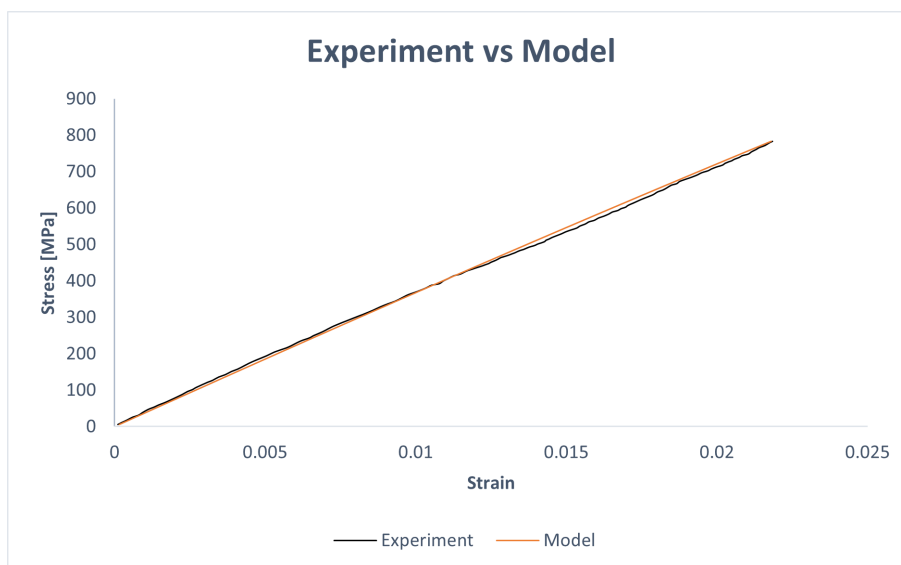


Figure 6.5: Model vs experimental curve, longitudinal tension

The average results of this study for tensile strength, elastic modulus, strain to failure, and absorbed energy are given in the next table:

**Table 6.2:** Longitudinal tensile properties of GFRP, [51]

Properties	Average value	Standard deviation
<b>Tensile strength [MPa]</b>	783.24	2.21
<b>Elastic modulus [GPa]</b>	37.256	0.16
<b>Strain to failure</b>	0.02148	1.5e-04
<b>Absorbed energy MJ/m<sup>3</sup></b>	8.52	0.24

The tensile strength, Young 's modulus and stress – strain curve for the transverse direction were obtained from the work of Zhang et al. [52], where the influence of fiber orientation to the material properties of pultruded GFRP fibers was investigated. Coupons with a fiber volume fraction of 0.42 were tested with the following data provided as the recorded ones:

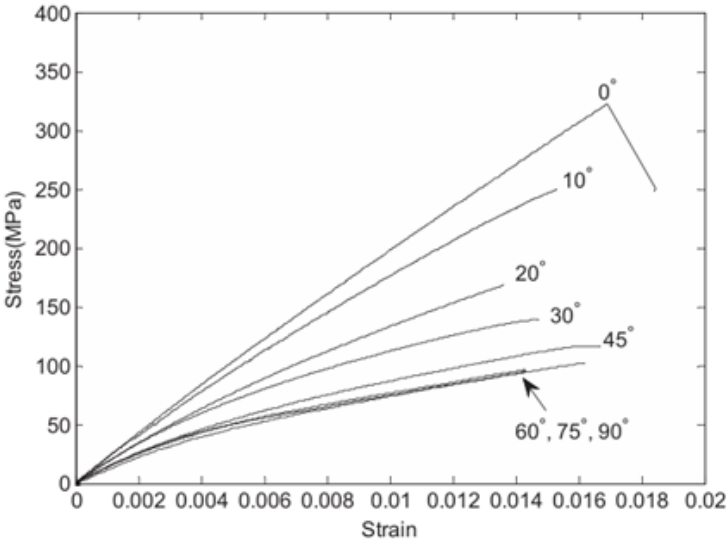


**Figure 6.6:** Transverse tension of GFRP, [52]

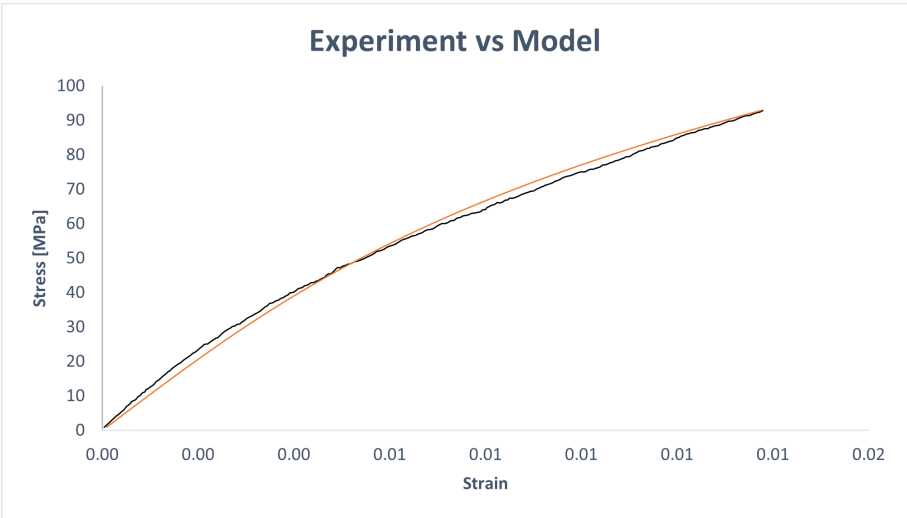


**Figure 6.7:** Model vs experimental curve, transverse tension

The average values of tensile strength  $Y_T$  and  $E_2$  are given in the following table with the standard deviations.

**Table 6.3:** Tensile properties in transverse direction of GFRP, [52]

Properties	Average value	Standard deviation
Tensile strength [MPa]	92.8	2.69
Elastic modulus [GPa]	10.5	0.303

Similar to the tensile mechanical properties, the stiffness and strengths for longitudinal and transverse compressive cases were found in the literature. For the longitudinal compressive strength, the work of Lee et al. [53] was used, where the following curves are provided. The case with a fiber volume fraction of 0.40 was selected from the graphs shown.

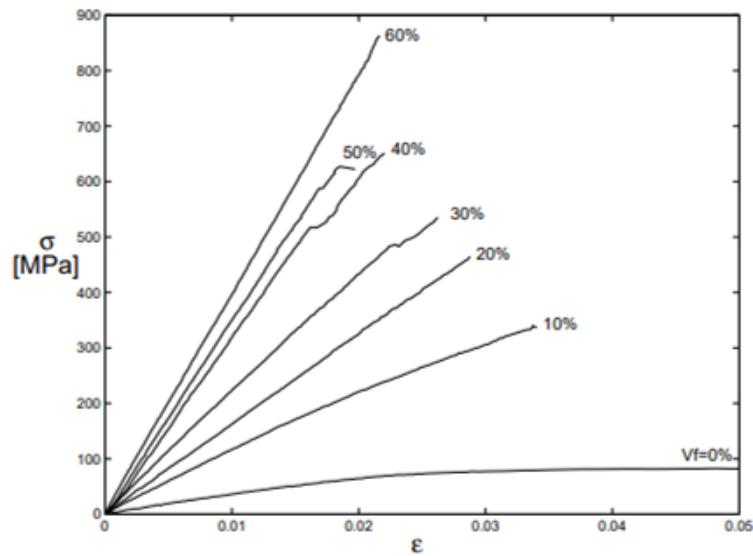


**Figure 6.8:** Longitudinal compression of GFRP, [53]

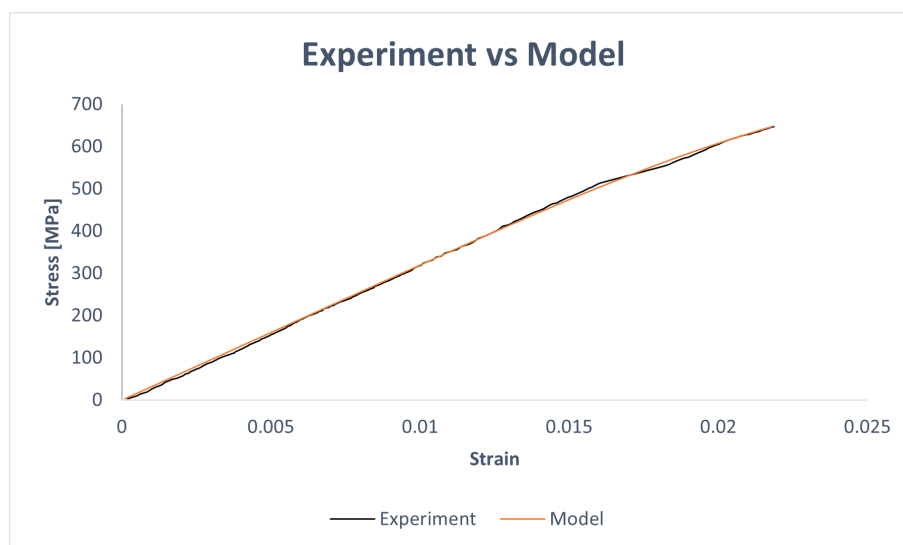


**Figure 6.9:** Model vs experimental curve, longitudinal compression

The initial stiffness and the compressive strength are:

**Table 6.4:** Longitudinal compression properties of GFRP, [53]

Properties	Average value
Compressive strength [MPa]	647.28
Elastic modulus [GPa]	32

Similarly, the necessary data for transverse compressive mechanical properties were found in the work of Kaddour et al. [54], which provides mechanical properties for four unidirectional laminates made of different materials. These properties are presented not only through curves but also with discrete stress-strain data. This specific paper was also used to select other properties required for FEA, such as Poisson's ratios, as three-dimensional elastic properties are provided in this publication for numerical analyses.

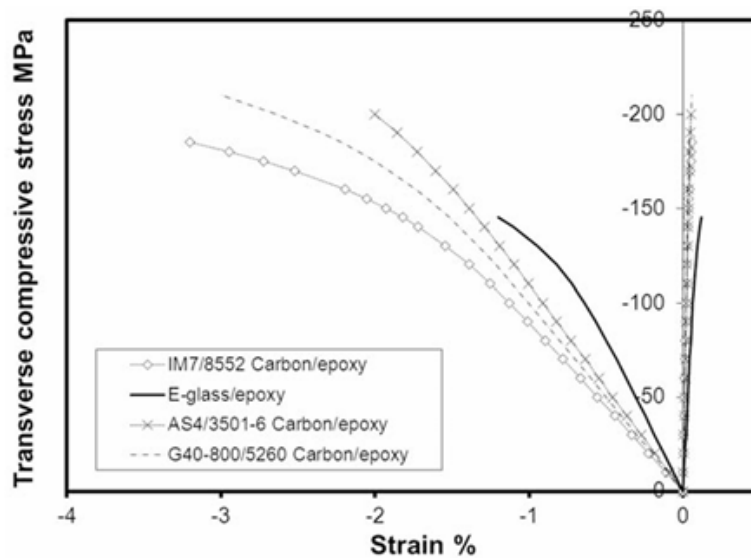


**Figure 6.10:** Transverse compression of GFRP, [54]

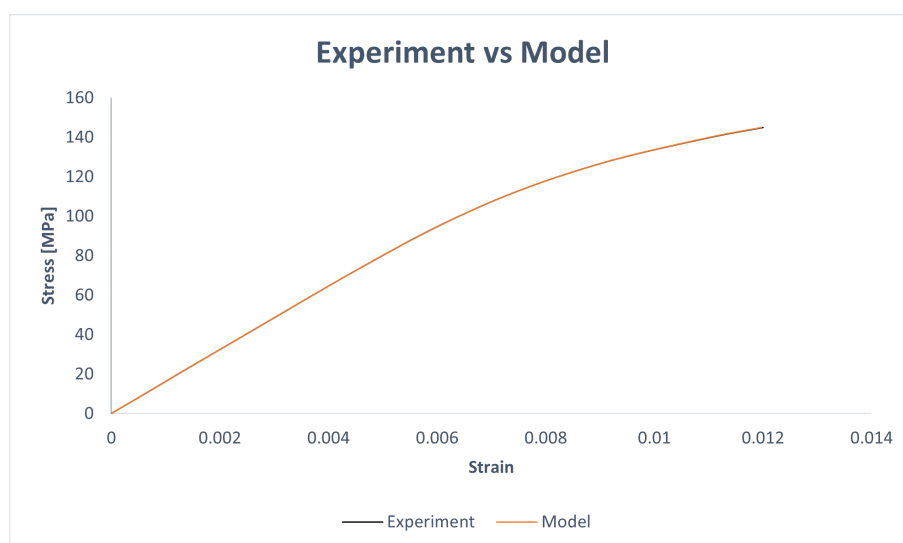


**Figure 6.11:** Model vs experimental curve, transverse compression

with Young's modulus and strength being given in the following table:

**Table 6.5:** Compression properties in transverse direction of GFRP, [54]

Properties	Average value
Compressive strength [MPa]	145
Elastic modulus [GPa]	16.2

Finally, the in-plane shear properties were taken from the paper by Van Paepegem et al. [55]. The authors conducted static tests on the  $[+45^\circ / -45^\circ]_{2s}$  specimens of GFRP laminates to measure the in-plane shear properties. Subsequently, they developed a material model to represent the shear modulus degradation and the accumulation of permanent shear strain [56]. The material used was a UD E-glass fabric (Roviglass R17/475) with an epoxy matrix, Araldite LY 556. The properties of the lamina were calculated based on a fiber volume fraction of 50%.

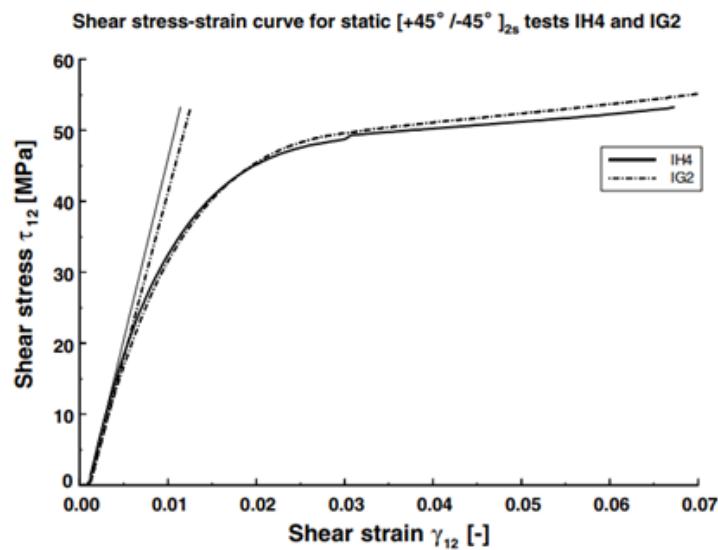


**Figure 6.12:** Shear properties of GFRP, [55]

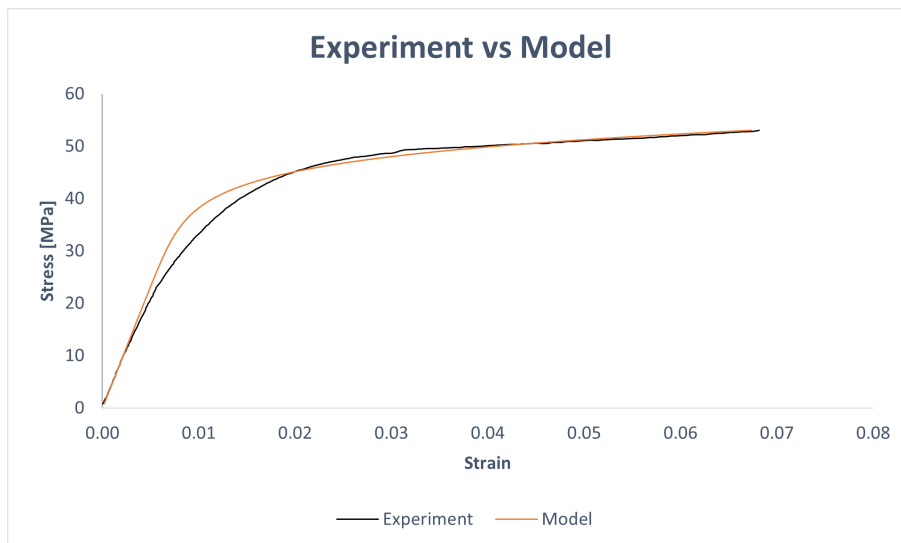


**Figure 6.13:** Model vs experimental curve, shear

The required shear properties are displayed in the next table:

**Table 6.6:** Shear properties of GFRP, [55]

Properties	IH4	IG2
<b>Compressive strength [MPa]</b>	69.2	71
<b>Elastic modulus [GPa]</b>	5.09	4.66

Data from type IG2 were used to make predictions for the blade in this thesis.

## 6.3. Predictions

With all the stress-strain curves presented earlier, the lifespan prediction methodology can be used to determine the K and n values, and consequently estimate the blade's life based on its in-plane stresses,  $\sigma_1$ ,  $\sigma_2$ , and  $\tau_{12}$ . The Ramberg-Osgood values for all cases are provided in the table below:

**Table 6.7:** Ramberg-Osgood terms determined for the lifespan predictions

Type of test	Value of K	Exponent n
<b>Longitudinal tension</b>	7.34	2.3687
<b>Transverse tension</b>	2.78e+04	3.2884
<b>Longitudinal compression</b>	1.94e+09	7.138
<b>Transverse compression</b>	4.77e+11	6.9323
<b>In-plane shear</b>	1.39e+19	10.4917

To calculate the blade's life, two different criteria were used. The first criterion involves determining which combination of stresses and its corresponding stress-strain curve leads to the minimum number of cycles. The second criterion is the Tsai-Wu failure criterion, applied using two different approaches.

### 6.3.1. Actual load case of blade

#### First criterion

Starting with the first criterion, the stresses exported from FEA at the critical hot spot were presented in Table 6.1. Using the Ramberg - Osgood terms that were determined based on the experimental data (6.7), the following cycles were calculated using  $\sigma_1 = 189.7MPa$ ,  $\sigma_2 = 38.26MPa$ , and  $\tau_{12} = 13.05MPa$  to the fatigue lifespan model.

$$N_{fX_T} = 589356536$$

$$N_{fY_T} = 3488703$$

$$N_{fS_{12}} = 3.072e + 18$$

The critical prediction results from the transverse tension at 3.48 million cycles, indicating at least the first damage of the blade. The type of failure and the redistribution of stresses affect the fatigue life of the blade.

#### Second criterion

##### Version 1

The second criterion is a generalization of the Tsai-Wu criterion, considering strengths as a function of cycles. This methodology is inspired by the work of Philippidis et al. [57], who used a quadratic failure tensor polynomial, yielding results in good agreement with experimental data. The two different approaches are related to how strength decreases cycle by cycle.

In the first version, the lifespan model presented earlier was used for various stress levels to create a fatigue stress life cycle curve. Afterwards, a fitting curve for each strength was then applied, and longitudinal, transverse, and shear strengths were expressed as functions of cycles. The fitting curves and their relationships are displayed below:



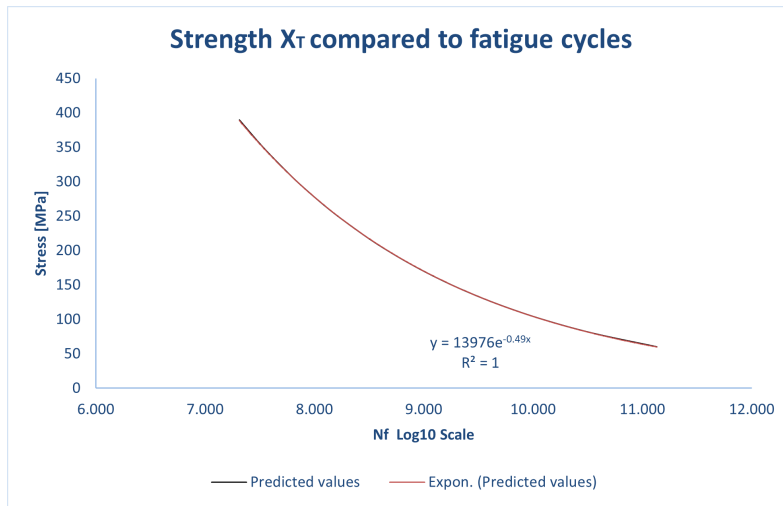


**Figure 6.14:** Strength as a function of cycles - longitudinal tension

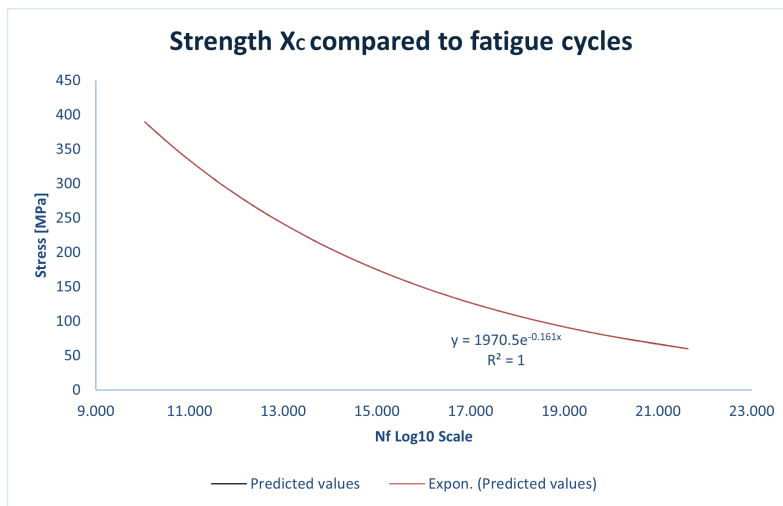


**Figure 6.15:** Strength as a function of cycles - longitudinal compression

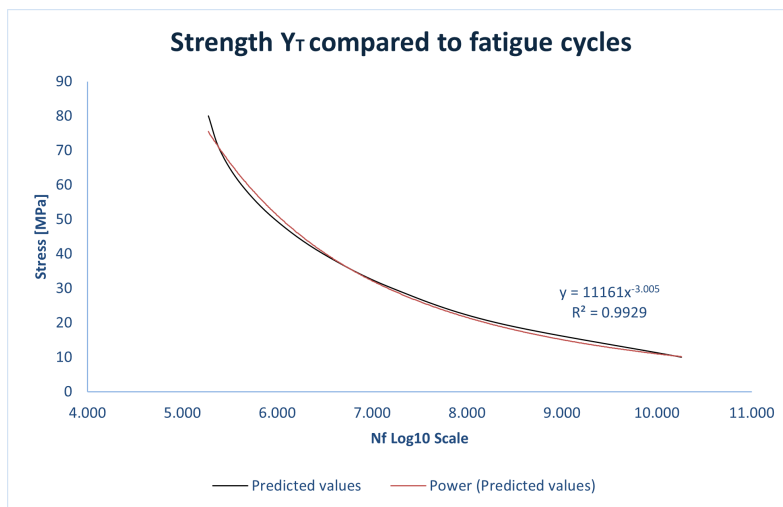


**Figure 6.16:** Strength as a function of cycles - transverse tension

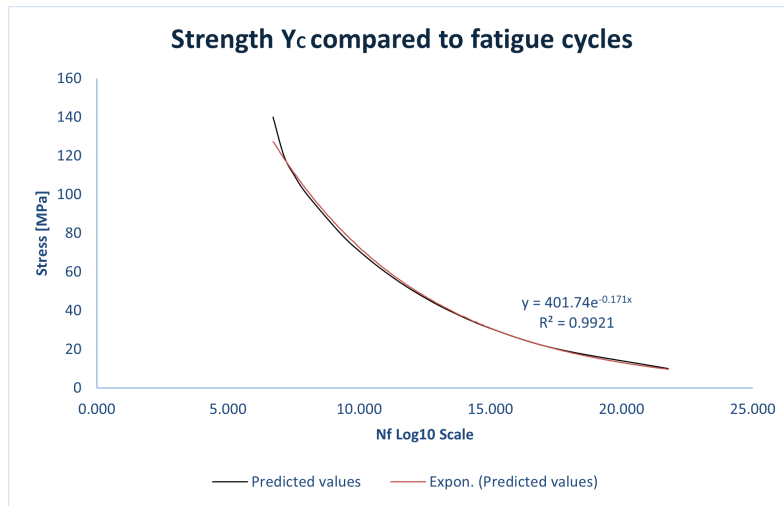


Figure 6.17: Strength as a function of cycles - transverse compression

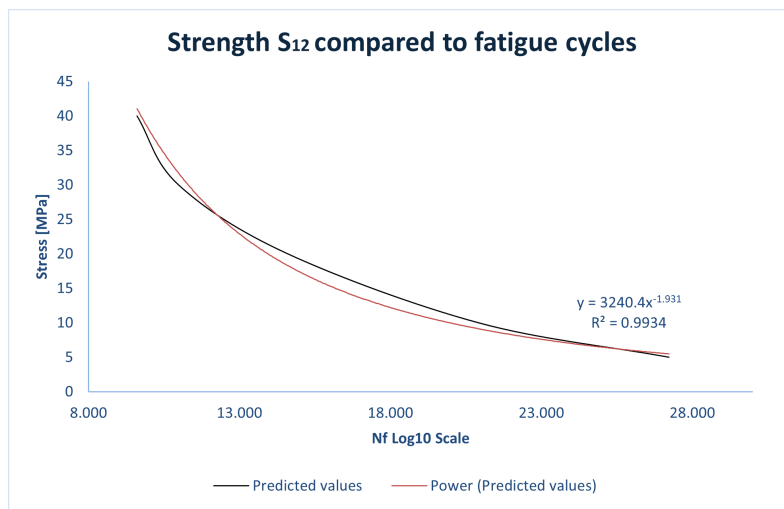


Figure 6.18: Strength as a function of cycles - In plane shear

Subsequently, fatigue life can be determined using the Tsai-Wu (fatigue) failure criterion when the following relation is satisfied:

$$F.I. = f_1\sigma_1 + f_2\sigma_2 + f_{11}\sigma_1^2 + f_{22}\sigma_2^2 + f_{44}\tau_{12}^2 + 2f_{12}\sigma_1\sigma_2 \leq 1 \quad (6.1)$$

where  $f_i$  and  $f_{ij}$  terms can be found in equations 5.3 to 5.14. The resultant fatigue life of the blade under the actual load case is:

$$N_f = 3572728 \text{ cycles}$$

#### Version 2

The second version consists of a different approach to how strengths change throughout the fatigue life. As presented in the chapter on stiffness degradation, it was assumed that strength changes linearly based on the following formula:

$$\sigma_{J_f}(m) = \sigma_{J_f} - \frac{m}{N_{f_J} - 1} \sigma_{J_f} \quad (6.2)$$

where  $J$  corresponds to  $X_T, X_C, Y_T, Y_C$ , and  $S_{12}$ , and  $m$  denotes the cycle that is running until it reaches the final lifespan  $N_f$ , predicted by the first criterion. The resultant fatigue life using this approach is:

$$N_f = 2088800 \text{ cycles}$$

and it is the most conservative one.

### 6.3.2. Load case during experiment

Following the same process for the load case of 9.5 kN for the upcoming experiment, the results for the two criteria with the two versions of Tsai-Wu are demonstrated below. Stresses at the hot spot were determined to be  $\sigma_1 = 269.69$  MPa,  $\sigma_2 = 58.84$  MPa, and  $\tau_{12} = 21.17$  MPa.

#### First criterion

$$N_{f(X_T)} = 113302775 \text{ cycles}$$

$$N_{f(Y_T)} = 452063 \text{ cycles}$$

$$N_{f(S_{12})} = 1.206 \times 10^{14} \text{ cycles}$$

#### Second criterion

##### Version 1

$$N_f = 687068 \text{ cycles}$$

##### Version 2

$$N_f = 167900 \text{ cycles}$$

which means that the blade is expected to show its first significant damage during the upcoming experiment between 167900 cycles and 687068 cycles, based on the experimental data on strength found in the literature.

An interesting observation is that all three approaches presented results of the same order, with only minor variance, which can be considered desirable for capturing the expected fatigue life scatter. The most conservative predictions are made using the third approach, where strength is assumed to change linearly. The second most conservative is when the highest in-plane stress is used in the lifespan model. Finally, the least conservative is the Tsai-Wu criterion, which utilizes the fatigue stress-life curves produced by the lifespan model.

Another significant observation is that all predictions closely align with the lifespan predicted by stress applied in the transverse direction (90 degrees), particularly when the stress is tensile. This indicates that tensile stresses promote the formation of defects due to localized stress concentrations. Additionally, when the load is applied along the longitudinal axis of a specimen with fibers oriented at 90 degrees, the material becomes matrix-dominated. Similarly, this suggests that the out-of-plane properties, which are more influenced by the matrix, are potentially important parameters that should be examined.

## 6.4. Conclusions

The most critical parameter that influences the fatigue life of the blade under in-plane loading stresses has been proven to be the tensile stress in the transverse direction  $\sigma_2$ . This is the main reason that, although there were T-W failure indices greater than the one found in layer 11, this lamina was the most critical one as  $\sigma_2$  reached its highest value close to 59 MPa.

To further validate this conclusion, the maximum stress failure criterion was also used in Marc to compare the results with those of the Tsai-Wu failure criterion. The results can be seen in the next figures. As observed, the position of the hot spot does not change, and layer 11 displayed the maximum failure index for both transverse and longitudinal directions.

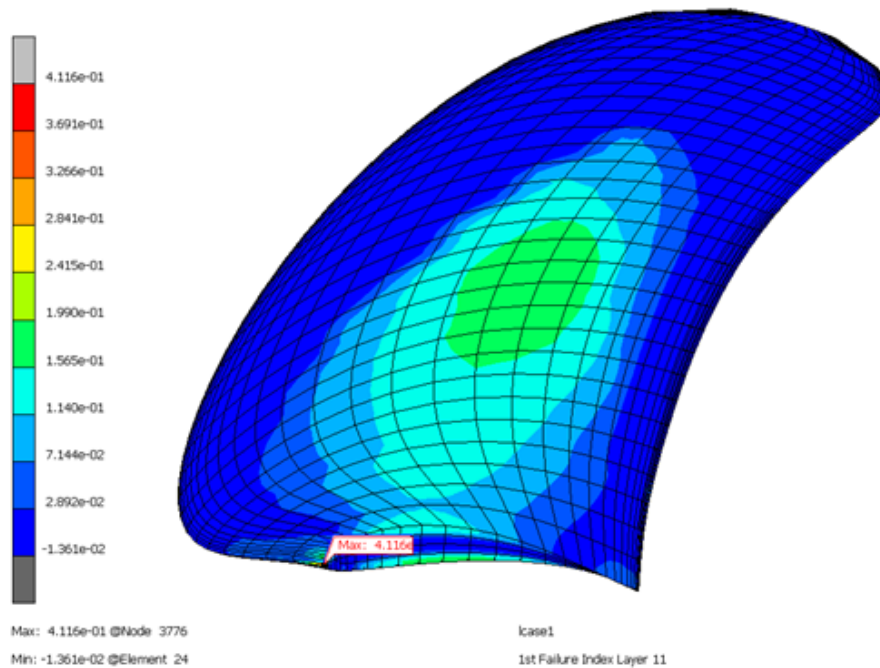


**Figure 6.19:** Maximum stress criterion - 1<sup>st</sup> failure index - transverse direction

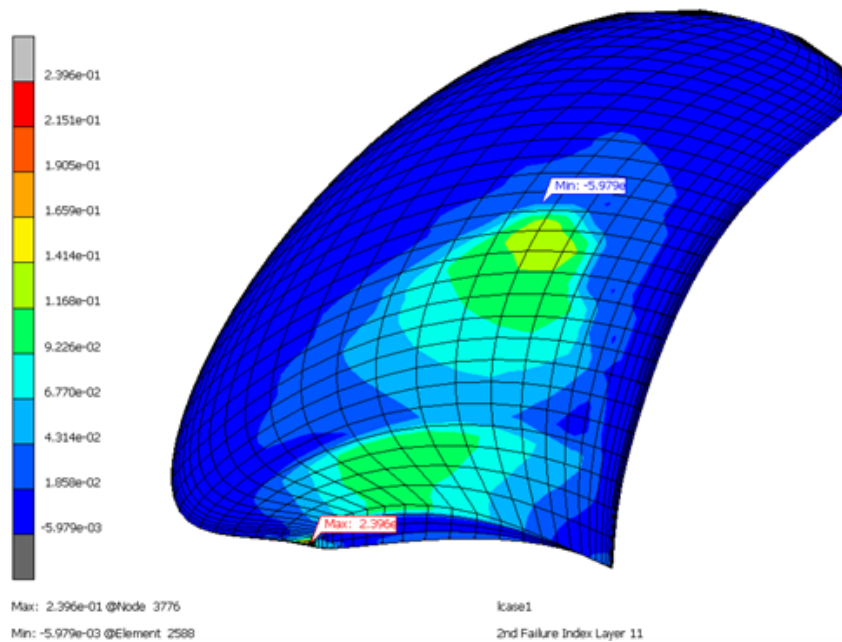


**Figure 6.20:** Maximum stress criterion - 2<sup>nd</sup> failure index - longitudinal direction

It is important to mention that the through-thickness stresses  $\sigma_{33}$ ,  $\sigma_{13}$ , and  $\sigma_{23}$  could be the most significant in terms of the blade's fatigue life. However, to validate this, experimental data on static stress-strain curves is required for these directions.

Finally, the predictions regarding the lifespan of the blade will likely change when the planned small-scale coupons experiment is conducted. As new stress-strain curves become available, they will provide discrete stress-strain data, leading to improved determination of the Ramberg-Osgood terms or applying equation 3.11 or 3.12 depending on the load ratio  $R$  and subsequently to more accurate results. As a result, with the aforementioned data, the stiffness degradation model can be used to find the deterioration of the stiffness, which is critical for the structure in terms of both its integrity and its hydrodynamic performance. Especially regarding hydrodynamic behavior, this is a highly significant advantage as hydrodynamic engineers will know which stiffness should be used for their design to make the blade either stiffer or more flexible to increase efficiency.



**Figure 6.21:** Actual blade: fabrication of the hub-blade interface

## Conclusions

The objective of this research was to assess the fatigue of structures made of composite materials using the innovative analytical method proposed by Kassapoglou. Originally developed for metals and demonstrating good agreement with experimental results, this method was adapted for composites in this thesis. Additionally, a new stiffness degradation model was created based on the fundamentals of this theory, showing good agreement with experimental results, though further investigation is needed. Validity research for both the lifespan prediction and stiffness degradation models was conducted using data from the literature.

An update to a Finite Element Analysis (FEA) model was also made, building on previous work regarding a GFRP blade for the EcoProp project, where fiber alignment was corrected and root regions were added. Finally, a combination of the FEM model and lifespan prediction model was implemented by analyzing the blade in three dimensions and extracting critical stresses at hot spots. Subsequently, in-plane stresses were used, and three different approaches were followed to predict the fatigue life of the blade. Upcoming experiments will verify whether these predictions are accurate.

Beginning with the fatigue life assessment using Kassapoglou's method, the same assumptions made for metals were applied to composite materials, comparing the predicted values with experimental data found in literature. In some cases, the experimental measurements of fatigue lives were captured acceptably, while in others, the results were either overestimated or underestimated. The critical parameter affecting the resultant curves is the initial stiffness, which is also influenced by the lack of discrete stress-strain values in the literature, necessitating digitization to replicate the curves. This digitization process varies between individuals, leading to different predictions. Additionally, this method assumes that dissipated energy converges after a few cycles but a further investigation of how this change occurs will assist in further improving the method especially for the first cycles that include  $n_1$ . As shown in the thesis, a new way of determining K and n values was presented using an optimization function instead of the 0.2% strain offset method.

An interesting observation was made in the work of Rafiqzaman et al. [43] regarding the case of  $R=0$ , where each stress-strain curve was replicated individually. The resultant curves captured the experimental measurements of fatigue life very accurately at specific stress levels. Moreover, in cases where the mean value of initial stiffness led to acceptable predictions, the 10th and 90th percentile curves bracketed the experimental data, especially for short and mid-term fatigue lives. This may be because, as described in some literature, the dissipated energy decreases during the initial cycles until it reaches a point where it increases again. However, with further investigation, there is a high potential for resolving these issues and improving the accuracy of the predictions. One of the greatest advantages of this method is that it relies on measurable quantities and does not depend to curve fitting. Additionally, it is a method which can reproduce known behavior such as the existence of fatigue threshold.

In addition to the fatigue life prediction model, a stiffness degradation model was also developed by Kassapoglou, based on the fundamental principles of the lifespan model. This new methodology allows for the estimation of both tangent and secant modulus degradation, with results for the two examined cases showing good to very good agreement with experimental results especially when stress strain data are given. The model is expected to improve further as the lifespan prediction model becomes more robust.

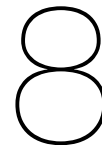
Regarding the FEM model, an update to the previous models by Maljaars and Zhang was created, revealing a different hotspot than the one proposed by the latter researcher. The new model provides a

---

more realistic representation of the actual blade, with the addition of the root region. A 3D stress analysis was conducted using the Tsai-Wu criterion and the maximum stress criterion, both identifying the same critical location near the clamp. This result was expected, as the clamped region is the boundary condition where internal forces become larger. Additionally, the critical layer was found to be the 11th one, with fibers oriented at 105 degrees while it is mainly loaded at 0 degrees.

Predictions were also made for the actual load case of the blade and the upcoming experiment, based on the lifespan prediction model. The in-plane stresses were extracted from Marc, and predictions were made using experimental data from static stress-strain curves found in the literature. Even though an effort was made to find properties for similar materials, there could be significant differences from the material to be used in this program because of (a) different fabrication method(s) (b) different final fiber volume(s) and (c) different matrix material. It was shown that the most critical component is the tensile strength in the transverse direction (90 degrees), which is most affected by the matrix. However, it is important to further investigate the influence of out-of-plane terms, such as stress in the through-thickness direction and inter-lamina and intra-lamina stresses. This necessitates small-scale coupon experiments in these directions.

Based on these conclusions, a set of recommendations for future work is provided in the next chapter 8.



## Recommendations for future work

The proposed recommendations are listed in descending order of priority, starting with the most urgent and ending with the less critical ones. The significance of the last recommendations is not diminished; they simply require more time and are more general in nature.

1. Small-scale coupon experiments are necessary. These tests are needed for several reasons. Firstly, they will provide stress-strain data that can be used to determine the K and n values for the materials used in the blade and not for load ratios close to zero, enabling more accurate predictions for its fatigue. The measured properties can also be applied to the FEM model, and the analysis should be updated accordingly. Measuring the stiffness degradation in some coupons will be helpful for comparison with the model's predictions, as stress-strain values will be known.
2. A fatigue experiment on the GFRP blade is highly important because it will provide data on the blade's fatigue life, helping to compare and optimize the lifespan prediction model. Strain gauges placed in various regions of the blade will help verify the FEM model's validity and determine if any adjustments are needed. Additionally, comparing the model's predicted fatigue life with experimental results will indicate whether the ply-by-ply analysis is accurate.
3. Further investigation and improvements on the methods are required. Acoustic emission sensors can be used to measure the dissipated energy in each cycle, allowing the recursion relationship of  $n_{(i-1)}/n_i$  to be updated and verified for applicability to composite materials. This will also determine if the relationship holds for the entire fatigue life or changes after a few cycles. These results can further enhance the stiffness degradation model.
4. Creating a progressive damage model in FEA is the next step. Once the method details have been refined and the lifespan model becomes robust for predicting fatigue life in composites, a progressive damage model can be developed. Specifically, functions indicating how strength changes through cycles can be integrated into an FEM model, providing a more realistic representation of the blade's structural response when combined with the stiffness degradation model.
5. Lastly, developing a digital twin of the blade by correlating data from strain gauges during experiments with an FEM model is crucial. This involves creating a link between the blade and the FEM model, where data from the strain gauges are fed into the numerical model to check its structural integrity continuously. Combining this process with lifespan and stiffness degradation models can predict the blade's response throughout its life, estimate remaining life, and determine when maintenance is necessary. If proven feasible, this process can be generalized to other constructions beyond propeller blades.

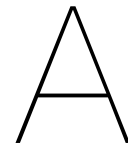


# References

- [1] Pieter Maljaars et al. "Hydro-elastic analysis of flexible marine propellers". In: *Maritime Technology and Engineering*; Guedes Soares, C., Santos, T., Eds (2014), pp. 705–715.
- [2] Xiaobo Zhang. "Short-term structural performance of self-monitoring composite marine propellers". In: *Delft University of Technology* (2021).
- [3] Thijs van Herwerden. "Fatigue life prediction of composite marine propellers". In: (2023).
- [4] Christos Kassapoglou. "Determination of energy dissipation during cyclic loading and its use to predict fatigue life of metal alloys". In: *Fatigue & Fracture of Engineering Materials & Structures* 46.10 (2023), pp. 3667–3679.
- [5] John Carlton. *Marine propellers and propulsion*. Butterworth-Heinemann, 2018.
- [6] Yin Lu Young et al. "Adaptive composite marine propulsors and turbines: progress and challenges". In: *Applied Mechanics Reviews* 68.6 (2016), p. 060803.
- [7] Amélie Boisseau et al. "Long term durability of composites in marine environment: Comparative study of fatigue behavior". In: *Procedia Engineering* 133 (2015), pp. 535–544.
- [8] MM Shokrieh et al. "A unified fatigue life model based on energy method". In: *Composite Structures* 75.1-4 (2006), pp. 444–450.
- [9] M Kawai. "A phenomenological model for off-axis fatigue behavior of unidirectional polymer matrix composites under different stress ratios". In: *Composites Part A: applied science and manufacturing* 35.7-8 (2004), pp. 955–963.
- [10] Mahmood M Shokrieh et al. "Progressive fatigue damage modeling of composite materials, Part I: Modeling". In: *Journal of composite materials* 34.13 (2000), pp. 1056–1080.
- [11] H □ Lin et al. "Strength evaluation of a composite marine propeller blade". In: *Journal of reinforced plastics and composites* 24.17 (2005), pp. 1791–1807.
- [12] Yin L Young. "Fluid–structure interaction analysis of flexible composite marine propellers". In: *Journal of fluids and structures* 24.6 (2008), pp. 799–818.
- [13] Jose Pedro Blasques et al. "Hydro-elastic analysis and optimization of a composite marine propeller". In: *Marine Structures* 23.1 (2010), pp. 22–38.
- [14] MR Motley et al. "Utilizing fluid–structure interactions to improve energy efficiency of composite marine propellers in spatially varying wake". In: *Composite structures* 90.3 (2009), pp. 304–313.
- [15] R Vijayanandh et al. "Comparative fatigue life estimations of Marine Propeller by using FSI". In: *Journal of Physics: Conference Series*. Vol. 1473. 1. IOP Publishing. 2020, p. 012018.
- [16] Joris Degrieck and et al. "Fatigue damage modeling of fibre-reinforced composite materials". In: *Appl. Mech. Rev.* 54.4 (2001), pp. 279–300.
- [17] M Kawai. "Fatigue life prediction of composite materials under constant amplitude loading". In: *Fatigue life prediction of composites and composite structures*. Elsevier, 2020, pp. 425–463.
- [18] Wim Van Paepegem. "Fatigue damage modelling of composite materials with the phenomenological residual stiffness approach". In: *Fatigue life prediction of composites and composite structures*. Elsevier, 2010, pp. 102–138.
- [19] W Hwang et al. "Fatigue of composites—fatigue modulus concept and life prediction". In: *Journal of Composite Materials* 20.2 (1986), pp. 154–165.
- [20] SS Wang et al. "Fatigue damage and degradation in random short-fiber SMC composite". In: *Journal of Composite Materials* 17.2 (1983), pp. 114–134.

- [21] H Mao et al. "Fatigue damage modelling of composite materials". In: *Composite Structures* 58.4 (2002), pp. 405–410.
- [22] Christos Kassapoglou. "Fatigue model for composites based on the cycle-by-cycle probability of failure: implications and applications". In: *Journal of composite materials* 45.3 (2011), pp. 261–277.
- [23] MM Shokrieh et al. "Fatigue life prediction of composite materials based on progressive damage modeling". In: *Fatigue life prediction of composites and composite structures*. Elsevier, 2010, pp. 249–292.
- [24] Roohollah Sarfaraz et al. "A hybrid S–N formulation for fatigue life modeling of composite materials and structures". In: *Composites Part A: Applied Science and Manufacturing* 43.3 (2012), pp. 445–453.
- [25] AP Vassilopoulos. "Introduction to the fatigue life prediction of composite materials and structures: past, present and future prospects". In: *Fatigue life prediction of composites and composite structures*. Elsevier, 2010, pp. 1–44.
- [26] NP Inglis. "Hysteresis and fatigue of Wohler rotating cantilever specimen". In: *The Metallurgist* 1.1 (1927), pp. 23–27.
- [27] Olivier Cousigné et al. "Development of a new nonlinear numerical material model for woven composite materials accounting for permanent deformation and damage". In: *Composite Structures* 106 (2013), pp. 601–614.
- [28] PM Jelf et al. "The failure of composite tubes due to combined compression and torsion". In: *Journal of materials science* 29 (1994), pp. 3080–3084.
- [29] Andrew Makeev et al. "A method for measurement of multiple constitutive properties for composite materials". In: *Composites Part A: Applied Science and Manufacturing* 43.12 (2012), pp. 2199–2210.
- [30] Joeun Choi et al. "A Methodology to Predict the Fatigue Life under Multi-Axial Loading of Carbon Fiber-Reinforced Polymer Composites Considering Anisotropic Mechanical Behavior". In: *Materials* 16.5 (2023), p. 1952.
- [31] RM Di Benedetto et al. "Energy absorption study considering crush test on carbon fiber/epoxy and carbon fiber/polyurethane structural composite beams". In: *Composite Structures* 203 (2018), pp. 242–253.
- [32] Zhenyu Qiu et al. "Nonlinear modeling of bamboo fiber reinforced composite materials". In: *Composite Structures* 238 (2020), p. 111976.
- [33] Štefan Obid et al. "Non-linear elastic tension–compression asymmetric anisotropic model for fibre-reinforced composite materials". In: *International Journal of Engineering Science* 185 (2023), p. 103829.
- [34] John W Holmes et al. "Experimental observations of frictional heating in fiber-reinforced ceramics". In: *Journal of the American Ceramic Society* 75.4 (1992), pp. 929–938.
- [35] Li Longbiao. "A hysteresis dissipated energy-based parameter for damage monitoring of carbon fiber-reinforced ceramic–matrix composites under fatigue loading". In: *Materials Science and Engineering: A* 634 (2015), pp. 188–201.
- [36] A Vahid Movahedi-Rad et al. "A novel fatigue life prediction methodology based on energy dissipation in viscoelastic materials". In: *International Journal of Fatigue* 152 (2021), p. 106457.
- [37] M Ospina Cadavid et al. "Experimental studies of stiffness degradation and dissipated energy in glass fibre reinforced polymer composite under fatigue loading". In: *Polymers and Polymer Composites* 25.6 (2017), pp. 435–446.
- [38] Sascha Stikkelorum. "Investigating energy dissipation for a methodology to fatigue master curves". In: (2019).
- [39] SB Sapozhnikov et al. "Predicting the kinetics of hysteretic self-heating of GFRPs under high-frequency cyclic loading". In: *Composite Structures* 226 (2019), p. 111214.
- [40] Matthias Drvoderic et al. "Comparing crack density and dissipated energy as measures for off-axis damage in composite laminates". In: *International Journal of Fatigue* 169 (2023), p. 107486.

- [41] Javier Romaris Villanueva. "An Analytical Method for Predicting Delamination Onset and Growth induced by Matrix Cracks under Quasi-Static loading". In: (2023).
- [42] Walid Roundi et al. "Experimental investigation of the fatigue behavior of glass/epoxy composites evaluated by the stiffness degradation and damage accumulation". In: *Journal of Composite Materials* 53.6 (2019), pp. 731–740.
- [43] Md Rafiquzzaman et al. "Behavioural observation of laminated polymer composite under uniaxial quasi-static and cyclic loads". In: *Fibers and Polymers* 16 (2015), pp. 640–649.
- [44] T Kevin O'Brien et al. "Tension fatigue analysis and life prediction for composite laminates". In: *International journal of fatigue* 11.6 (1989), pp. 379–393.
- [45] A Makeev et al. "Fatigue structural substantiation for thick composites". In: *Proceedings of the 17th international conference on composite materials*. 2009.
- [46] Thanh Chi Truong et al. "Carbon composites based on multi-axial multi-ply stitched preforms. Part 4. Mechanical properties of composites and damage observation". In: *Composites Part A: applied science and manufacturing* 36.9 (2005), pp. 1207–1221.
- [47] Katleen Vallons et al. "Carbon composites based on multi-axial multi-ply stitched preforms—Part 6. Fatigue behaviour at low loads: Stiffness degradation and damage development". In: *Composites Part A: Applied Science and Manufacturing* 38.7 (2007), pp. 1633–1645.
- [48] Wouter de Bles. "Dynamic response reconstruction of an FRC blade with embedded piezoelectric sensors". In: (2022).
- [49] MSC Marc. "MENTAT: Volume B: Element Library, MSC". In: *Software Corporation* (2012).
- [50] MSC Marc. "Theory and user information, vol". In: *AD, MSC Software Corporation* (2010).
- [51] Mahmood M Shokrieh et al. "Tension behavior of unidirectional glass/epoxy composites under different strain rates". In: *Composite structures* 88.4 (2009), pp. 595–601.
- [52] Shaohua Zhang et al. "Influence of fibre orientation on pultruded GFRP material properties". In: *Composite Structures* 204 (2018), pp. 368–377.
- [53] SH Lee et al. "Compressive response and failure of fiber reinforced unidirectional composites". In: *International Journal of Fracture* 100 (1999), pp. 275–306.
- [54] AS Kaddour et al. "Mechanical properties and details of composite laminates for the test cases used in the third world-wide failure exercise". In: *Journal of Composite Materials* 47.20-21 (2013), pp. 2427–2442.
- [55] Wim Van Paepegem et al. "Modelling the nonlinear shear stress–strain response of glass fibre-reinforced composites. Part I: Experimental results". In: *Composites science and technology* 66.10 (2006), pp. 1455–1464.
- [56] Wim Van Paepegem et al. "Modelling the nonlinear shear stress–strain response of glass fibre-reinforced composites. Part II: Model development and finite element simulations". In: *Composites Science and Technology* 66.10 (2006), pp. 1465–1478.
- [57] TP Philippidis et al. "Fatigue strength prediction under multiaxial stress". In: *Journal of Composite Materials* 33.17 (1999), pp. 1578–1599.



## Matlab functions

The two functions mentioned in Chapter 3 (Methodology) are detailed here, explaining how they work. First, we will look at the *grabit* function, followed by a demonstration of script that made by using *fmincon* function.

The *grabit* function is used to extract data from an image. According to MathWorks, the user can import files in BMP, JPG, TIF, and PNG formats, and then extract data from the image. To illustrate how this function operates, an example will be provided below for the coupon  $[0_3/90]_s$  from the work of Roundi et al. [42]. The original data on stress-strain curves from static experiments are shown in Figure 3.5.

When the function has ran, a GUI screen opens, allowing the user to import the image.

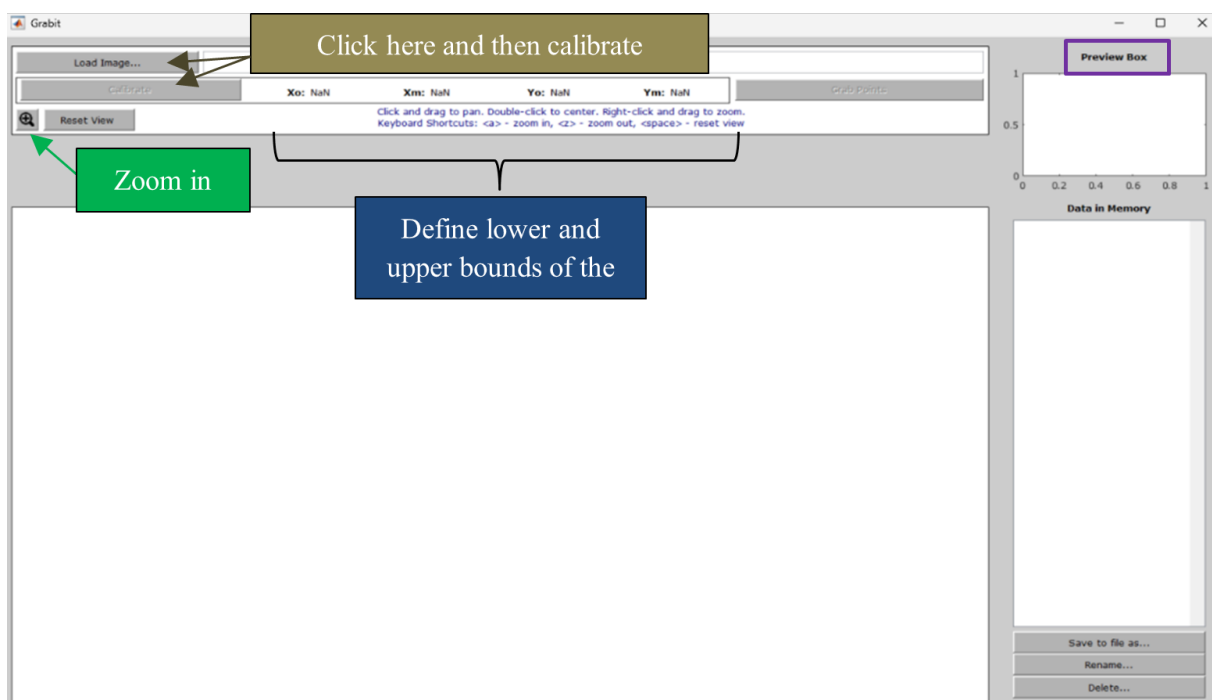


Figure A.1: GUI of grabit function

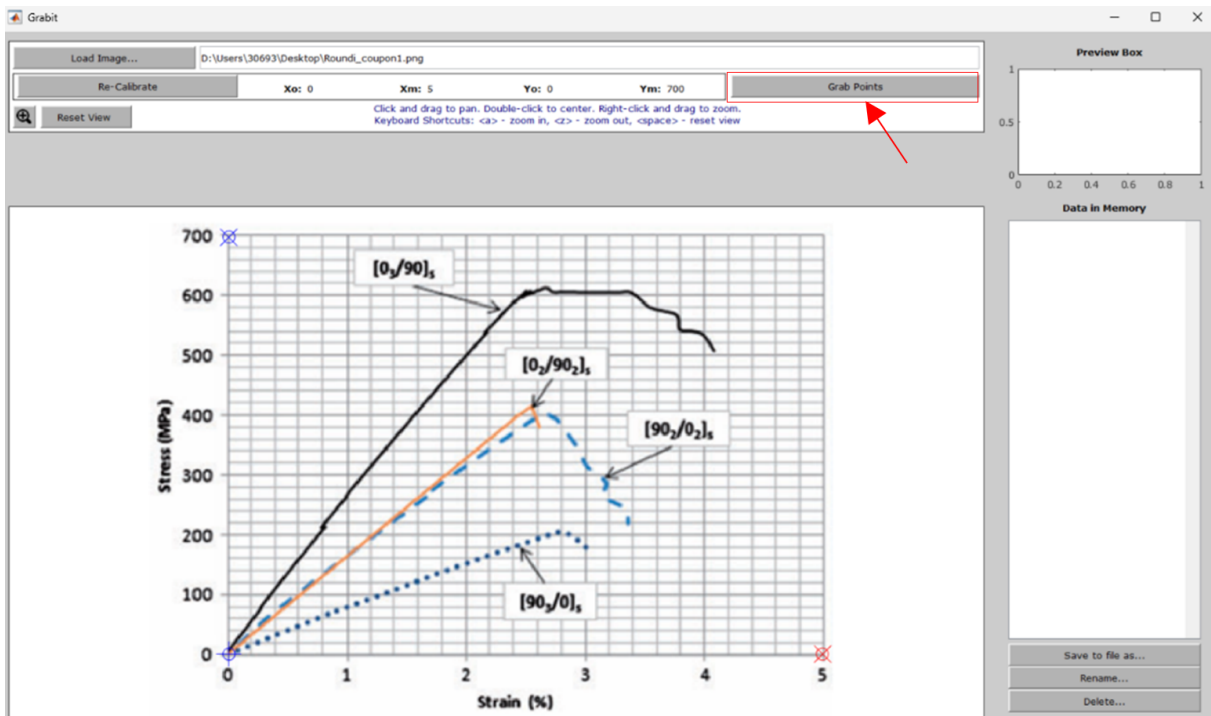


Figure A.2: Calibration of the curve

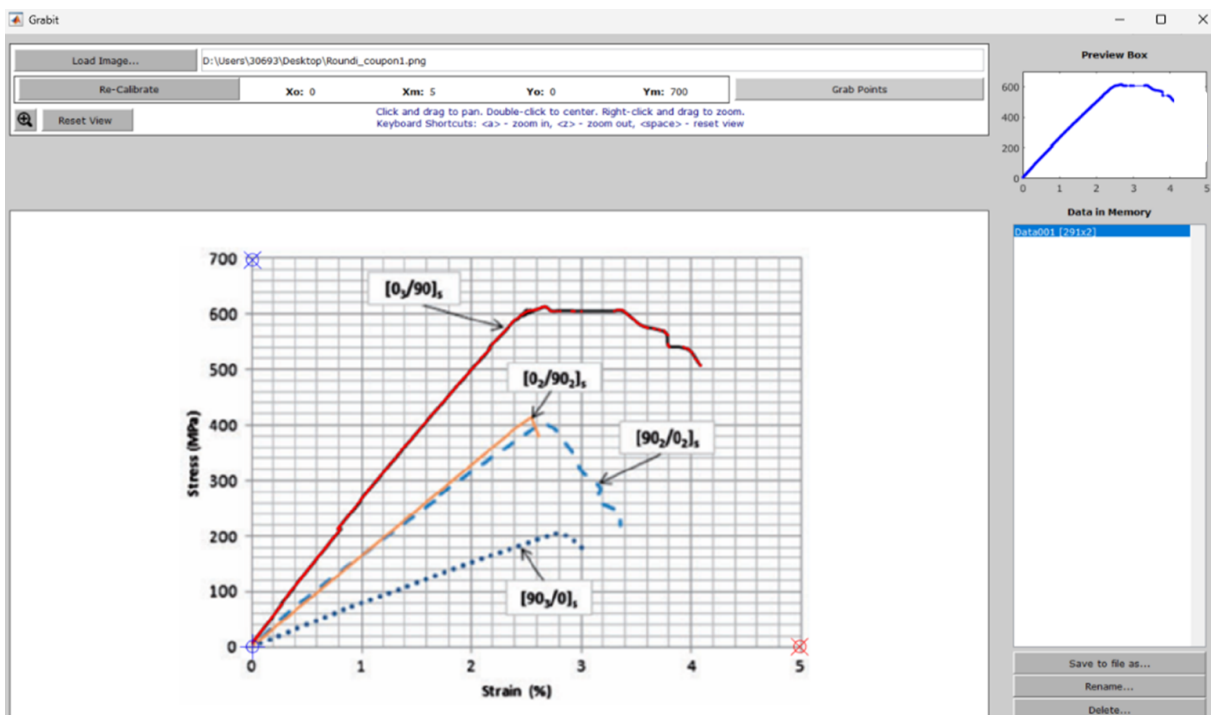
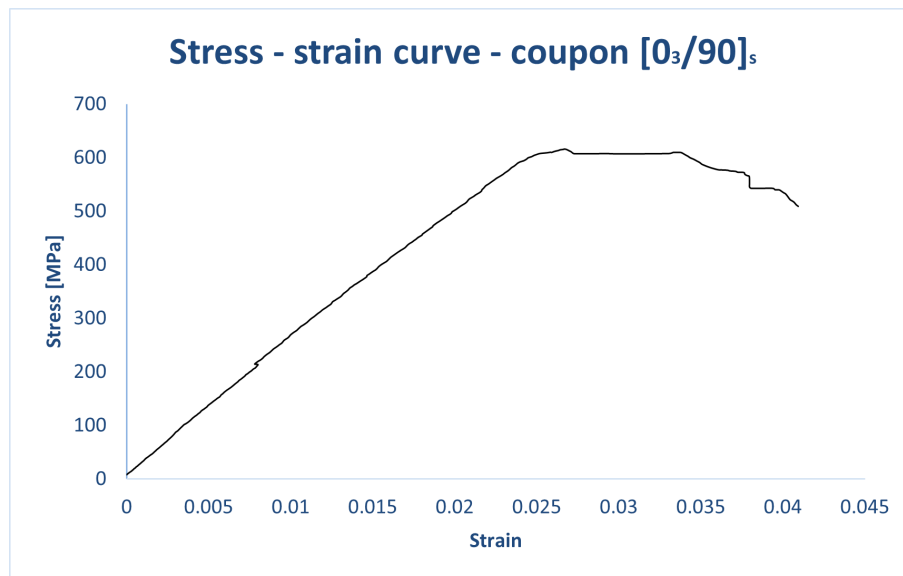


Figure A.3: Grabbing points

where the extracted data lead to the following stress strain curve (after dividing the digitized data for strains by 100):



**Figure A.4:** Resultant curve - coupon [0<sub>3</sub>/90]<sub>s</sub>

Regarding *fmincon*, this function is used to find the minimum of a constrained nonlinear multivariable function. The following script shows how it was used to determine exponent  $n$  according to the theory presented in Chapter 3 (3.1.2).

```
function [n] = optimization_techn(stress, strain, Eo, U, Sf)
    % Define the model function with specific values
    f = @(x) (stress./Eo) + (x(1)+1)/(x(1))*U*(stress./Sf).^x(1);

    % Define the objective function
    opt_function = @(x) sum(((f(x) - strain)./ strain).^2);

    % Initial guess for optimization
    initialGuess = stress(1); % Starting point within the desired range

    % Define lower and upper bounds for the parameters
    lb = 1; % Lower bounds for params(1) and params(2)
    ub = +20; % Upper bounds for params(1) and params(2) and params(3)

    % Perform constrained optimization using fmincon
    options = optimset('fmincon');
    options.Display = 'iter'; % Display iteration information
    optimizedParams = fmincon(opt_function, initialGuess, [], [], [], [], lb, ub, [], options);

    n = optimizedParams(1);
    disp('Optimized Parameters:');
    disp(optimizedParams);
end
```

**Figure A.5:** Script with *fmincon*

First, the Ramberg-Osgood function was defined as  $f(x)$ , where  $x(1)$  corresponds to the exponent  $n$ . Then, the objective function described in the theory (check equation 3.22) was defined, and the starting point along with the lower and upper limits for exponent  $n$  were applied. Essentially, the value of  $x(1)$  is determined so that the function  $f(x)$  results in a strain value close to the experimental one, using the stress measured in the experiment at that specific point as an input. This means that the “fmincon” function returns the value of  $n$  that minimizes the numerator of the objective function.

# B

## Material properties of GFRP blade

The following image constitutes the original plan for the fabrication of the blade. This image was taken from the work of de Bles [48].

LAMINAATOPBOUW Sensorprop Versie 16-06-2021 - V6									
Laag	Offset	Zone 1 / Zone 6	Zone 2 / Zone 7	Zone 3 / Zone 8	Zone 4 / Zone 9	Zone 5 / Zone 10	Root 1 / Root 2	Type	Dikte
1		Ondermaal							
2				0				ERW 200	0,17
3						0		UD 600	0,5
4							0	UD 600	0,5
5							0	G-Flow	0,5
6							0	UD 600	0,5
7	0mm			-20				UD 600	0,5
8							0	UD 600	0,5
9	-15mm			-20				UD 600	0,5
10	-20mm			0				G-Flow	0,5
11							0	UD 600	0,5
12						-20		UD 600	0,5
13	-10mm			15				UD 600	0,5
14						15		UD 600	0,5
15						0		G-Flow	0,5
16	0mm			60				UD 600	0,5
17							60	UD 600	0,5
18	-5mm			105				UD 600	0,5
19					60			UD 600	0,5
20							60	UD 600	0,5
21				0				G-Flow	0,5
22				15				UD 600	0,5
23						15		UD 600	0,5
24						-20		UD 600	0,5
25						0		G-Flow	0,5
26						-20		UD 600	0,5
27							-20	UD 600	0,5
28							0	UD 600	0,5
29	-30mm							Polymat	1-3
30							0	UD 600	0,5
31						-20		UD 600	0,5
32						-20		UD 600	0,5
33						0		G-Flow	0,5
34						-20		UD 600	0,5
35							15	UD 600	0,5
36				15				UD 600	0,5
37				0				G-Flow	0,5
38							60	UD 600	0,5
39						60		UD 600	0,5
40						105		UD 600	0,5
41							-60	UD 600	0,5
42	0mm			60				UD 600	0,5
43						0		G-Flow	0,5
44						15		UD 600	0,5
45	-10mm			15				UD 600	0,5
46							-20	UD 600	0,5
47							0	UD 600	0,5
48	-15mm			-20				UD 600	0,5
49							0	UD 600	0,5
50	-20mm			0				G-Flow	0,5
51	0mm			-20				UD 600	0,5
52							0	UD 600	0,5
53							0	G-Flow	0,5
54							0	UD 600	0,5
55							0	UD 600	0,5
56				0				ERW 200	0,17

Figure B.1: Original stacking sequence of the GFRP blade

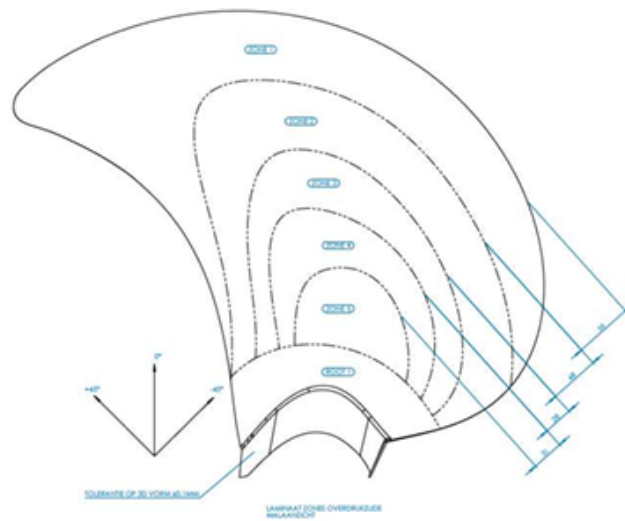
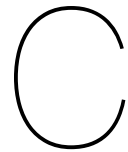


**Figure B.2:** Allocation of the different zones

However, some discrepancies made during the fabrication and that was the reason that a new FEA model was created. The correct the layup of the final blade can be found in the next table.



No. of ply	Offset	Zone 1 / Zone 6	Zone 2 / Zone 7	Zone 3 / Zone 8	Zone 4 / Zone 9	Zone 5 / Zone 10	Root 1 / Root 2	Type of fabric	Thickness
1				0				ERW 200	0.17
2						0		UD 600	0.5
3							0	UD 600	0.5
4							0	UD 600	0.5
5							0	UD 600	0.5
6	0mm			-20				UD 600	0.5
7							0	UD 600	0.5
8	-15mm			-15				UD 600	0.5
9	-20mm			0				G-Flow	0.5
10							0	UD 600	0.5
11						-20		UD 600	0.5
12	-10mm			25				UD 600	0.5
13						15		UD 600	0.5
14						0		G-Flow	0.5
15	0mm			60				UD 600	0.5
16							-60	UD 600	0.5
17	-5mm			105				UD 600	0.5
18					-60			UD 600	0.5
19							-60	UD 600	0.5
20				0				G-Flow	0.5
21				15				UD 600	0.5
22						15		UD 600	0.5
23					65			UD 600	0.5
24					0			G-Flow	0.5
25					65			UD 600	0.5
26						-20		UD 600	0.5
27							0	UD 600	0.5
28	-30mm			matrix				Polymat	
29							0	UD 600	0.5
30						-20		UD 600	0.5
31					15			UD 600	0.5
32					0			G-Flow	0.5
33					15			UD 600	0.5
34						15		UD 600	0.5
35				10				UD 600	0.5
36				0				G-Flow	0.5
37						60		UD 600	0.5
38					50			UD 600	0.5
39					105			UD 600	0.5
40							60	UD 600	0.5
41	0mm			60				UD 600	0.5
42						0		G-Flow	0.5
43						15		UD 600	0.5
44	-10mm			15				UD 600	0.5
45						-20		UD 600	0.5
46							0	UD 600	0.5
47	-15mm			0				G-Flow	0.5
48							-25	UD 600	0.5
49	-20mm			25				UD 600	0.5
50	0mm			-20				UD 600	0.5
51							0	G-Flow	0.5
53							0	UD 600	0.5
53				0				ERW 200	0.17



# FEA: Marc Mentat

This chapter is dedicated to Marc Mentat, providing essential information to help a new FEM engineer run an analysis. After installing Marc, it is crucial to install a Fortran compiler to compile any required subroutine. Note that Fortran allows no more than 73 characters per line. All the guidelines that are presented in this chapter are based on personal experience and of course, there are better ways to handle the program with those skills being obtained after some experience.

Upon initiating Marc, the user can import or open a file by selecting "File" and then "Import" or "Open," respectively. If the imported object or structure is not visible, selecting "Reset View" and "Fill View" can help display it.

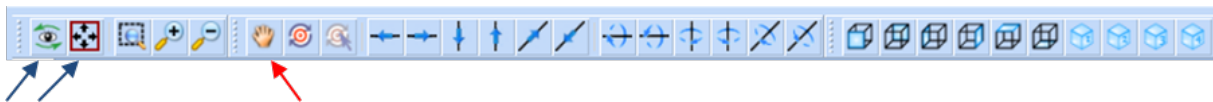


Figure C.1: Marc Mentat - GUI

To rotate or move the imported object, the user should enable the dynamic control mouse, represented by the red arrow symbol. This option should be deselected when performing other tasks. Exploring the various options will allow the user to discover more details about them. A simplified model of a coupon will be presented here using a 3D analysis.

## Geometry & Mesh

First, the user should define the units and dimensions of the coupon. Select the "Length Unit" option in the "Geometry & Mesh" tab, and choose from the emerging list of units. Assuming mm is selected, choose "Geometry & Mesh" in the same tab to define points, curves, surfaces, and solids. For this example, a solid will be designed. By pressing "Add", the sentence "Enter block solid origin coordinates" appears in the dialog box; input 0,0,0 as the origin of the coordinate system. Then, define the dimensions of the object, ensuring consistency with the initially selected units (e.g., mm).

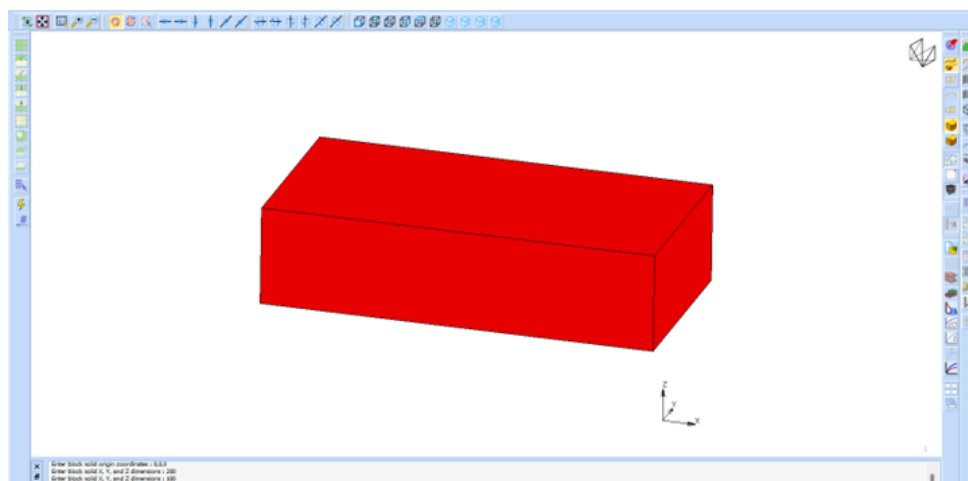


Figure C.2: Create a solid

Due to the simple geometry of this parallelepiped, select the "Volumes" option in the Automesh tab. Choose hexahedral volumes in the target family (Volume) and define the target element size. Ensure that the largest element size used is the minimum dimension. Finally, select "Voxel Mesh" and then the object, creating the mesh.

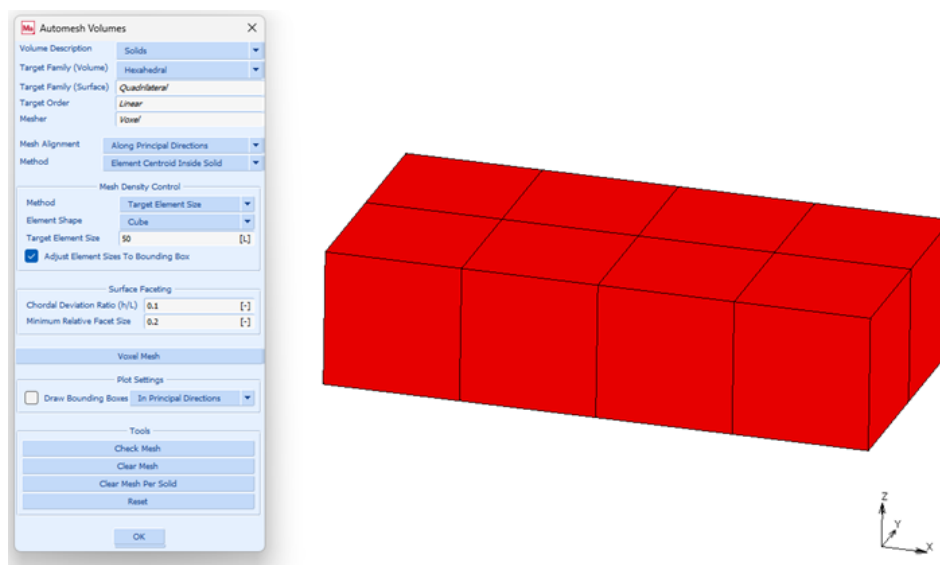


Figure C.3: Meshing

Marc offers various elements, detailed in its documentation. In this case, the coupon represents a composite laminate. To provide more details, the solid will be split into three regions, with three elements through the thickness to match the thesis's element types.

To change the class of the elements (e.g., using hexahedral elements), select "Change Class," choose Hex (20), and apply it to all existing elements in the "Elements" tab.

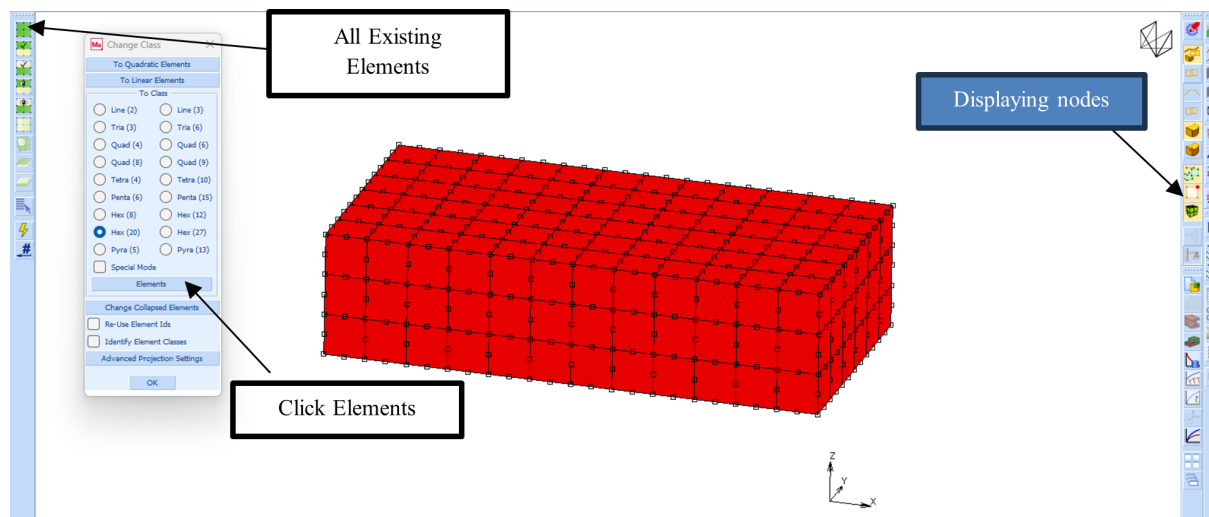


Figure C.4: Selecting hexahedral elements

The 3D composite element in Marc is Element type 150, as presented in the thesis. To select this element, go to the "Jobs" tab and then to "Element Types." Select "Solid Composite/Gasket" for all existing elements. Verify correct application by clicking "ID Types" and "ID Classes" in the "Element Types" tab.

### Geometric Properties

Under "Geometric Properties," select "Solid Composite/Gasket," and "Face 4" as the direction, assuming the z-direction is through the thickness. Click "Add" and apply this property to all existing elements.

## Material Properties

Defining material properties is critical for the analysis. In the "Material Properties" tab, click "New" and select "Standard" to create a lamina or matrix core.

Assuming the matrix core is created first, since the material is isotropic, select "Elastic-Plastic Isotropic," and input Young's modulus and Poisson ratio. If a failure criterion is to be used, select the "Damage Effects" tab and choose failure instead of damage.

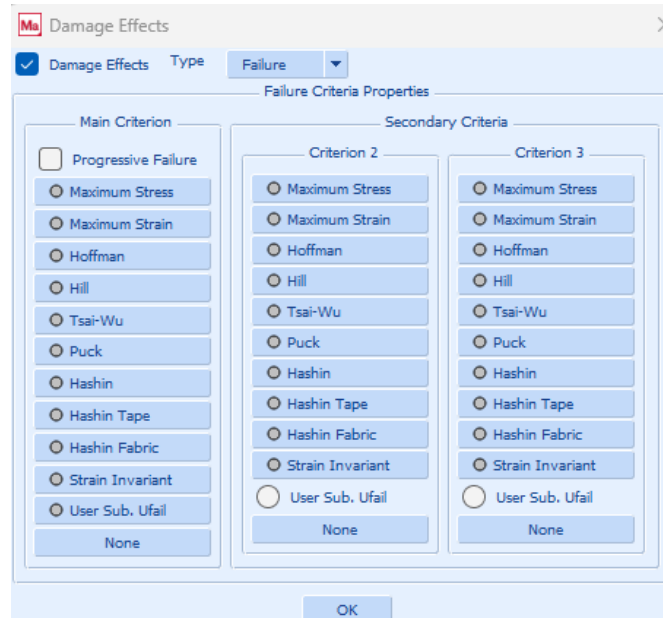


**Figure C.5:** Available failure criteria

If a user subroutine is to be used for a failure criterion, select "User Sub. Ufail." Otherwise, up to three criteria from the list can be used, detailed in Marc's documentation. Before applying this material to the elements, define the different laminas. Select "Standard" again, choose "Elastic-Plastic Orthotropic," and apply the properties in three directions. Similarly, select "Damage Effects" and apply the failure criteria. To construct the laminate, select "Composite" instead of "Standard" material.

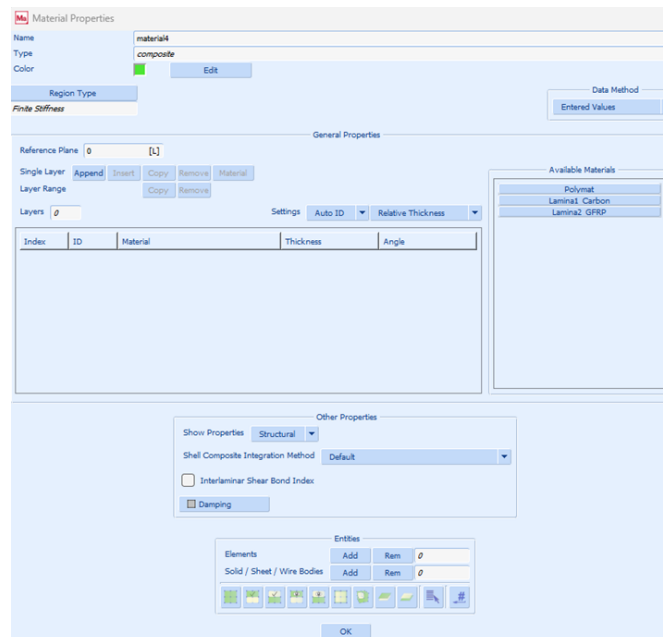


**Figure C.6:** Creating a composite material

The available materials will be displayed on the right. To build the laminate, click "Append" and create the stacking sequence. Assume the coupon consists of a carbon fiber oriented at 60 degrees, a GFRP blade oriented at 45 degrees, a core matrix, and symmetrical laminas. Assign the appropriate material to each element.

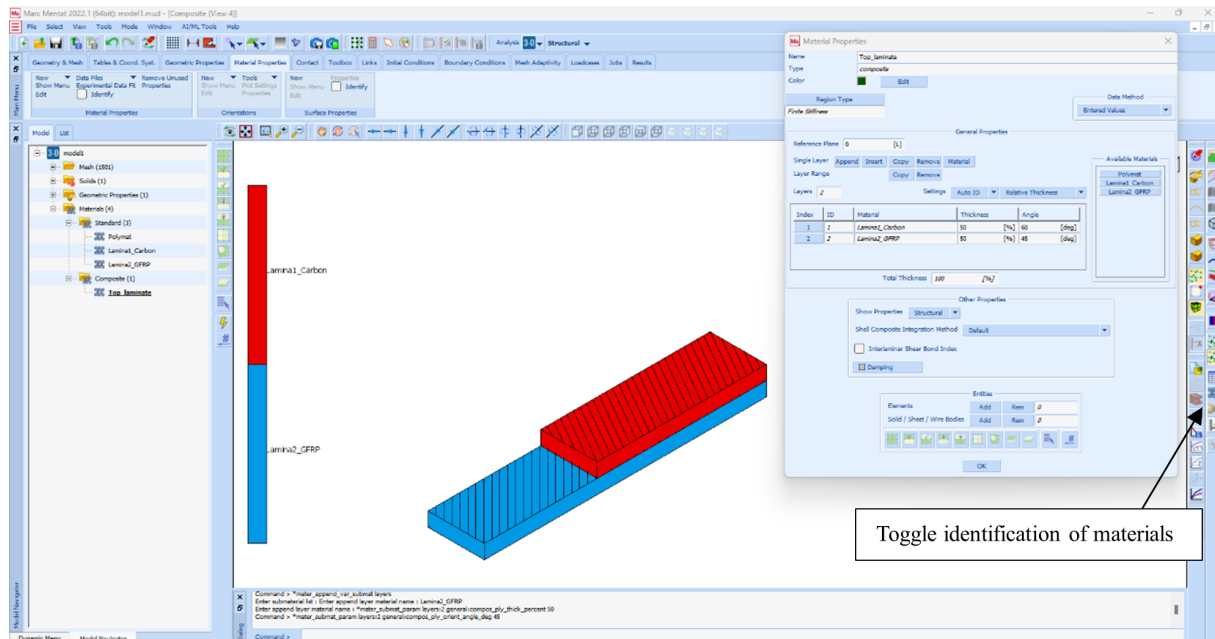


Figure C.7: Stacking sequence

Creating the external surfaces of the coupons first and hiding them to apply the polymat material to the middle elements by selecting "Add" for all visible elements yields the desired laminate structure.

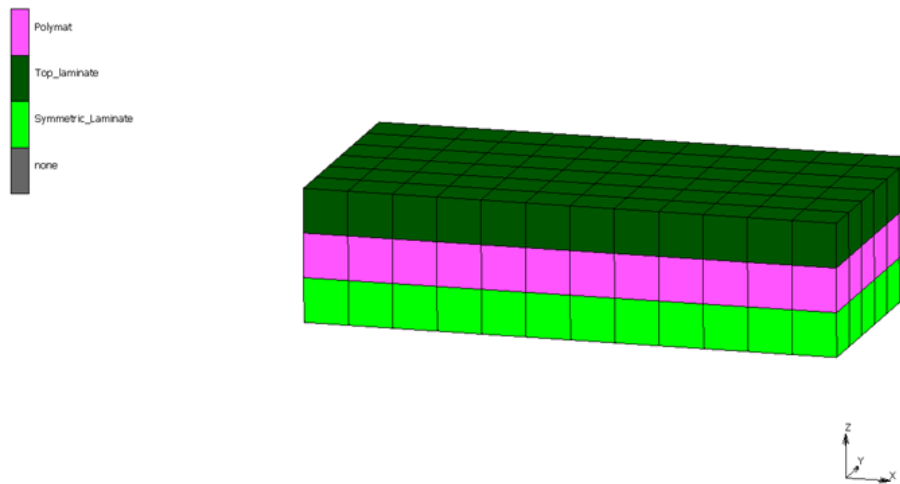
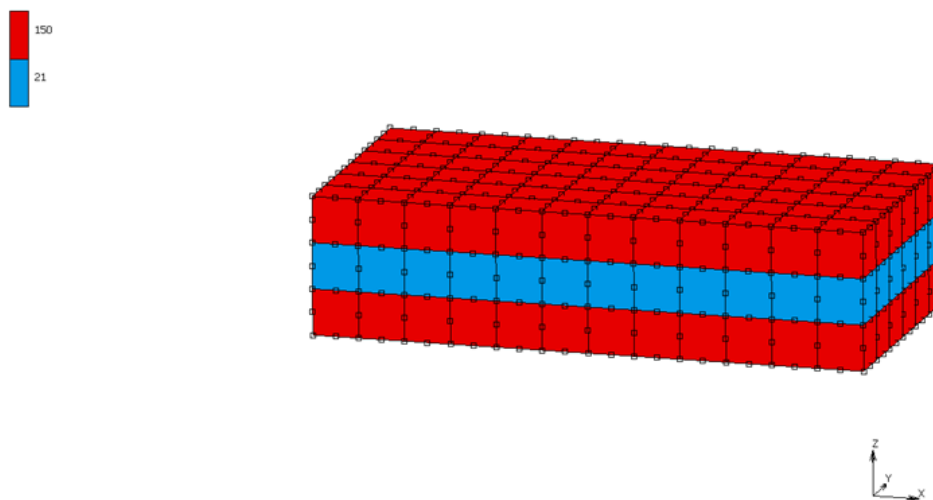


Figure C.8: Different materials

To apply a second type of element, such as solid brick elements type 21, return to the "Geometric Properties" tab, select "Solid," and then hide the composite materials to choose the middle elements. This process applies the correct section to the middle elements. From the "Jobs" tab, select solid element 21 and apply it to the middle elements.



**Figure C.9:** Different types of elements

In the "Material Properties," apply "Usub Orient2" to ensure the Z-direction is through the thickness if draping capabilities are needed. However, for this coupon, the "Usub Orient2" subroutine is unnecessary as it was specific to correcting fiber orientation in the complex shape of the blade described in the thesis.

### Boundary Conditions

Assuming the coupon is clamped on one side and under tension on the other, click "New" in the "Boundary Conditions" tab to restrict displacement in all axes and apply the condition to the desired nodes.

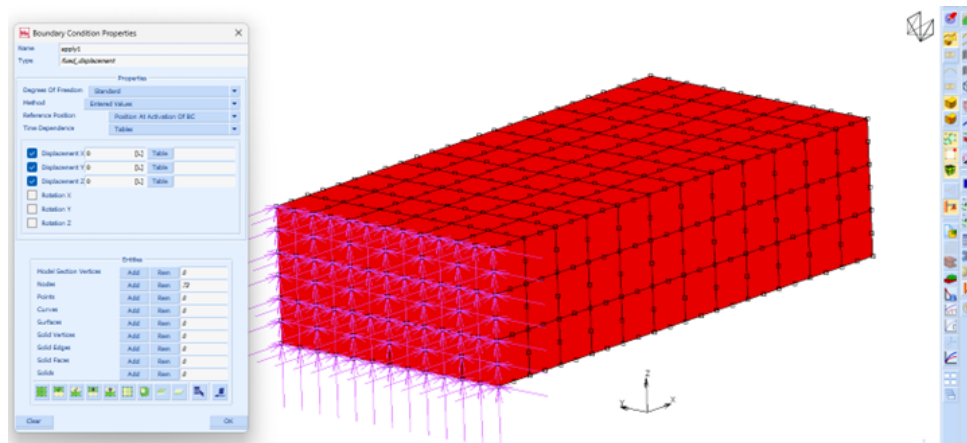


**Figure C.10:** Clamped boundary condition

Similarly, apply a point load to each node on the other side of the coupon.

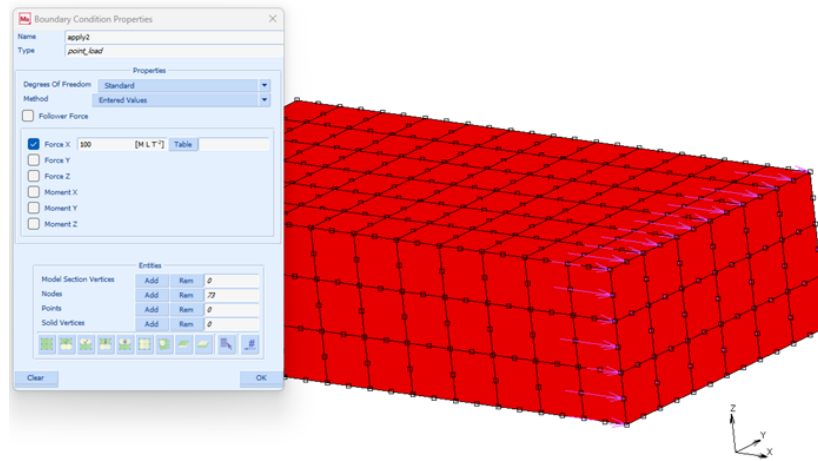


Figure C.11: Tensile force at the other side

For a smooth load application, use "Tables Coord. Syst." and follow the provided guidelines.

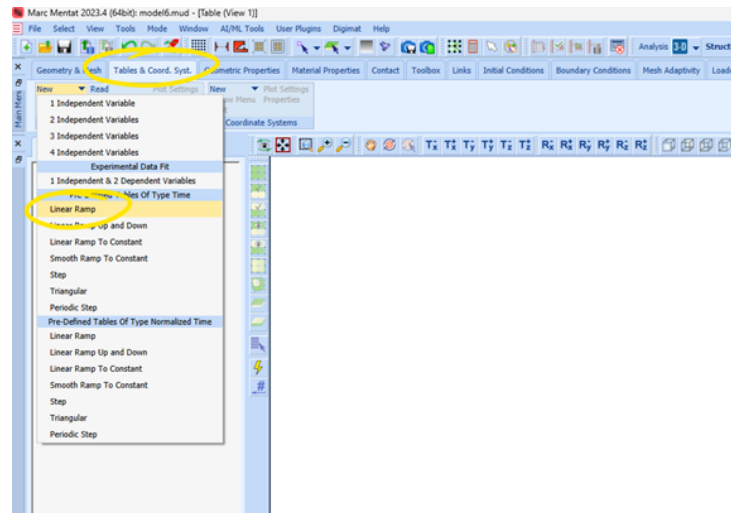


Figure C.12: Use table

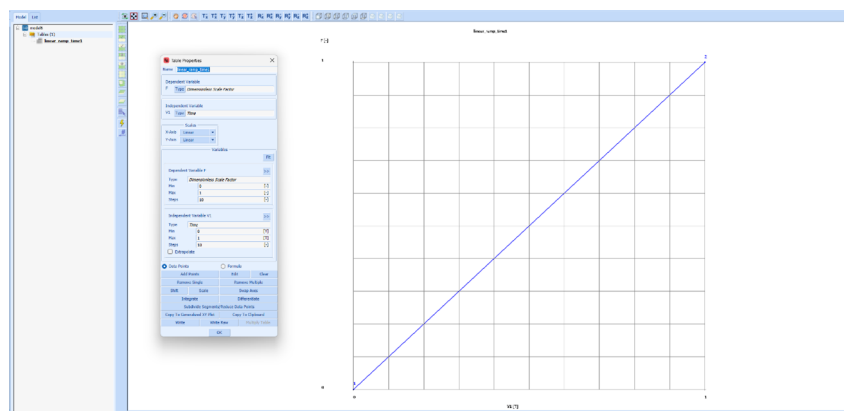


Figure C.13: Apply the load linearly

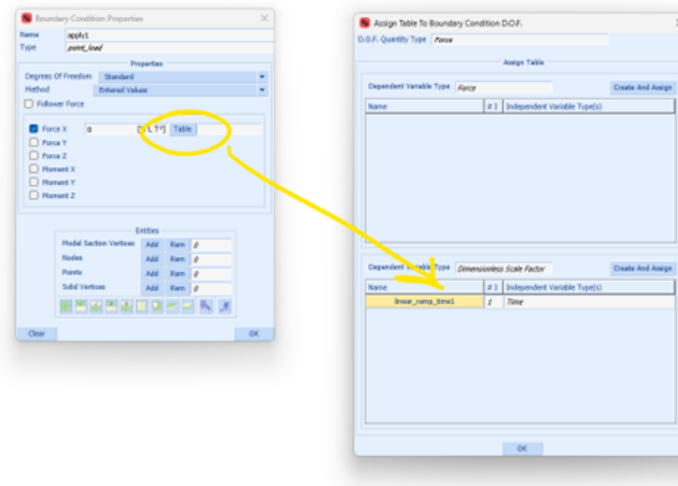


Figure C.14: Select table when the load is applied

### Loadcases

Select a new load case in the corresponding tab, choose "Static," and define the time steps for the analysis. For this analysis, only one step is adequate, but this depends on user requirements.

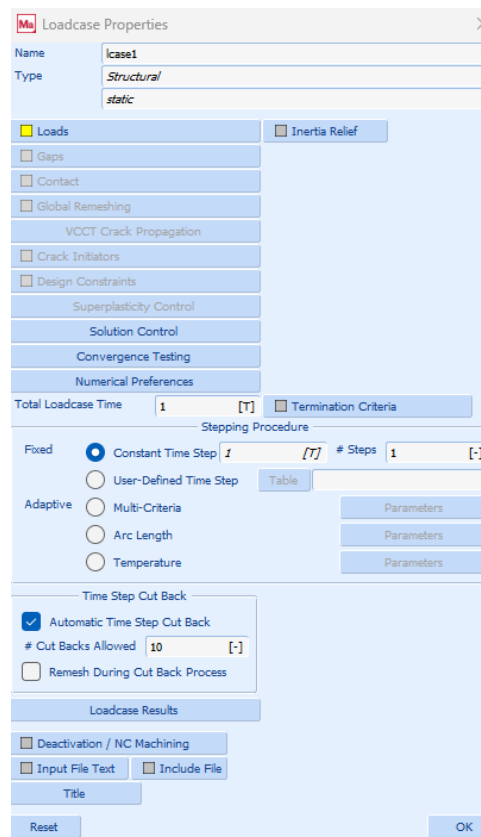
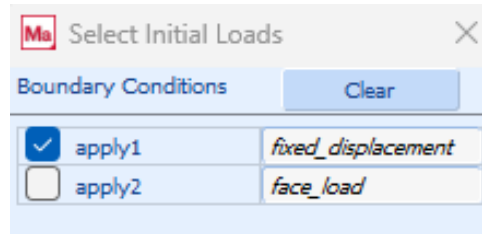


Figure C.15: Time steps



## Jobs

In the "Jobs" tab, select the type of analysis (e.g., Structural) and choose between three numerical methods for result calculation. "Large Strain" was selected in the thesis, but further information is available in Marc's documentation. For initial loads, only displacement should be selected as the coupon is assumed intact before loading.



**Figure C.16:** Initial loading

Select load case "Icase1" and choose the list of job results.

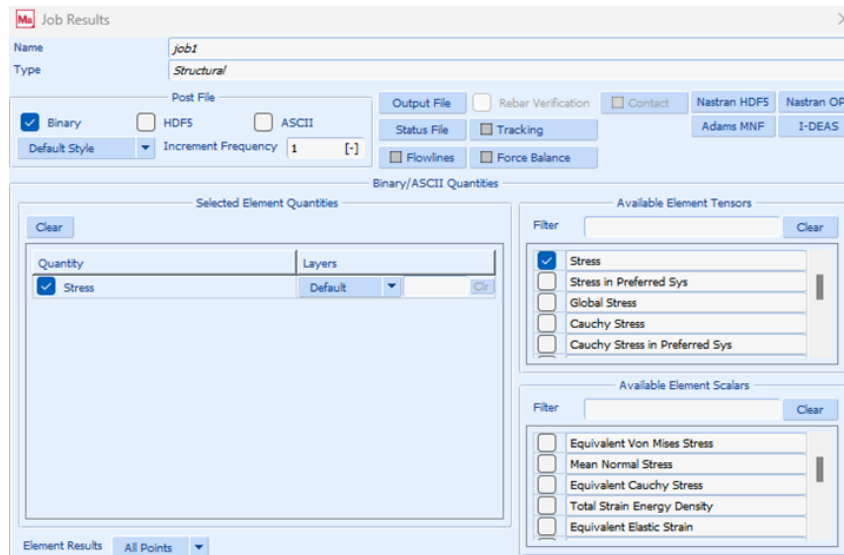


**Figure C.17:** Job results

In "Job Properties," under the "Analysis Options" tab, details about the solving process are available. Before running an analysis, perform a "Check" to identify any warnings or errors in the model. If no problems are found, press "Submit" to run the model. If a user subroutine is required, import it by clicking "Fortran Source File" and selecting the subroutine, ensuring it is on the same disk as the Fortran compiler.

## Results

To view the results, ensure the "Status" indicates "Complete," then click "Open Binary Post File." Results can be viewed in the "Model Plot" tab. To extract data from the model, follow the provided process.

## Results Reporting

### Output nodal and element values to an external file

- ❑ NEW/APPEND: Toggles whether to create new report or append
- ❑ MODEL SUMMARY provides a summary of the post file data. It includes the available post values and will report the global values for each selected increment. If a Mentat model is open, a summary of the model is listed (materials, contact bodies, etc)
- ❑ NODE DATA will list the nodal data (XYZ coordinates)
- ❑ ELEMENT DATA will list the element data consisting of number of nodes, edges, faces. If a Mentat model is open, additional data of the material, geometric property, orientation property and contact body will be listed
- ❑ ELEMENT CONN will list the node connectivity of the element
- ❑ OUTPUT OPTIONS provides access to the layout of the floating point data
- ❑ SCOPE: Selects the node/elements required
- ❑ DESCENDING/ASCENDING: Output data in either descending value or ascending value order
- ❑ VALUE/IDENTIFIER: Sort items based on either the value or the identifier (node or element id)
- ❑ DATA COLLECTION: By default the current increment data is collected. A list of increments may be selected by turning on the INCREMENT LIST toggle and selecting the increments using the LIST menu
- ❑ NODAL VALUES enables output of the nodal data values
- ❑ ELEMENT VALUES enables output of the element data values
- ❑ CREATE REPORT runs the report. Output is written to the specified file
- ❑ OPEN REPORT opens the report file

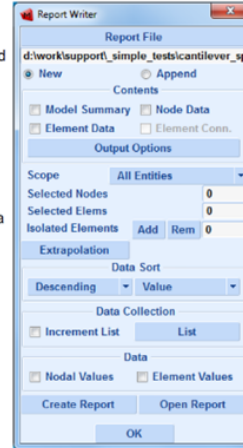


Figure C.18: Extract results

## Tools: Max/Min & Range Selection

- ❑ Select element / nodes with maximum or minimum values easily
- ❑ Select elements / nodes with values within a specified range

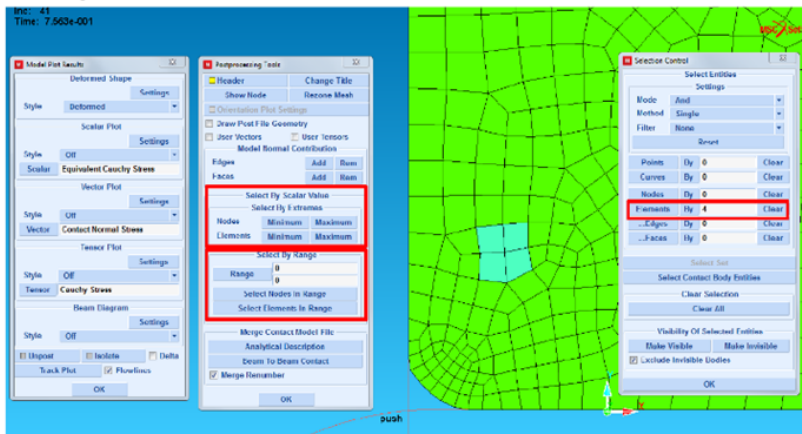
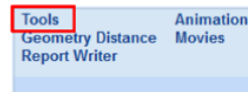


Figure C.19: Tools